Notes for the International Summer School on Advanced Ultrasound Imaging

Jørgen Arendt Jensen

May 26, 2015

Center for fast Ultrasound Imaging, Dept. of Elec. Eng., Technical University of Denmark

This page is inserted to facilitate double sided printing.

CONTENTS

CHAPTER

ONE

Introduction

These notes have been prepared for the international summer school on advanced ultrasound imaging in June 2015 at the Technical University of Denmark. The notes should be read in conjunction with the notes prepared by Trahey[1]. The intended audience is Ph.D. students working in medical ultrasound. A knowledge of general linear acoustics and signal processing is assumed.

The notes give a linear description of general ultrasound imaging through the use of spatial impulse responses. It is shown in Chapter 2 how both the emitted and scattered fields for the pulsed and continuous wave case can be calculated using this approach. Chapter 3 gives a brief overview of modern ultrasound imaging and how it is simulated using spatial impulse responses. The first two chapters are based on the previous summer school course notes in [2]. Chapter 4 gives a brief description of both spectral and color flow imaging systems and their modeling and simulation along with the more modern vector velocity systems. This is based on the book chapter in [3]. A description of synthetic aperture imaging is given in Chapter 5 based on [4]. The final chapter is on sequential beamforming for synthetic aperture imaging and is based on [5].

For the summer school it is assumed that the participant has read and understands the first two chapters on linear imaging. Lectures will be given on the content of the other chapters.

Jørgen Arendt Jensen
May, 2015.

Center for fast Ultrasound Imaging
DTU Elektro, Build. 349,
Technical University of Denmark
DK-2800 Lyngby, Denmark
E-mail: jaj@elektro.dtu.dk
Web: http://bme.elektro.dtu.dk/jaj/

[1] [1] Martin E. Anderson, Nick Bottenus and Gregg E. Trahey: A seminar on k-space applied to medical ultrasound, Dept. of Biomedical Engineering, Duke University, 2015

CHAPTER

TWO

Description of ultrasound fields

This chapter gives a linear description of acoustic fields using spatial impulse responses. It is shown how both the pulsed emitted and scattered fields can be accurately derived using spatial impulse responses, and how attenuation and different boundary conditions can be incorporated. The chapter goes into some detail of deriving the different results and explaining their consequence. Different examples for both simulated and measured fields are given. The chapter is based on the papers [6], [7] and [8] and on the book [9].

2.1 Fields in linear acoustic systems

It is a well known fact in electrical engineering that a linear electrical system is fully characterized by its impulse response as shown in Fig. 2.1. Applying a delta function to the input of the circuit and measuring its output characterizes the system. The output $y(t)$ to any kind of input signal $x(t)$ is then given by

$$y(t) = h(t) * x(t) = \int_{-\infty}^{+\infty} h(\theta)x(t-\theta)d\theta, \tag{2.1}$$

where $h(t)$ is the impulse response of the linear system and $*$ denotes time convolution. The transfer function of the system is given by the Fourier transform of the impulse response and characterizes the systems amplification of a time-harmonic input signal.

The same approach can be taken to characterize a linear acoustic system. The basic set-up is shown in Fig. 2.2. The acoustic radiator (transducer) on the left is mounted in a infinite rigid, baffle and its position is denoted by $\vec{r}_2$. It radiates into a homogeneous medium with a constant speed of sound c and density ρ_0 throughout the medium. The point denoted by $\vec{r}_1$ is where the acoustic pressure from the transducer is measured by a small point hydrophone. A voltage excitation of the transducer with a delta function will give rise to a pressure field that is measured by the hydrophone. The measured response is the acoustic impulse response for this particular system with the given set-up. Moving the transducer or the hydrophone to a new position will give a different response. Moving the hydrophone closer to the

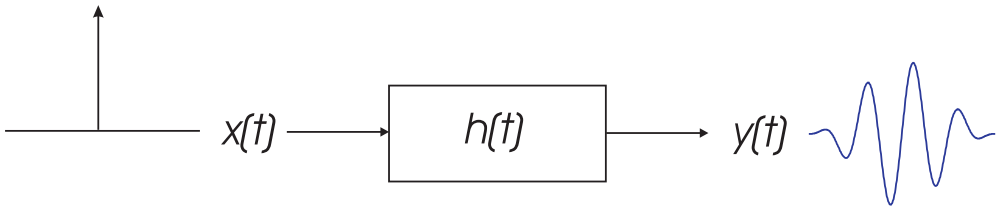

Figure 2.1: Measurement of impulse response for a linear electric system.

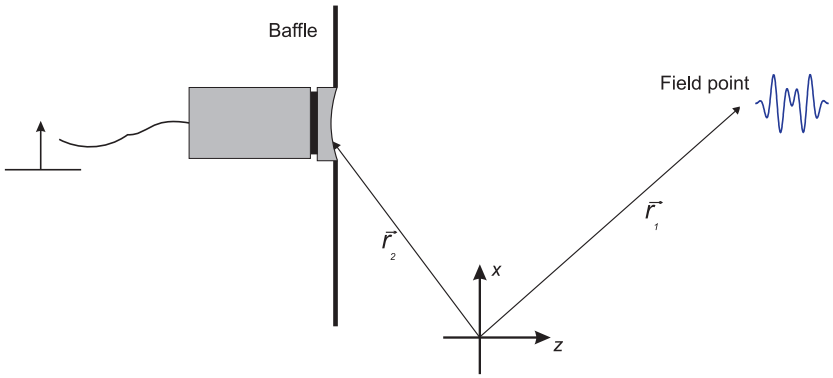

Figure 2.2: A linear acoustic system.

transducer surface will often increase the signal[1], and moving it away from the center axis of the transducer will often diminish it. Thus, the impulse response depends on the relative position of both the transmitter and receiver $(\vec{r}_2 - \vec{r}_1)$ and hence it is called a spatial impulse response.

A perception of the sound field for a fixed time instance can be obtained by employing Huygens' principle in which every point on the radiating surface is the origin of an outgoing spherical wave. This is illustrated in Fig. 2.3. Each of the outgoing spherical waves are given by

$$p_s(\vec{r}_1, t) = \delta\left(t - \frac{|\vec{r}_2 - \vec{r}_1|}{c}\right) = \delta\left(t - \frac{|r|}{c}\right) \tag{2.2}$$

where $\vec{r}_1$ indicates the point in space, $\vec{r}_2$ is the point on the transducer surface, and t is the time for the snapshot of the spatial distribution of the pressure. The spatial impulse response is then found by observing the pressure waves at a fixed position in space over time by having all the spherical waves pass the point of observation and summing them. Being on the acoustical axis of the transducer gives a short response whereas an off-axis point yields a longer impulse response as shown in Fig. 2.3.

2.2 Basic theory

In this section the exact expression for the spatial impulse response will more formally be derived. The basic setup is shown in Fig. 2.4. The triangularly shaped aperture is placed in an infinite, rigid baffle on which the velocity normal to the plane is zero, except at the aperture. The field point is denoted by $\vec{r}_1$ and the aperture by $\vec{r}_2$. The pressure field generated by the aperture is then found by the Rayleigh integral [10]

$$p(\vec{r}_1, t) = \frac{\rho_0}{2\pi} \int_S \frac{\frac{\partial v_n(\vec{r}_2, t - \frac{|\vec{r}_1 - \vec{r}_2|}{c})}{\partial t}}{|\ \vec{r}_1 - \vec{r}_2\ |} dS, \tag{2.3}$$

where v_n is the velocity normal to the transducer surface. The integral is a statement of Huyghens' principle that the field is found by integrating the contributions from all the infinitesimally small area elements that make up the aperture. This integral formulation assumes linearity and propagation in a homogeneous medium without attenuation. Further, the radiating aperture is assumed flat, so no re-radiation from scattering and reflection takes place. Exchanging the integration and the partial derivative, the integral can be written as

$$p(\vec{r}_1, t) = \frac{\rho_0}{2\pi} \frac{\partial \int_S \frac{v_n(\vec{r}_2, t - \frac{|\vec{r}_1 - \vec{r}_2|}{c})}{|\ \vec{r}_1 - \vec{r}_2\ |} dS}{\partial t}. \tag{2.4}$$

[1] This is not always the case. It depends on the focusing of the transducer. Moving closer to the transducer but away from its focus will decrease the signal.

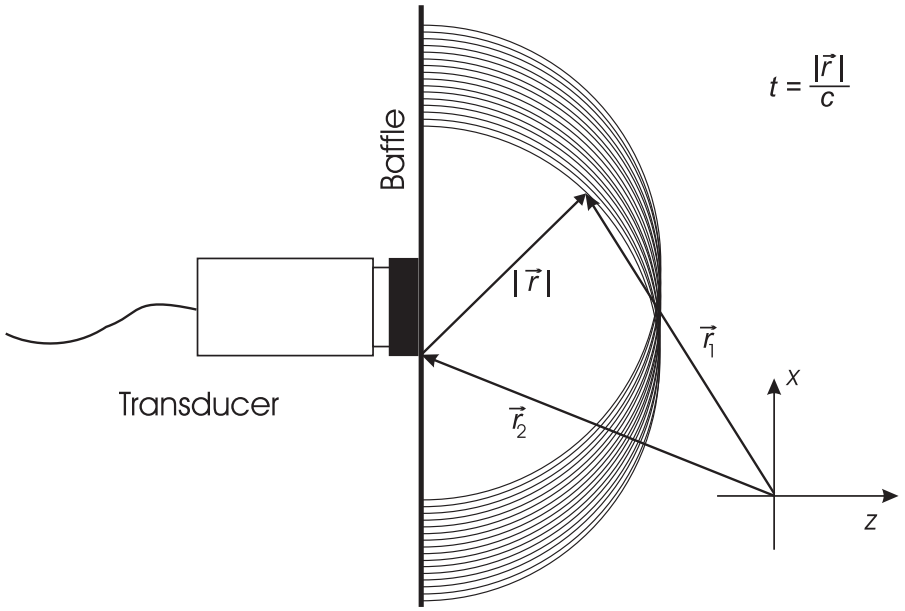

Figure 2.3: Illustration of Huygens' principle for a fixed time instance. A spherical wave with a radius of $|\vec{r}| = ct$ is radiated from each point on the aperture.

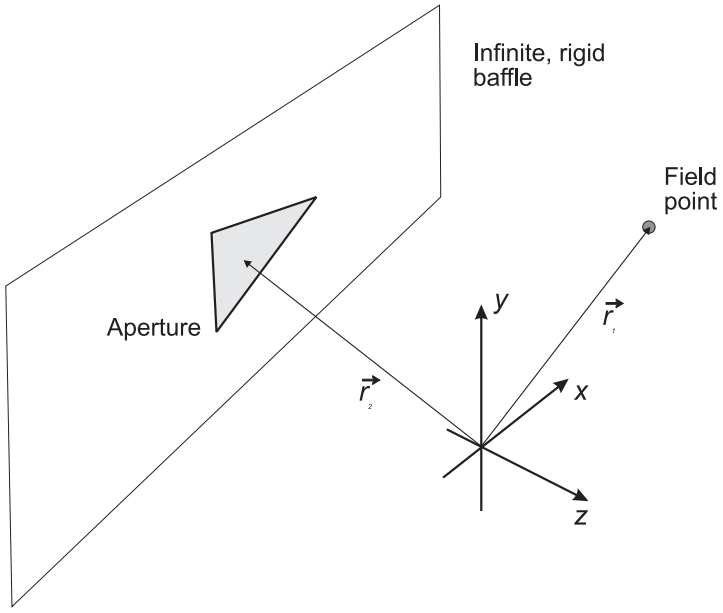

Figure 2.4: Position of transducer, field point, and coordinate system.

It is convenient to introduce the velocity potential ψ that satisfies the equations [11]

$$\begin{aligned} \vec{v}(\vec{r},t) &= -\nabla\psi(\vec{r},t) \\ p(\vec{r},t) &= \rho_0 \frac{\partial\psi(\vec{r},t)}{\partial t}. \end{aligned} \tag{2.5}$$

Then only a scalar quantity need to be calculated and all field quantities can be derived from it. The surface integral is then equal to the velocity potential:

$$\psi(\vec{r}_1,t) = \int_S \frac{v_n(\vec{r}_2, t - \frac{|\vec{r}_1-\vec{r}_2|}{c})}{2\pi \mid \vec{r}_1 - \vec{r}_2 \mid} dS \tag{2.6}$$

The excitation pulse can be separated from the transducer geometry by introducing a time convolution with a delta function as

$$\psi(\vec{r}_1,t) = \int_S \int_T \frac{v_n(\vec{r}_2,t_2)\delta(t - t_2 - \frac{|\vec{r}_1-\vec{r}_2|}{c})}{2\pi \mid \vec{r}_1 - \vec{r}_2 \mid} dt_2 dS, \tag{2.7}$$

where δ is the Dirac delta function.

Assume now that the surface velocity is uniform over the aperture making it independent of $\vec{r}_2$, then:

$$\psi(\vec{r}_1,t) = v_n(t) * \int_S \frac{\delta(t - \frac{|\vec{r}_1-\vec{r}_2|}{c})}{2\pi \mid \vec{r}_1 - \vec{r}_2 \mid} dS, \tag{2.8}$$

where $*$ denotes convolution in time. The integral in this equation

$$h(\vec{r}_1,t) = \int_S \frac{\delta(t - \frac{|\vec{r}_1-\vec{r}_2|}{c})}{2\pi \mid \vec{r}_1 - \vec{r}_2 \mid} dS \tag{2.9}$$

is called the spatial impulse response and characterizes the three-dimensional extent of the field for a particular transducer geometry. Note that this is a function of the relative position between the aperture and the field.

Using the spatial impulse response the pressure is written as

$$p(\vec{r}_1,t) = \rho_0 \frac{\partial v_n(t)}{\partial t} * h(\vec{r}_1,t) \tag{2.10}$$

which equals the emitted pulsed pressure for any kind of surface vibration $v_n(t)$. The continuous wave field can be found from the Fourier transform of (2.10). The received response for a collection of scatterers can also be found from the spatial impulse response [12], [6]. This is derived in Section 2.6. Thus, the calculation of the spatial impulse response makes it possible to find all ultrasound fields of interest.

2.2.1 Geometric considerations

The calculation of the spatial impulse response assumes linearity and any complex-shaped transducer can therefore be divided into smaller apertures and the response can be found by adding the responses from the sub-apertures. The integral is, as mentioned before, a statement of Huyghens' principle of summing contributions from all areas of the aperture.

An alternative interpretation is found by using the acoustic reciprocity theorem [13]. This states that: "If in an unchanging environment the locations of a small source and a small receiver are interchanged, the received signal will remain the same." Thus, the source and receiver can be interchanged. Emitting a spherical wave from the field point and finding the wave's intersection with the aperture also yields the spatial impulse response. The situation is depicted in Fig. 2.5, where an outgoing spherical wave is emitted from the origin of the coordinate system. The dashed curves indicate the circles from the projected spherical wave.

The calculation of the impulse response is then facilitated by projecting the field point onto the plane of the aperture. The task is thereby reduced to a two-dimensional problem and the field point is given as a (x, y) coordinate set and a

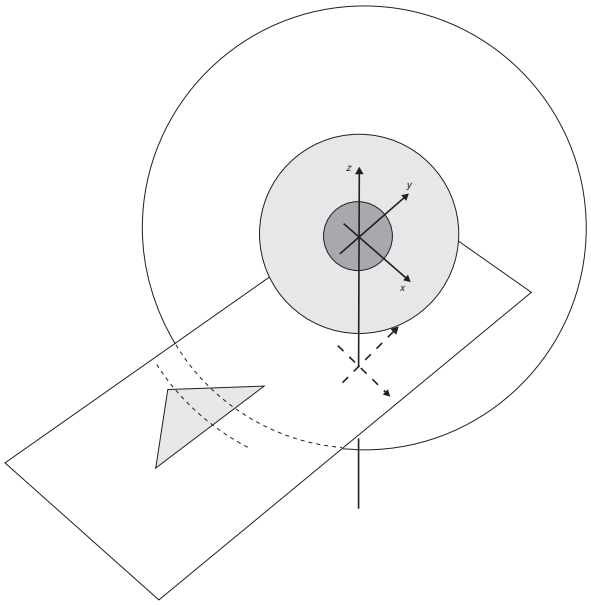

Figure 2.5: Emission of a spherical wave from the field point and its intersection of the aperture.

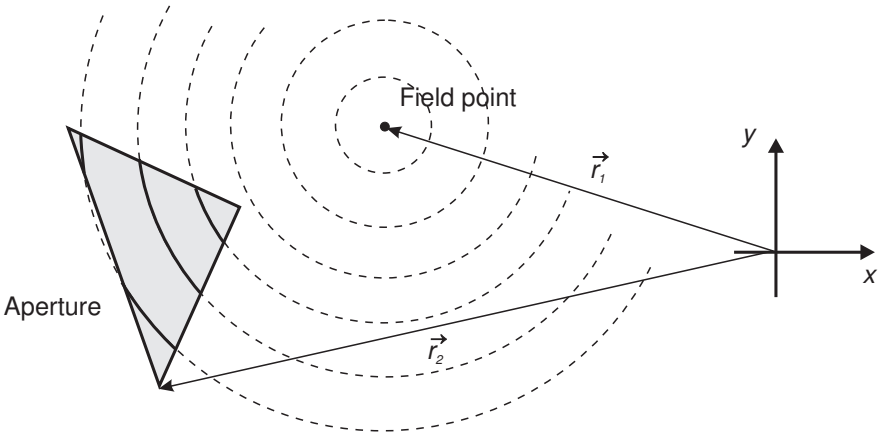

Figure 2.6: Intersection of spherical waves from the field point by the aperture, when the field point is projected onto the plane of the aperture.

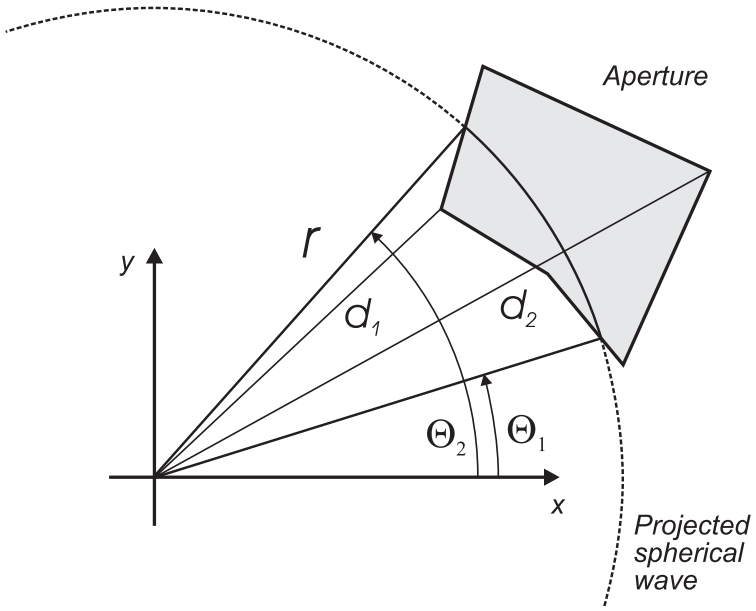

Figure 2.7: Definition of distances and angles in the aperture plan for evaluating the Rayleigh integral.

height z above the plane. The three-dimensional spherical waves are then reduced to circles in the $x-y$ plane with the origin at the position of the projected field point as shown in Fig. 2.6.

The spatial impulse response is, thus, determined by the relative length of the part of the arc that intersects the aperture. Thereby it is the crossing of the projected spherical waves with the edges of the aperture that determines the spatial impulse responses. This fact is used for deriving equations for the spatial impulse responses in the next section.

2.3 Calculation of spatial impulse responses

The spatial impulse response is found from the Rayleigh integral derived earlier

$$h(\vec{r}_1,t)=\int_S \frac{\delta(t-\frac{|\vec{r}_1-\vec{r}_2|}{c})}{2\pi\mid \vec{r}_1-\vec{r}_2\mid} dS \tag{2.11}$$

The task is to project the field point onto the plane coinciding with the aperture, and then find the intersection of the projected spherical wave (the circle) with the active aperture as shown in Fig. 2.6.

Rewriting the integral into polar coordinates gives:

$$h(\vec{r}_1,t)=\int_{\Theta_1}^{\Theta_2}\int_{d_1}^{d_2} \frac{\delta(t-\frac{R}{c})}{2\pi R} r\, dr\, d\Theta \tag{2.12}$$

where r is the radius of the projected circle and R is the distance from the field point to the aperture given by $R^2=r^2+z_p^2$. Here z_p is the field point height above the $x-y$ plane of the aperture. The projected distances d_1, d_2 are determined by the aperture and are the distance closest to and furthest away from the aperture, and Θ_1, Θ_2 are the corresponding angles for a given time (see Fig. 2.7).

Introducing the substitution $2RdR=2rdr$ gives

$$h(\vec{r}_1,t)=\frac{1}{2\pi}\int_{\Theta_1}^{\Theta_2}\int_{R_1}^{R_2} \delta(t-\frac{R}{c})\, dR\, d\Theta \tag{2.13}$$

The variables R_1 and R_2 denote the edges closest to and furthest away from the field point. Finally using the substitution $t' = R/c$ gives

$$h(\vec{r}_1, t) = \frac{c}{2\pi} \int_{\Theta_1}^{\Theta_2} \int_{t_1}^{t_2} \delta(t - t') dt' d\Theta \tag{2.14}$$

For a given time instance the contribution along the arc is constant and the integral gives

$$h(\vec{r}_1, t) = \frac{\Theta_2 - \Theta_1}{2\pi} c \tag{2.15}$$

when assuming the circle arc is only intersected once by the aperture. The angles Θ_1 and Θ_2 are determined by the intersection of the aperture and the projected spherical wave, and the spatial impulse response is, thus, solely determined by these intersections, when no apodization of the aperture is used. The response can therefore be evaluated by keeping track of the intersections as a function of time.

2.3.1 A simple calculation procedure

From the derivation in the last section it can be seen that the spatial impulse response in general can be expressed as

$$h(\vec{r}_1, t) = \frac{c}{2\pi} \sum_{i=1}^{N(t)} \left[\Theta_2^{(i)}(t) - \Theta_1^{(i)}(t) \right] \tag{2.16}$$

where $N(t)$ is the number of arc segments that crosses the boundary of the aperture for a given time and $\Theta_2^{(i)}(t), \Theta_1^{(i)}(t)$ are the associated angles of the arc. This was also noted by Stepanishen [14]. The calculation can, thus, be formulated as finding the angles of the aperture edge's intersections with the projected spherical wave, sorting the angles, and then summing the arc angles that belong to the aperture. Finding the intersections can be done from the description of the edges of the aperture. A triangle can be described by three lines, a rectangle by four, and the intersections are then found from the intersections of the circle with the lines. This makes it possible to devise a general procedure for calculating spatial impulse responses for any flat, bounded aperture, since the task is just to find the intersections of the boundary with the circle.

The spatial impulse response is calculated from the time the aperture first is intersected by a spherical wave to the time for the intersection furthest away. The intersections are found for every time instance and the corresponding angles are sorted. The angles lie in the interval from 0 to 2π. It is then found whether the arc between two angles belongs to the aperture, and the angle difference is added to the sum, if the arc segment is inside the aperture. This yields the spatial impulse response according to Eq. (2.16). The approach can be described by the flow chart shown in Fig. 2.8.

The only part of the algorithm specific to the aperture is the determination of the intersections and whether the point is inside the aperture. Section 2.3.2 shows how this is done for polygons, Section 2.3.3 for circles, and Section 2.3.6 for higher-order parametric boundaries.

All the intersections need not be found for all times. New intersections are only introduced, when a new edge or corner of the aperture is met. Between times when two such corners or edges are encountered the number of intersections remains constant and only intersections, which belong to points inside the aperture need to be found. Note that an aperture edge gives rise to a discontinuity in the spatial impulse response. Also testing whether the point is inside the aperture is often superfluous, since this only needs to be found once after each discontinuity in the response. These two observations can significantly reduce the number of calculations, since only the intersections affecting the response are found.

The procedure first finds the number of discontinuities. Then only intersection influencing the response are calculated between two discontinuity points. This can potentially make the approach faster than the traditional approach, where the response from a number of different rectangles or triangles must be calculated.

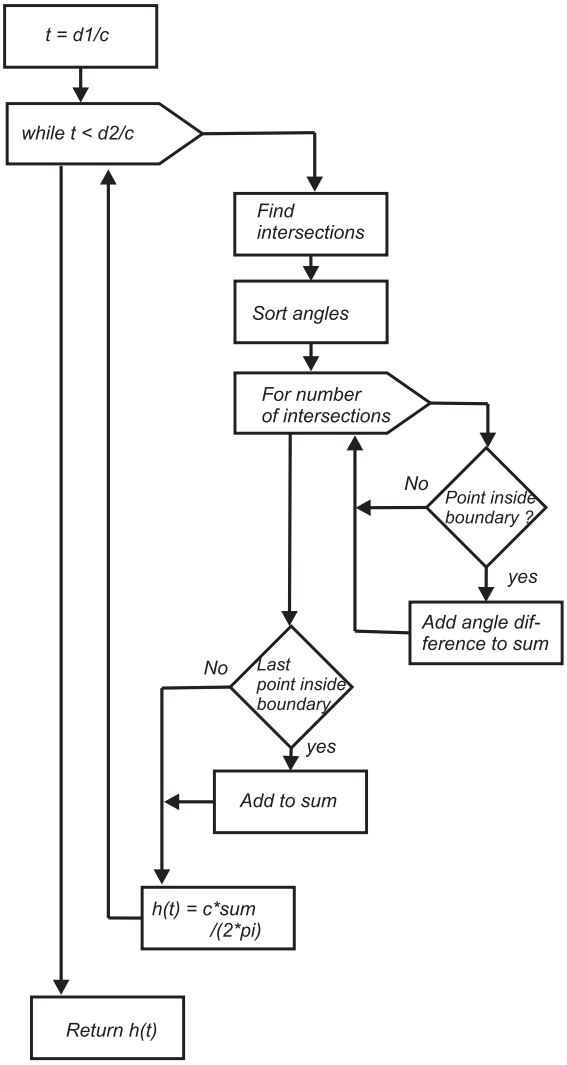

Figure 2.8: Flow chart for calculating the spatial impulse response.

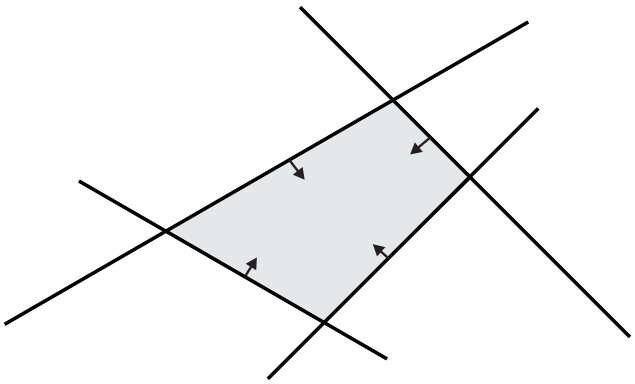

Figure 2.9: Definition of bounding lines for polygon transducer. The arrows indicate the half-planes for the active aperture.

2.3.2 Solution for polygons

The boundary of any polygon can be defined by a set of bounding lines as shown in Fig. 2.9.

The active aperture is then defined as lying on one side of the line as indicated by the arrows, and a point on the aperture must be placed correctly in relation to all lines. The test whether a point is on the aperture is thus to go through all lines and test whether the point lies in the active half space for the line, and stop if it is not. The point is inside the aperture, if it passes the test for all the lines.

The intersections are found from the individual intersections between the projected circle and the lines. They are determined from the equations for the projected spherical wave and the line:

$$\begin{aligned} r^2 &= (x-x_0)^2 + (y-y_0)^2 \\ y &= \alpha x + y_1 \\ r^2 &= (ct)^2 - z_p^2 \end{aligned} \tag{2.17}$$

Here (x_0, y_0) is the center of the circle, α the slope of the line, and y_1 its intersect with the y-axis. The intersections are given from the solutions to:

$$\begin{aligned} 0 &= (1+\alpha^2)x^2 + (2\alpha y_1 - 2x_0 - 2y_0\alpha)x + (y_0^2 + y_1^2 + x_0^2 - 2y_0 y_1 - r^2) \\ &= Ax^2 + Bx + C \\ D &= B^2 - 4AC \end{aligned} \tag{2.18}$$

The angles are

$$\Theta = \arctan\left(\frac{y-y_0}{x-x_0}\right) \tag{2.19}$$

Intersections between the line and the circle are only found if $D > 0$. A determinant $D < 0$ indicates that the circle did not intersect the line. If the line has infinite slope, the solution is found from the equation:

$$\begin{aligned} x &= x_1 \\ 0 &= y^2 - 2y_0 y + y_0^2 + (x_1 - x_0)^2 - r^2 \\ &= A_\infty y^2 + B_\infty y + C_\infty \end{aligned} \tag{2.20}$$

in which $A_\infty, B_\infty, C_\infty$ replace A, B, C, respectively, and the solutions are found for y rather than x. Here x_1 is the line's intersection with the x-axis.

The times for discontinuities in the spatial impulse response are given by the intersections of the lines that define the aperture's edges and by the minimum distance from the projected field point to the lines. The minimum distance is

found from a line passing through the field point that is orthogonal to the bounding line. The intersection between the orthogonal line and the bounding line is:

$$\begin{aligned} x &= \frac{\alpha y_p + x_p - \alpha y_1}{\alpha^2 + 1} \\ y &= \alpha x + y_1 \end{aligned} \tag{2.21}$$

where (x_p, y_p, z_p) is the position of the field point. For an infinite slope line the solution is $x = x_1$ and $y = y_p$. The corresponding time is:

$$t_i = \frac{\sqrt{(x - x_p)^2 + (y - y_p)^2 + z_p^2}}{c} \tag{2.22}$$

The intersections of the lines are also found, and the corresponding times are calculated by (2.22) and sorted in ascending order. They indicate the start and end time for the response and the time points for discontinuities in the response.

2.3.3 Solution for circular surfaces

The other basic shape for a transducer apart from rectangular shapes is the flat, round surface used for single element piston transducers and annular arrays. For these the intersections are determined by two circles as depicted in Fig. 2.10.

Here O_1 is the center of the aperture with radius r_a and the projected spherical wave is centered at O_2 with radius $r_b(t) = \sqrt{(ct)^2 - z_p^2}$. The length $h_a(t)$ is given by [15, page 66]

$$\begin{aligned} h_a(t) &= \frac{2\sqrt{p(t)(p(t) - a)(p(t) - r_a)(p(t) - r_b(t))}}{a} \\ a &= ||O_1 - O_2|| \\ p(t) &= \frac{a + r_a + r_b(t)}{2} \end{aligned} \tag{2.23}$$

In a coordinate system centered at O_1 and an x-axis in the $O_1 - O_2$ direction, the intersections are at

$$\begin{aligned} y &= h_a(t) \\ l &= \pm\sqrt{r_b^2(t) - h_a^2(t)} \end{aligned} \tag{2.24}$$

The sign for l depends on the position of the intersections. A negative sign is used if the intersections are for negative values of x, and positive sign is used for positive x positions.

When the field point is outside the active aperture the spatial impulse response is

$$\begin{aligned} h(\vec{r}_1, t) &= \frac{|\Theta_2 - \Theta_1|}{2\pi} c = \frac{c}{\pi} \arctan\left(\frac{h_a(t)}{l}\right) \\ \Theta_2 &= \arctan\left(\frac{h_a(t)}{l}\right) = -\Theta_1 \end{aligned} \tag{2.25}$$

It must be noted that a proper four-quadrant arc-tan should be used to give the correct response. An alternative formula is [16, page 19]

$$\begin{aligned} h(\vec{r}_1, t) &= \frac{c}{2\pi} \arcsin\left(\frac{2\sqrt{p(t)(p(t) - a)(p(t) - r_a)(p(t) - r_b(t))}}{r_b^2(t)}\right) \\ &= \frac{c}{2\pi} \arcsin\left(\frac{a h_a(t)}{r_b^2(t)}\right) \end{aligned} \tag{2.26}$$

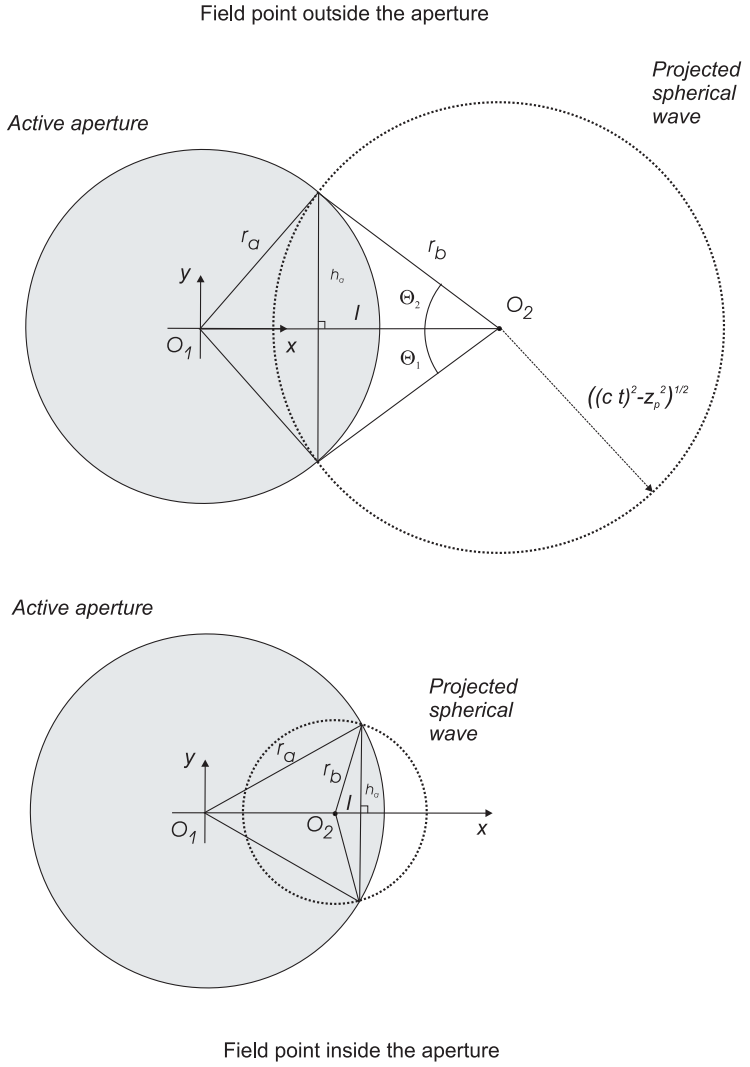

Figure 2.10: Geometry for determining intersections between circles. The top graph shows the geometry when the field point denoted by O_2 is outside the aperture, and the bottom graph when it is inside.

The start time t_s for the response is found from

$$\begin{aligned} r_a + r_b(t) &= ||O_1 - O_2|| \\ t_s &= \frac{\sqrt{r_b^2(t) + z_p^2}}{c} = \frac{\sqrt{(||O_1 - O_2|| - r_a)^2 + z_p^2}}{c} \end{aligned} \tag{2.27}$$

and the response ends at the time t_e when

$$\begin{aligned} r_b(t) &= r_a + ||O_1 - O_2|| \\ t_e &= \frac{\sqrt{r_b^2(t) + z_p^2}}{c} = \frac{\sqrt{(||O_1 - O_2|| + r_a)^2 + z_p^2}}{c} \end{aligned} \tag{2.28}$$

When the field point is inside the aperture, the response is

$$h(\vec{r}_1, t) = c \quad \text{for} \quad \frac{z_p}{c} \leq t \leq \frac{\sqrt{(r_a - ||O_1 - O_2||)^2 + z_p^2}}{c} \tag{2.29}$$

thereafter the arc lying outside the aperture should be subtracted, so that

$$h(\vec{r}_1, t) = \frac{2\pi - |\Theta_2 - \Theta_1|}{2\pi} c \tag{2.30}$$

The response ends when

$$\begin{aligned} r_b(t) &= r_a + ||O_1 - O_2|| \\ t_e &= \frac{\sqrt{(||O_1 - O_2|| + r_a)^2 + z_p^2}}{c} \end{aligned} \tag{2.31}$$

The determination of which part of the arc that subtracts or adds to the response is determined by what the active aperture is. One ring in an annular array can be defined as consisting of an active aperture outside a circle combined with an active aperture inside a circle for defining the inner and outer rim of the aperture. A circular aperture can also be combined with a line for defining the active area of a split aperture used for continuous wave probing.

2.3.4 Solution for a circular concave surface

For reference the expression for a concave transducer, which is a type often used in medical ultrasonics, is given. A derivation of the solution can be found in [17] and [18].

The spatial impulse response is [17]:

$$h_c(\vec{r}_1, t) = \begin{cases} & \text{Region I} & & & \text{Region II} \\ & \underline{z < 0} & & \underline{z > 0} & \\ 0 & ct < r_0 & r_0 < ct & & ct < r_1 \\ \frac{cR}{r} & r_0 < ct < r_1 & r_2 < ct < r_0 & & - \\ \frac{cR}{r}\frac{1}{\pi}\arccos\frac{\eta(t)}{\sigma(t)} & r_1 < ct < r_2 & r_1 < ct < r_2 & & r_1 < ct < r_2 \\ 0 & r_2 < ct & & ct < r_1 & r_2 < ct \end{cases} \tag{2.32}$$

where:

$$\begin{aligned} \eta(t) &= R\left\{\frac{1 - d/R}{\sin\Theta} + \frac{1}{\tan\Theta}\left(\frac{R^2 + r^2 - c^2t^2}{2rR}\right)\right\} \\ \sigma(t) &= R\sqrt{1 - \left(\frac{R^2 + r^2 - c^2t^2}{2rR}\right)^2} \\ r &= |\vec{r}_1\,|. \end{aligned} \tag{2.33}$$

The variables are defined in Fig. 2.11.

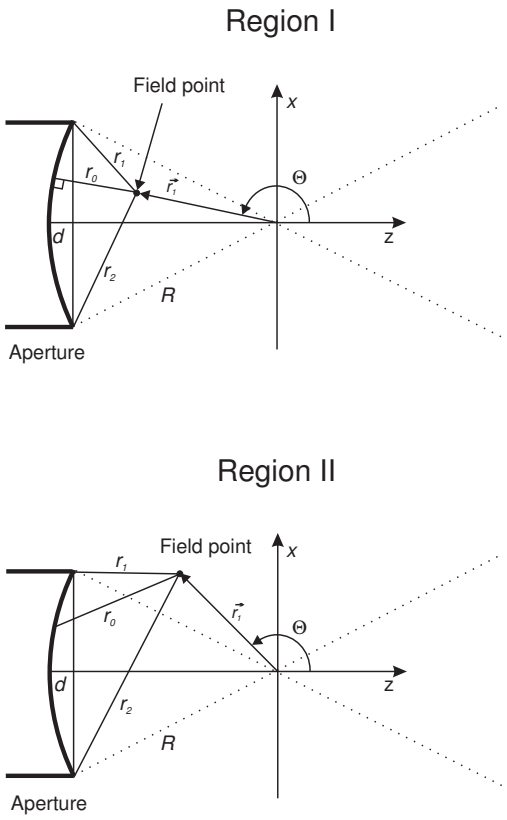

Figure 2.11: Definition of variables for spatial impulse response of concave transducer.

2.3.5 Solution for other surfaces

Analytical solutions for spatial impulse response have been derived for a number of different geometries by various authors. The response from a flat rectangle can be found in [19, 20], and for a flat triangle in [21]).

2.3.6 Solution for parametric surfaces

For ellipses or other higher order parametric surfaces it is in general not easy to find analytic solutions for the spatial impulse response. The boundary method described above can, however, be used for providing a simple solution to the problem, since the intersections between the projected spherical wave and the edge of the aperture uniquely determine the spatial impulse response. It is therefore possible to use root finding for a set of (non-linear) equations for finding these intersections. The problem is to find when both the spherical wave and the aperture have crossing contours in the plane of the aperture, *i.e.*, when

$$\begin{aligned} (ct)^2 - z_p^2 - (x - x_p)^2 - (y - y_p)^2 &= 0 \\ S(x, y) &= 0 \end{aligned} \tag{2.34}$$

in which $S(x, y) = 0$ defines the boundary of the aperture. The problem of numerically finding these roots is in general not easy, if a good initial guess on the position of the intersections is not found [22, pages 286–289]. Good initial values are however found here, since the intersections must lie on the projected circle and the intersections only move slightly from time point to time point. An efficient Newton-Raphson algorithm can therefore be devised for finding the intersections, and the procedure detailed here can be used to find the spatial impulse response for any flat transducer geometry with an arbitrary apodization and both hard and soft baffle mounting.

2.4 Apodization and soft baffle

Often ultrasound transducers do not vibrate as a piston over the aperture. This can be due to the clamping of the active surface at its edges, or intentionally to reduce side-lobes in the field. Applying for example a Gaussian apodization will significantly lower side lobes and generate a field with a more uniform point spread function as a function of depth. Apodization is introduced in (2.12) by writing [23]

$$h(\vec{r}_1, t) = \int_{\Theta_1}^{\Theta_2} \int_{d_1}^{d_2} a_p(r, \Theta) \frac{\delta(t - \frac{R}{c})}{2\pi R} r \, dr \, d\Theta \tag{2.35}$$

in which $a_p(r, \Theta)$ is the apodization over the aperture. Using the same substitutions as before yields

$$h(\vec{r}_1, t) = \frac{c}{2\pi} \int_{\Theta_1}^{\Theta_2} \int_{t_1}^{t_2} a_{p1}(t', \Theta) \delta(t - t') \, dt' \, d\Theta \tag{2.36}$$

where $a_{p1}(t', \Theta) = a_p(\sqrt{(ct')^2 - z_p^2}, \Theta)$. The inner integral is a convolution of the apodization function with a δ-function and readily yields

$$h(\vec{r}_1, t) = \frac{c}{2\pi} \int_{\Theta_1}^{\Theta_2} a_{p1}(t, \Theta) \, d\Theta \tag{2.37}$$

as noted by several authors [23, 24, 25]. The response for a given time instance can, thus, be found by integrating the apodization function along the fixed arc with a radius of $r = \sqrt{(ct)^2 - z_p^2}$ for the angles for the active aperture. Any apodization function can therefore be incorporated into the calculation by employing numerical integration.

Often the assumption of an infinite rigid baffle for the transducer mounting is not appropriate and another form of the Rayleigh integral must be used. For a soft baffle, in which the pressure on the baffle surface is zero, the Rayleigh-Sommerfeld integral is used. This is [26, pages 46–50]

$$h_s(\vec{r}_1, t) = \int_S \frac{\delta(t - \frac{|\vec{r}_1 - \vec{r}_2|}{c})}{2\pi \mid \vec{r}_1 - \vec{r}_2 \mid} \cos\varphi \, dS \tag{2.38}$$

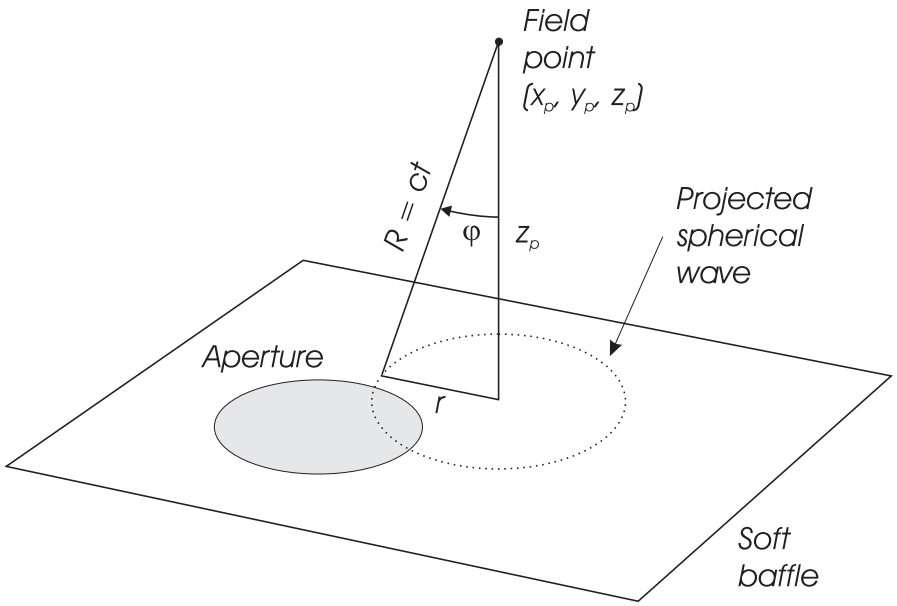

Figure 2.12: Definition of angle used for a soft baffle.

assuming that $|\vec{r}_1 - \vec{r}_2| \gg \lambda$. Here $\cos\varphi$ is the angle between the line through the field point orthogonal to the aperture plane and the radius of the spherical wave as shown in Fig. 2.12.

The angle φ is constant for a given radius of the projected spherical wave and thus for a given time. It is given by

$$\cos\varphi = \frac{z_p}{R} = \frac{z_p}{ct} \tag{2.39}$$

Using the substitutions from Section 2.2, the Rayleigh-Sommerfeld integral can then be rewritten as

$$h_s(\vec{r}_1, t) = \frac{z_p}{2\pi} c(\Theta_2 - \Theta_1) \int_{t_1}^{t_2} \frac{\delta(t - t')}{ct'}\, dt' \tag{2.40}$$

Using the property of the δ-function that

$$\int_{-\infty}^{+\infty} g(t')\delta(t - t')\, dt' = g(t) \tag{2.41}$$

then gives

$$h_s(\vec{r}_1, t) = \frac{z_p}{ct} \frac{\Theta_2 - \Theta_1}{2\pi} c = \frac{z_p}{ct} h(\vec{r}_1, t). \tag{2.42}$$

The spatial impulse response can, thus, be found from the spatial impulse response for the rigid baffle case by multiplying with $z_p/(ct)$.

2.5 Examples of spatial impulse responses

The first example shows the spatial impulse responses from a 3×5 mm rectangle for different spatial positions 5 mm from the front face of the transducer. The responses are found from the center of the rectangle $(y = 0)$ and out in steps of 2 mm in the x direction to 6 mm away from the center of the rectangle. A schematic diagram of the situation is shown in Fig. 2.13 for the on-axis response. The impulse response is zero before the first spherical wave reaches the aperture. Then the response stays constant at a value of c. The first edge of the aperture is met, and the response drops

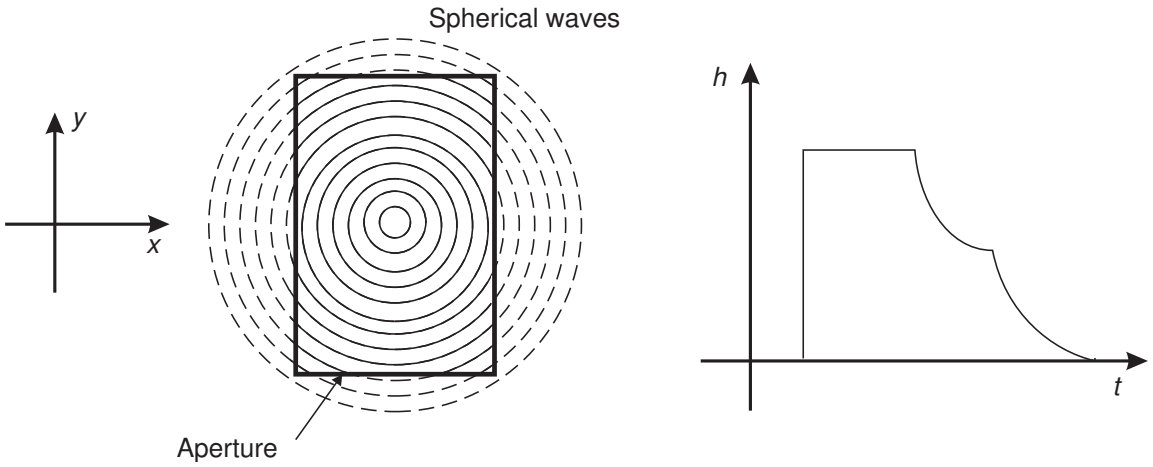

Figure 2.13: Schematic diagram of field from rectangular element.

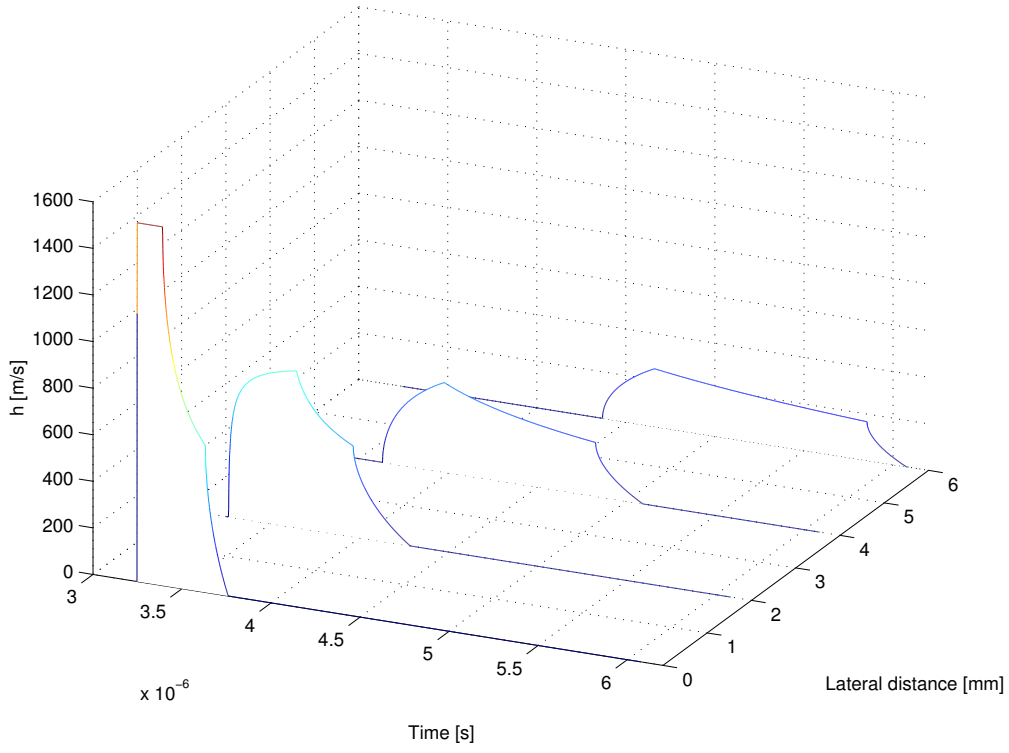

Figure 2.14: Spatial impulse response from a rectangular aperture of 4×5 mm at for different lateral positions

of. The decrease with time in increased when the next edge of the aperture is reached and the response becomes zero when the projected spherical waves all are outside the area of the aperture.

A plot of the results for the different lateral field positions is shown in Fig. 2.14. It can be seen how the spatial impulse response changes as a function of relative position to the aperture.

The second example shows the response from a circular, flat transducer. Two different cases are shown in Fig. 2.15. The top graph shows the traditional spatial impulse response when no apodization is used, so that the aperture vibrates as a piston. The field is calculated 10 mm from the front face of the transducer starting at the center axis of the aperture. Twenty-one responses for lateral distance of 0 to 20 mm off axis are then shown. The same calculation is repeated in the bottom graph, when a Gaussian apodization has been imposed on the aperture. The vibration amplitude is a factor of $1/\exp(4)$ less at the edges of the aperture than at the center. It is seen how the apodization reduces some of the sharp discontinuities in the spatial impulse response, which can reduce the sidelobes of the field.

2.6 Calculation of the scattered signal

In medical ultrasound, a pulsed field is emitted into the body and is scattered and reflected by density and propagation velocity perturbations. The scattered field then propagates back through the tissue and is received by the transducer. The field is converted to a voltage signal and used for the display of the ultrasound image. A full description of a typical imaging system, using the concept of spatial impulse response, is the purpose of the section.

The received signal can be found by solving an appropriate wave equation. This has been done in a number of papers (e.g. [27], [28]). Gore and Leeman [27] considered a wave equation where the scattering term was a function of the adiabatic compressibility and the density. The transducer was modeled by an axial and lateral pulse that were separable. Fatemi and Kak [28] used a wave equation where scattering originated only from velocity fluctuations, and the transducer was restricted to be circularly symmetric and unfocused (flat).

The scattering term for the wave equation used here is a function of density and propagation velocity perturbations, and the wave equation is equivalent to the one used by Gore and Leeman [27]. No restrictions are enforced on the transducer geometry or its excitation, and analytic expressions for a number of geometries can be incorporated into the model.

The model includes attenuation due to propagation and scattering, but not the dispersive attenuation observed for propagation in tissue. This can, however, be incorporated into the model as indicated in Section 2.6.6.

The derivation is organized as follows. The following section derives the wave equation and describes the different linearity assumptions made. Section 2.6.2 calculates the scattered field and section 2.6.3 introduces the spatial impulse response model for the incident field. Section 2.6.4 combines the wave equation solution and the transducer model to give the final equation for the received pressure field. To indicate the precision of the model, a single example of a predicted pressure field compared to measured field is given in Section 2.6.5.

2.6.1 Derivation of the wave equation

This section derives the wave equation. The section has been included in order to explain in detail the different linearity assumptions and approximations made to obtain a solvable wave equation. The derivation closely follows that developed by Chernov (1960).

The first approximation states that the instantaneous acoustic pressure and density can be written

$$P_{ins}(\vec{r},t) = P + p_1(\vec{r},t) \tag{2.43}$$

$$\rho_{ins}(\vec{r},t) = \rho(\vec{r}) + \rho_1(\vec{r},t) \tag{2.44}$$

in which P is the mean pressure of the medium and ρ is the density of the undisturbed medium. Here p_1 is the pressure

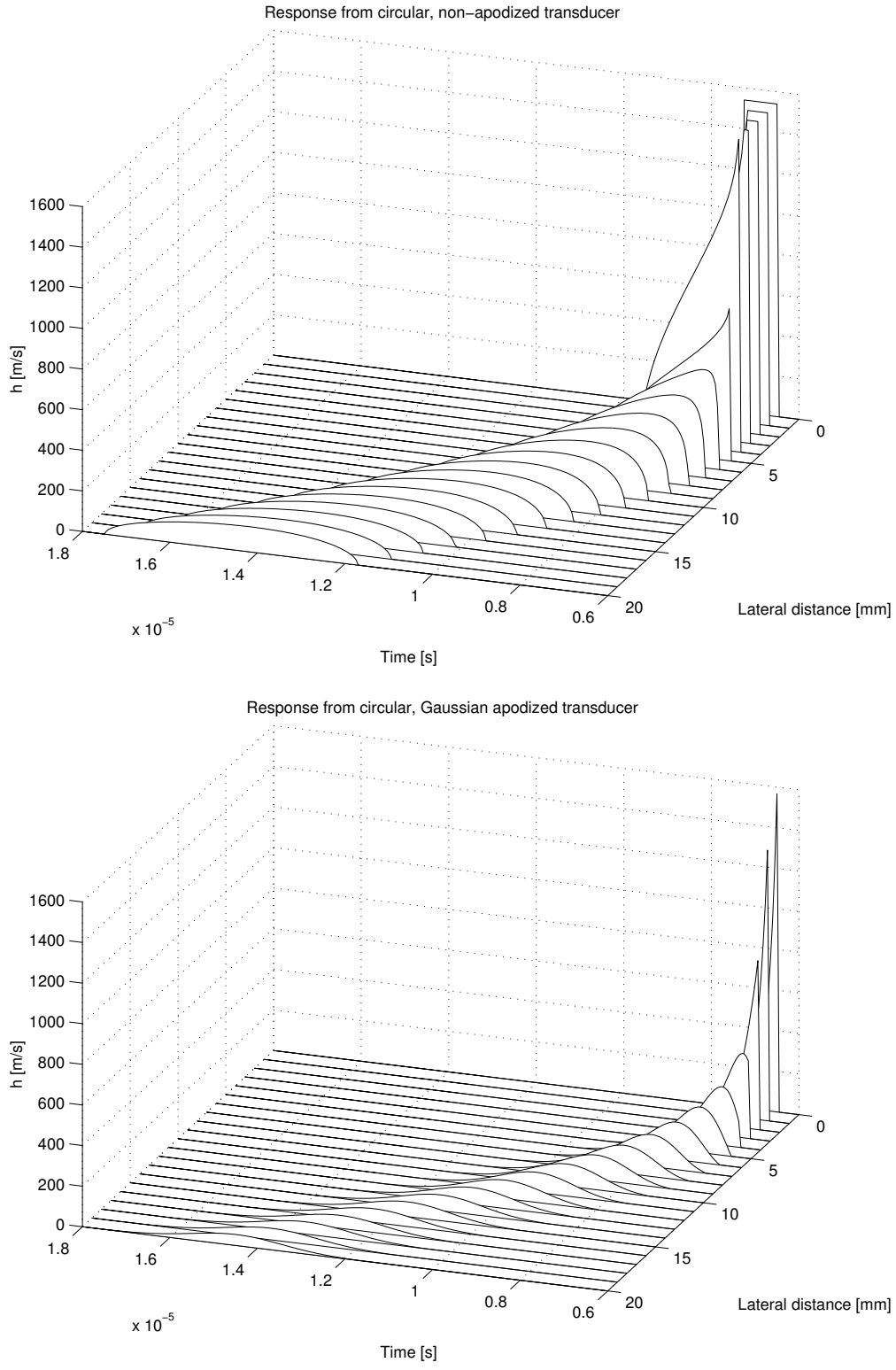

Figure 2.15: Spatial impulse response from a circular aperture. Graphs are shown without apodization of the aperture (top) and with a Gaussian apodization function (bottom). The radius of the aperture is 5 mm and the field is calculated 10 mm from the transducer surface.

variation caused by the ultrasound wave and is considered small compared to P and ρ_1 is the density change caused by the wave. Both p_1 and ρ_1 are small quantities of first order.

Our second assumption is that no heat conduction or conversion of ultrasound to thermal energy take place. Thus, the entropy is constant for the process, so that the acoustic pressure and density satisfy the adiabatic equation [29]:

$$\frac{dP_{ins}}{dt} = c^2 \frac{d\rho_{ins}}{dt} \tag{2.45}$$

The equation contains total derivatives, as the relation is satisfied for a given particle of the tissue rather than at a given point in space. This is the Lagrange description of the motion [11]. For our purpose the Euler description is more appropriate. Here the coordinate system is fixed in space and the equation describes the properties of whatever particle of fluid there is at a given point at a given time. Converting to an Eulerian description results in the following constitutive equation [29], [11]:

$$\frac{1}{c^2}\frac{\partial p_1}{\partial t} = \frac{\partial \rho_1}{\partial t} + \vec{u} \cdot \nabla \rho \tag{2.46}$$

using that P and ρ do not depend on time and that ρ_1 is small compared to ρ. Here u is the particle velocity, ∇ is the gradient operator, and $\cdot$ symbolizes the scalar product.

The pressure, density, and particle velocity must also satisfy the hydrodynamic equations [29]:

$$\rho_{ins}\frac{d\vec{u}}{dt} = -\nabla P_{ins} \tag{2.47}$$

$$\frac{\partial \rho_{ins}}{\partial t} = -\nabla \cdot (\rho_{ins}\vec{u}) \tag{2.48}$$

which are the dynamic equation and the equation of continuity. Using (2.43) and (2.44) and discarding higher order terms we can write

$$\rho\frac{\partial \vec{u}}{\partial t} = -\nabla p_1 \tag{2.49}$$

$$\frac{\partial \rho_1}{\partial t} = -\nabla \cdot (\rho\vec{u}) \tag{2.50}$$

Differentiating (2.50) with respect to t and inserting (2.49) gives

$$\frac{\partial^2 \rho_1}{\partial^2 t} = -\nabla \cdot (\rho\frac{\partial \vec{u}}{\partial t}) = -\nabla \cdot (-\nabla p_1) = \nabla^2 p_1 \tag{2.51}$$

Differentiating (2.46) with respect to t

$$\frac{1}{c^2}\frac{\partial^2 p_1}{\partial^2 t} = \frac{\partial^2 \rho_1}{\partial^2 t} + \frac{\partial \vec{u}}{\partial t} \cdot \nabla \rho \tag{2.52}$$

and inserting (2.51) and (2.49) leads to

$$\nabla^2 p_1 - \frac{1}{c^2}\frac{\partial^2 p_1}{\partial^2 t} = \frac{1}{\rho}\nabla\rho \cdot \nabla p_1 \tag{2.53}$$

Assuming that the propagation velocity and the density only vary slightly from their mean values yields

$$\begin{aligned} \rho(\vec{r}) &= \rho_0 + \Delta\rho(\vec{r}) \\ c(\vec{r}) &= c_0 + \Delta c(\vec{r}) \end{aligned} \tag{2.54}$$

where $\rho_0 \gg \Delta\rho$ and $c_0 \gg \Delta c$.

$$\nabla^2 p_1 - \frac{1}{(c_0 + \Delta c)^2}\frac{\partial^2 p_1}{\partial^2 t} = \frac{1}{(\rho_0 + \Delta\rho)}\nabla(\rho_0 + \Delta\rho) \cdot \nabla p_1 \tag{2.55}$$

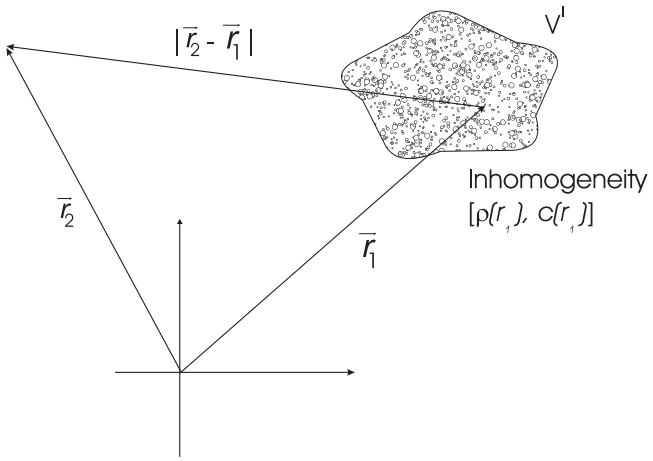

Figure 2.16: Coordinate system for calculating the scattered field

Ignoring small quantities of second order and using the approximation ($\Delta \ll 1$):

$$\frac{1}{1+\Delta} \approx 1 - \Delta \tag{2.56}$$

gives:

$$\nabla^2 p_1 - (\frac{1}{{c_0}^2} - \frac{2\Delta c}{{c_0}^3})\frac{\partial^2 p_1}{\partial^2 t} = \left(\frac{1}{\rho_0}\nabla(\Delta\rho) - \frac{\Delta\rho}{{\rho_0}^2}\nabla(\Delta\rho)\right) \cdot \nabla p_1 \tag{2.57}$$

Neglecting the second order term $(\Delta\rho/{\rho_0}^2)\nabla(\Delta\rho) \cdot \nabla p_1$ yields the wave equation:

$$\nabla^2 p_1 - \frac{1}{c_0^2}\frac{\partial^2 p_1}{\partial t^2} = -\frac{2\Delta c}{c_0^3}\frac{\partial^2 p_1}{\partial t^2} + \frac{1}{\rho_0}\nabla(\Delta\rho) \cdot \nabla p_1 \tag{2.58}$$

The two terms on the right side of the equation are the scattering terms which vanish for a homogeneous medium. The wave equation was derived by Chernov [29]. It has also been considered in Gore & Leeman [27] and Morse & Ingard [11] in a slightly different form, where the scattering terms were a function of the adiabatic compressibility κ and the density.

2.6.2 Calculation of the scattered field

Having derived a suitable wave equation, we now calculate the scattered field from a small inhomogeneity embedded in a homogeneous surrounding. The scene is depicted in Fig. 2.16. The inhomogeneity is identified by $\vec{r}_1$ and enclosed in the volume V'. The scattered field is calculated at the point indicated by $\vec{r}_2$ by integrating all the spherical waves emanating from the scattering region V' using the time dependent Green's function for unbounded space. Thus, the scattered field is [11], [27]:

$$p_s(\vec{r}_2, t) = \int_{V'}\int_T \left[\frac{1}{\rho_0}\nabla(\Delta\rho(\vec{r}_1)) \cdot \nabla p_1(\vec{r}_1, t_1) - \frac{2\Delta c(\vec{r}_1)}{c_0^3}\frac{\partial^2 p_1(\vec{r}_1, t_1)}{\partial t^2}\right] G(\vec{r}_1, t_1 \mid \vec{r}_2, t) dt_1 \, d^3\vec{r}_1 \tag{2.59}$$

where G is the free space Green's function:

$$G(\vec{r}_1, t_1 \mid \vec{r}_2, t) = \frac{\delta(t - t_1 - \frac{|\vec{r}_2 - \vec{r}_1|}{c_0})}{4\pi \mid \vec{r}_2 - \vec{r}_1 \mid} \tag{2.60}$$

$d^3\vec{r}_1$ means integrating w.r.t. $\vec{r}_1$ over the volume V', and T denotes integration over time.

We denote by

$$F_{op} = \frac{1}{\rho_0}\nabla(\Delta\rho(\vec{r}_1)) \cdot \nabla \quad - \frac{2\Delta c(\vec{r}_1)}{c_0^3}\frac{\partial^2}{\partial t^2} \tag{2.61}$$

the scattering operator.

The pressure field inside the scattering region is:

$$p_1(\vec{r}, t) = p_i(\vec{r}, t) + p_s(\vec{r}, t) \tag{2.62}$$

where p_i is the incident pressure field. As can be seen, the integral can not be solved directly. To solve it we apply the Born-Neumann expansion [30]. If G_i symbolizes the integral operator representing Green's function and the integration and F_{op} the scattering operator, then the first order Born approximation can be written:

$$p_{s_1}(\vec{r}_2, t) = G_i F_{op}\, p_i(\vec{r}_1, t_1) \tag{2.63}$$

Here p_s has been set to zero in (2.62). Inserting p_{s_1} in (2.62) and then in (2.59) we arrive at

$$\begin{aligned} p_{s_2}(\vec{r}_2, t) &= G_i F_{op}\left[p_i(\vec{r}_1, t_1) + G_i F_{op}\, p_i(\vec{r}_1, t_1)\right] \\ &= G_i F_{op}\, p_i(\vec{r}_1, t_1) + \left[G_i F_{op}\right]^2 p_i(\vec{r}_1, t_1) \end{aligned} \tag{2.64}$$

It is emphasized here that G_i indicates an integral over $\vec{r}_1$ and t_1, and not the pressure at point $\vec{r}_1$ and time t_1 but over the volume of V' and time T indicated by $\vec{r}_1$ and t_1.

The general expression for the scattered field then is:

$$\begin{aligned} p_s(\vec{r}_2, t) = \quad & G_i F_{op}\, p_i(\vec{r}_1, t_1) \quad + \\ & \left[G_i F_{op}\right]^2 p_i(\vec{r}_1, t_1) \quad + \\ & \left[G_i F_{op}\right]^3 p_i(\vec{r}_1, t_1) \quad + \\ & \left[G_i F_{op}\right]^4 p_i(\vec{r}_1, t_1) \quad + \cdots \end{aligned} \tag{2.65}$$

Terms involving $\left[G_i F_{op}\right]^N p_i(\vec{r}_1, t_1)$, where $N > 1$, describe multiple scattering of order N. Usually the scattering from small obstacles is considered weak so higher order terms can be neglected. Thus, a useful approximation is to employ only the first term in the expansion. This corresponds to the first order Born-approximation.

Using this (2.59) can be approximated by (note the replacement of $p_1(\vec{r}_1, t_1)$ with $p_i(\vec{r}_1, t_1)$):

$$\begin{aligned} p_s(\vec{r}_2, t) \approx \int_{V'}\int_T \Bigg[& \frac{1}{\rho_0}\nabla(\Delta\rho(\vec{r}_1)) \cdot \nabla p_i(\vec{r}_1, t_1) \\ & - \frac{2\Delta c(\vec{r}_1)}{c_0^3}\frac{\partial^2 p_i(\vec{r}_1, t_1)}{\partial t^2}\Bigg] \quad G(\vec{r}_1, t_1 \mid \vec{r}_2, t) dt_1\, d^3\vec{r}_1 \end{aligned} \tag{2.66}$$

So in order to calculate the scattered field, the incident field for the homogeneous medium must be calculated.

2.6.3 Calculation of the incident field

The incident field is generated by the ultrasound transducer assuming no other sources exist in the tissue. The field is conveniently calculated by employing the velocity potential $\psi(\vec{r}, t)$, and enforcing appropriate boundary conditions [31], [32]. The velocity potential satisfies the following wave equation for the homogeneous medium:

$$\nabla^2\psi - \frac{1}{{c_0}^2}\frac{\partial^2\psi}{\partial^2 t} = 0 \tag{2.67}$$

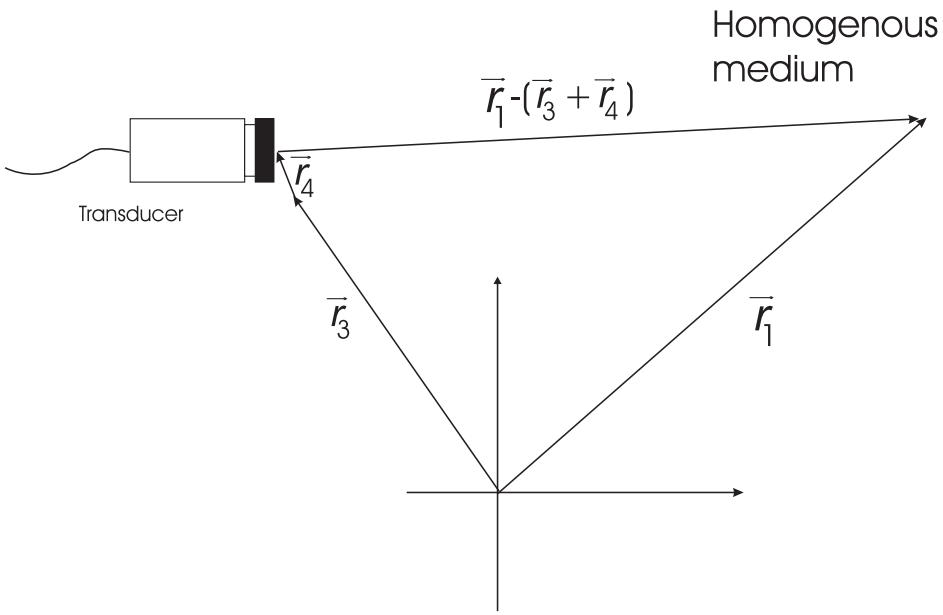

Figure 2.17: Coordinate system for calculating the incident field.

and the pressure is calculated from:

$$p(\vec{r},t) = \rho_0 \frac{\partial \psi(\vec{r},t)}{\partial t} \tag{2.68}$$

The coordinate system shown in Fig. 2.17 is used in the calculation. The particle velocity normal to the transducer surface is denoted by $v(\vec{r}_3+\vec{r}_4,t)$, where $\vec{r}_3$ identifies the position of the transducer and $\vec{r}_4$ a point on the transducer surface relative to $\vec{r}_3$.

The solution to the homogeneous wave equation is [32]:

$$\psi(\vec{r}_1+\vec{r}_3,t) = \int_S \int_T v(\vec{r}_3+\vec{r}_4,t_3) g(\vec{r}_1,t \mid \vec{r}_3+\vec{r}_4,t_3) dt_3 \, d^2\vec{r}_4 \tag{2.69}$$

when the transducer is mounted in a rigid infinite planar baffle. S denotes the transducer surface.

g is the Green's function for a bounded medium and is

$$g(\vec{r}_1,t \mid \vec{r}_3+\vec{r}_4,t_3) = \frac{\delta(t-t_3-\frac{|\vec{r}_1-\vec{r}_3-\vec{r}_4|}{c_0})}{2\pi \mid \vec{r}_1-\vec{r}_3-\vec{r}_4 \mid} \tag{2.70}$$

$\mid \vec{r}_1-\vec{r}_3-\vec{r}_4 \mid$ is the distance from S to the point where the field is calculated and c_0 the mean propagation velocity. The field is calculated under the assumption of radiation into an isotropic, homogeneous, non-dissipative medium.

If a slightly curved transducer is used, an additional term is introduced as shown in Morse & Feshbach [33]. This term is called the second order diffraction term in Penttinen & Luukkala [18]. It can be shown to vanish for a planar transducer, and as long as the transducer is only slightly curved and large compared to the wavelength of the ultrasound, the resulting expression is a good approximation to the pressure field [18].

If the particle velocity is assumed to be uniform over the surface of the transducer, (2.69) can be reduced to [34]:

$$\psi(\vec{r}_1,\vec{r}_3,t) = \int_T v(t_3) \int_S g(\vec{r}_1,t \mid \vec{r}_3+\vec{r}_4,t_3) d^2\vec{r}_4 \, dt_3 \tag{2.71}$$

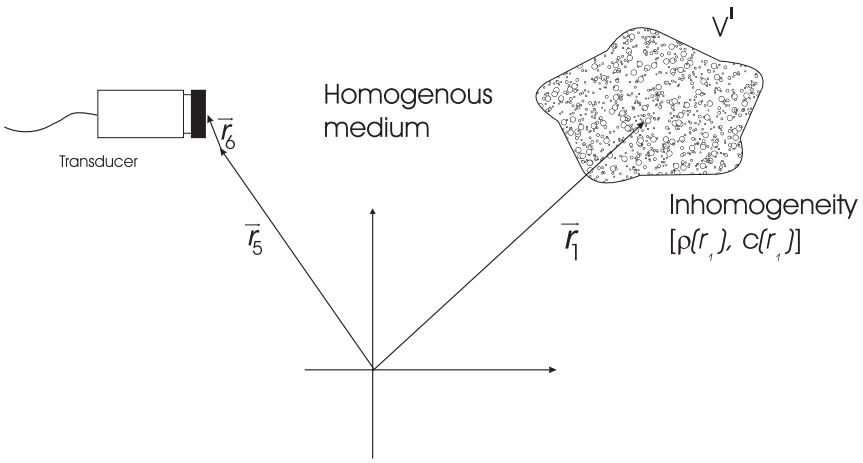

Figure 2.18: Coordinate system for calculating the received signal.

This is the spatial impulse response previously derived, and the sound pressure for the incident field then is:

$$p(\vec{r}_1, \vec{r}_3, t) = \rho_0 \frac{\partial \psi(\vec{r}_1, \vec{r}_3, t)}{\partial t} = \rho_0 v(t) \underset{t}{\star} \frac{\partial h(\vec{r}_1, \vec{r}_3, t)}{\partial t} \tag{2.72}$$

or

$$p(\vec{r}_1, \vec{r}_3, t) = \rho_0 \frac{\partial v(t)}{\partial t} \underset{t}{\star} h(\vec{r}_1, \vec{r}_3, t) \tag{2.73}$$

2.6.4 Calculation of the received signal

The received signal is the scattered pressure field integrated over the transducer surface, convolved with the electro-mechanical impulse response, $E_m(t)$, of the transducer. To calculate this we introduce the coordinate system shown in Fig. 2.18. $\vec{r}_6 + \vec{r}_5$ indicates a receiving element on the surface of the transducer that is located at $\vec{r}_5$. The received signal is:

$$p_r(\vec{r}_5, t) = E_m(t) \underset{t}{\star} \int_S p_s(\vec{r}_6 + \vec{r}_5, t) d^2\vec{r}_6 \tag{2.74}$$

The scattered field is:

$$p_s(\vec{r}_6 + \vec{r}_5, t) = \tfrac{1}{2} \int_{V'} \int_T F_{op}\left[p_i(\vec{r}_1, t_1)\right] \frac{\delta(t - t_1 - \frac{|\vec{r}_6 + \vec{r}_5 - \vec{r}_1|}{c_0})}{2\pi \mid \vec{r}_6 + \vec{r}_5 - \vec{r}_1 \mid} dt_1 \, d^3\vec{r}_1 \tag{2.75}$$

Combining this with (2.74) and comparing with (2.9) we see that p_r includes Green's function for bounded space integrated over the transducer surface, which is equal to the spatial impulse response. Inserting the expression for p_i and performing the integration over the transducer surface and over time, results in:

$$p_r(\vec{r}_5, t) = E_m(t) \underset{t}{\star} \tfrac{1}{2} \int_{V'} F_{op}\left[\rho_0 \frac{\partial v(t)}{\partial t} \underset{t}{\star} h(\vec{r}_1, \vec{r}_3, t)\right] \underset{t}{\star} h(\vec{r}_5, \vec{r}_1, t) d^3\vec{r}_1 \tag{2.76}$$

If the position of the transmitting and the receiving transducer is the same ($\vec{r}_3 = \vec{r}_5$), then a simple rearrangement of (2.76) yields:

$$p_r(\vec{r}_5, t) = \frac{\rho_0}{2} E_m(t) \underset{t}{\star} \frac{\partial v(t)}{\partial t} \underset{t}{\star} \int_{V'} F_{op}\left[h_{pe}(\vec{r}_1, \vec{r}_5, t)\right] d^3\vec{r}_1 \tag{2.77}$$

where

$$h_{pe}(\vec{r}_1, \vec{r}_5, t) = h(\vec{r}_1, \vec{r}_5, t) \underset{t}{\star} h(\vec{r}_5, \vec{r}_1, t) \tag{2.78}$$

is the pulse-echo spatial impulse response.

The calculated signal is the response measured for one given position of the transducer. For a B-mode scan picture a number of scan-lines is measured and combined to a picture. To analyze this situation, the last factor in (2.77) is explicitly written out

$$\int_{V'} \left[\frac{1}{\rho_0} \nabla(\Delta\rho(\vec{r}_1)) \cdot \nabla h_{pe}(\vec{r}_1, \vec{r}_5, t) - \frac{2\Delta c(\vec{r}_1)}{c_0^3} \frac{\partial^2 h_{pe}(\vec{r}_1, \vec{r}_5, t)}{\partial t^2} \right] d^3\vec{r}_1 \tag{2.79}$$

From section 2.6.3 it is know that H_{pe} is a function of the distance between $\vec{r}_1$ and $\vec{r}_5$, while $\Delta\rho$ and Δc only are functions of $\vec{r}_1$. So when $\vec{r}_5$ is varied over the volume of interest, the resulting image is a spatial non-stationary convolution between $\Delta\rho$, Δc and a modified form of the pulse-echo spatial impulse response.

If we assume that the pulse-echo spatial impulse is slowly varying so that the spatial frequency content is constant over a finite volume, then (2.79) can be rewritten

$$\int_{V'} \left[\frac{1}{\rho_0} \Delta\rho(\vec{r}_1) \nabla^2 h_{pe}(\vec{r}_1, \vec{r}_5, t) - \frac{2\Delta c(\vec{r}_1)}{c_0^3} \frac{\partial^2 h_{pe}(\vec{r}_1, \vec{r}_5, t)}{\partial t^2} \right] d^3\vec{r}_1 \tag{2.80}$$

h_{pe} is a function of the distance between the transducer and the scatterer or equivalently of the corresponding time given by

$$t = \frac{| \vec{r}_1 - \vec{r}_5 |}{c_0} \tag{2.81}$$

The Laplace operator is the second derivative w.r.t. the distance, which can be approximated with the second derivative w.r.t. time. So

$$\nabla^2 h_{pe}(\vec{r}_1, \vec{r}_5, t) = \frac{1}{c_0^2} \frac{\partial^2 h_{pe}(\vec{r}_1, \vec{r}_5, t)}{\partial t^2} \tag{2.82}$$

assuming only small deviations from the mean propagation velocity.

Using these approximations, (2.77) can be rewritten:

$$p_r(\vec{r}_5, t) = \frac{\rho_0}{2c_0^2} E_m(t) \underset{t}{\star} \frac{\partial v^3(t)}{\partial t^3} \underset{t}{\star} \int_{V'} \left[\frac{\Delta\rho(\vec{r}_1)}{\rho_0} - \frac{2\Delta c(\vec{r}_1)}{c_0} \right] h_{pe}(\vec{r}_1, \vec{r}_5, t) d^3\vec{r}_1 \tag{2.83}$$

Symbolically this is written

$$p_r(\vec{r}_5, t) = v_{pe}(t) \underset{t}{\star} f_m(\vec{r}_1) \underset{r}{\star} h_{pe}(\vec{r}_1, \vec{r}_5, t) \tag{2.84}$$

$\underset{r}{\star}$ denotes spatial convolution. v_{pe} is the pulse-echo wavelet which includes the transducer excitation and the electro-mechanical impulse response during emission and reception of the pulse. f_m accounts for the inhomogeneities in the tissue due to density and propagation velocity perturbations which give rise to the scattered signal. h_{pe} is the modified pulse-echo spatial impulse response that relates the transducer geometry to the spatial extent of the scattered field. Explicitly written out these terms are:

$$v_{pe}(t) = \frac{\rho_0}{2c_0^2} E_m(t) \underset{t}{\star} \frac{\partial v^3(t)}{\partial t^3} \tag{2.85}$$

$$f_m(\vec{r}_1) = \frac{\Delta\rho(\vec{r}_1)}{\rho_0} - \frac{2\Delta c(\vec{r}_1)}{c_0} \tag{2.86}$$

$$h_{pe}(\vec{r}_1, \vec{r}_5, t) = h(\vec{r}_1, \vec{r}_5, t) \underset{t}{\star} h(\vec{r}_5, \vec{r}_1, t) \tag{2.87}$$

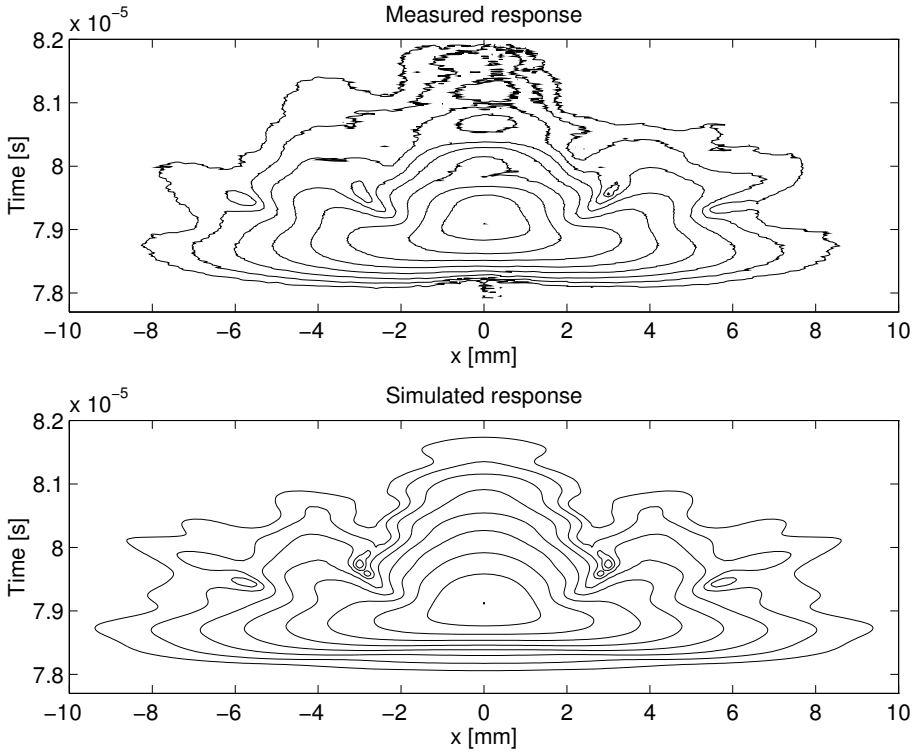

Figure 2.19: Measured and simulated pulse-echo response for a concave transducer. The axial distance was 60 mm and the small scatterer was moved in the lateral direction. The envelope of the RF signal is shown as 6 dB contours.

Expression (2.84) consists of three distinct terms. The interesting signal, and the one that should be displayed in medical ultrasound, is $f_m(\vec{r}_1)$. We, however, measure a time and spatially smoothed version of this, which obscures the finer details in the picture. The smoothing consists of a convolution in time with a fixed wavelet $v_{pe}(t)$ and a spatial convolution with a spatially varying $h_{pe}(\vec{r}_1, \vec{r}_5, t)$.

2.6.5 Example of pulse echo response

To show that the pulse-echo response can be calculated to good accuracy, a single example is shown in Fig. 2.19 for a concave transducer (r = 8.1 mm) with a focus at R = 150 mm. The measured and simulated responses were obtained at a distance of 60 mm from the transducer surface. The measured pressure field was acquired by moving a needle pointing toward the transducer in steps of 0.2 mm in the lateral direction, making measurements in a plane containing the acoustical axis of the transducer. The simulated field was calculated by measuring v_{pe} as the response from a planar reflector, and then using (2.32) and (2.84) to calculate the field. The envelope of the RF-signals is shown as a contour plot with 6 dB between the contours. The plots span 20 mm in the lateral direction and 4 μs in the axial direction.

2.6.6 Attenuation effects

The model includes attenuation of the pulse due to propagation, but not the dispersive attenuation of the wave observed when propagating in tissue. This changes the pulse continuously as it propagates down through the tissue. Not including dispersive attenuation is, however, not a serious drawback of the theory, as this change of the pulse can be lumped into the already spatially varying h_{pe}. Or, if in the far field and assuming a homogeneous, dispersive

attenuation, then an attenuation transfer function can be convolved onto v_{pe} to yield an attenuated pulse.

Submerging the transducer into a *homogeneously* attenuating medium will modify the propagation of the spherical waves, which will change continuously as a function of distance from the transducer. The spatial impulse is then changed to

$$h_{att}(t,\vec{r}) = \int_T \int_S a(t-\tau, |\vec{r}+\vec{r}_1|) \frac{\delta(\tau - \frac{|\vec{r}+\vec{r}_1|}{c})}{|\vec{r}+\vec{r}_1|} dS d\tau \tag{2.88}$$

when linear propagation is assumed and the attenuation is the same throughout the medium. a is the attenuation impulse response. The spherical wave is convolved with the distance dependent attenuation impulse response and spherical waves emanating from different parts of the aperture are convolved with different attenuation impulse responses.

A model for the attenuation must be introduced in order to solve the integral. Ultrasound propagating in tissue experiences a nearly linear with frequency attenuation and a commonly used attenuation amplitude transfer function is

$$|A'(f,|\vec{r}|)| = \exp(-\beta' f |\vec{r}|) \tag{2.89}$$

where β' is attenuation in nepers per meter. We here prefer to split the attenuation into a frequency dependent and a frequency independent part term as

$$|A(f,|\vec{r}|)| = \exp(-\alpha|\vec{r}|)\exp(-\beta(f-f_0)|\vec{r}|) \tag{2.90}$$

α is the frequency independent attenuation coefficient, and f_0 the transducer center frequency. The phase of the attenuation need also be considered. Kak and Dines [35] introduced a linear with frequency phase response

$$\Theta(f) = 2\pi f \tau_b |\vec{r}| \tag{2.91}$$

where τ_b is the bulk propagation delay per unit length and is equal to $1/c$. This, however, results in an attenuation impulse response that is non-causal. Gurumurthy and Arthur [36] therefore suggested using a minimum phase impulse response, where the amplitude and phase spectrum form a Hilbert transform pair. The attenuation spectrum is then given by

$$\begin{aligned} A(f,|\vec{r}|) &= \exp(-\alpha|\vec{r}|)\exp(-\beta(f-f_0)|\vec{r}|) \\ &\times \exp(-j2\pi f(\tau_b + \tau_m \frac{\beta}{\pi^2})|\vec{r}|) \\ &\times \exp(j\frac{2f}{\pi}\beta|\vec{r}|\ln(2\pi f)) \end{aligned} \tag{2.92}$$

where τ_m is the minimum phase delay factor. Gurumurthy and Arthur [36] suggest a τ_m value of 20 in order to fit the dispersion found in tissue.

The inverse Fourier transform of (2.92) must be inserted into (2.88) and the integral has to be solved for the particular transducer geometry. This is clearly a difficult, if not impossible, task and some approximations must be introduced. All spherical waves arrive at nearly the same time instance, if the distance to the field point is much larger than the transducer aperture. In this case the attenuation function is, thus, the same for all waves and the result is a convolution between the attenuation impulse response and the spatial impulse response, which is a Dirac impulse. A spatial impulse response other than a Dirac function indicates that the spherical waves arrive at different times. Multiplying the arrival time with the propagation velocity gives the distance to the points on the aperture contributing to the response at that time instance. A first approximation is, therefore, to multiply the non-attenuated spatial impulse response with the proper frequency independent term. This approximation also assumes that the span of values for $|\vec{r}+\vec{r_1}|$ is so small that both $1/|\vec{r}+\vec{r}_1|$ and the attenuation can be assumed to be roughly constant.

The frequency dependent function will also change for the different values of the spatial impulse response. A non-stationary convolution must, thus, be performed. One possible method to avoid this is to assume that the frequency dependent attenuation impulse response is constant for the time and, thus, distances $|\vec{r}+\vec{r}_1|$ where h is non-zero. The mean distance is then used in (2.92) and the inverse Fourier transform of $A(f,|\vec{r}_{mid}|)$ is convolved with $h(t,\vec{r})$. The accuracy of the approach depends on the duration of h and of the attenuation. The error in dB for a concave transducer

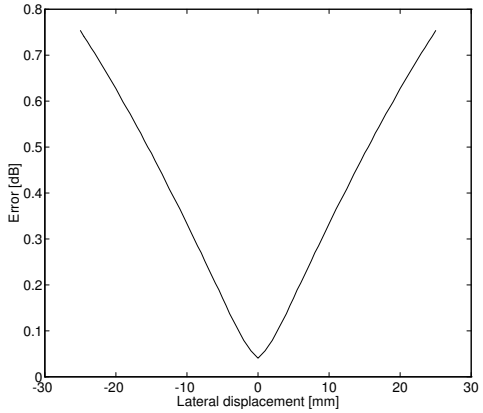

Figure 2.20: Error of assuming a non-varying frequency dependent attenuation over the duration of the spatial impulse response.

with a radius of 10 mm focused at 100 mm and an attenuation of 0.5 dB/[MHz cm] is shown in Fig. 2.20. The axial distance to the transducer is 50 mm.

An example of the influence of attenuation on the point spread function (PSF) is shown in Fig. 2.21. A concave transducer with a radius of 8 mm, center frequency of 3 MHz, and focused at 100 mm was used. Fig. 2.21 shows point spread functions calculated under different conditions. The logarithmic envelope of the received pressure is displayed as a function of time and lateral displacement. The left most graph shows the normalized PSF for the transducer submerged in a non-attenuating medium. The distance to the field point is 60 mm and the function is shown for lateral displacements from -8 to 8 mm. Introducing a 0.5 dB/[MHz cm] attenuation yields the normalized PSF shown in the middle. The central core of the PSF does not change significantly, but the shape at -30 dB and below are somewhat different from the non-attenuated response. A slightly broader and longer function is seen, but the overall shape is the same.

An commonly used approach to characterize the field is to include the attenuation into the basic one-dimensional pulse, and then use the non-attenuated spatial impulse response in calculating the PSF. This is the approach used in the rightmost graph in Fig. 2.21. All attenuation is included in the pulse and the spatial impulse response calculated in the leftmost graph is used for making the PSF. The similarity to the center graph is striking. Apart from a slightly longer response, nearly all features of the field are the same. It is, thus, appropriate to estimate the attenuated one-dimensional pulse and reconstruct the whole field from this and knowledge of the transducer geometry.

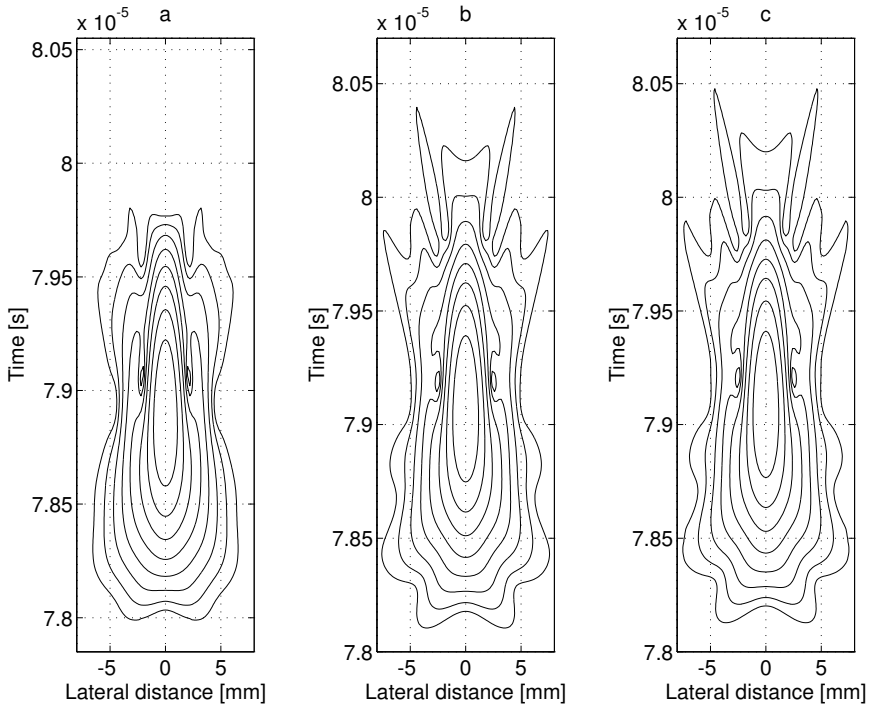

Figure 2.21: Contour plots of point spread functions for different media and calculation methods. a: Non attenuating medium. b: 0.5 dB/[MHz cm] attenuation. c: 0.5 dB/[MHz cm] attenuation on the one-dimensional pulse. There is 6 dB between the contour lines. The distance to the transducer is 60 mm.

CHAPTER

THREE

Ultrasound imaging

Modern medical ultrasound scanners are used for imaging nearly all soft tissue structures in the body. The anatomy can be studied from gray-scale B-mode images, where the reflectivity and scattering strength of the tissues are displayed. The imaging is performed in real time with 20 to 100 images per second. The technique is widely used since it does not use ionizing radiation and is safe and painless for the patient.

This chapter gives a short introduction to modern ultrasound imaging using array transducers. Part of the chapter is based on [9] and [37].

3.1 Fourier relation

This section derives a simple relation between the oscillation of the transducer surface and the ultrasound field. It is shown that field in the far-field can be found by a simple one-dimensional Fourier transform of the one-dimensional aperture pattern. This might seem far from the actual imaging situation in the near field using pulsed excitation, but the approach is very convenient in introducing all the major concepts like main and side lobes, grating lobes, etc. It also very clearly reveals information about the relation between aperture properties and field properties.

3.1.1 Derivation of Fourier relation

Consider a simple line source as shown in Fig. 3.1 with a harmonic particle speed of $U_0 \exp(j\omega t)$. Here U_0 is the vibration amplitude and ω is its angular frequency. The line element of length dx generates an increment in pressure of [13]

$$dp = j\frac{\rho_0 ck}{4\pi r'} U_0 a_p(x) e^{j(\omega t - kr')} dx, \tag{3.1}$$

where ρ_0 is density, c is speed of sound, $k = \omega/c$ is the wavenumber, and $a_p(x)$ is an amplitude scaling of the individual parts of the aperture. In the far-field ($r \ll L$) the distance from the radiator to the field points is (see Fig. 3.1)

$$r' = r - x\sin\theta \tag{3.2}$$

The emitted pressure is found by integrating over all the small elements of the aperture

$$p(r,\theta,t) = j\frac{\rho_0 cU_0 k}{4\pi}\int_{-\infty}^{+\infty} a_p(x)\frac{e^{j(\omega t - r')}}{r'}dx. \tag{3.3}$$

Notice that $a_p(x) = 0$ if $|x| > L/2$. Here r' can be replaced with r, if the extent of the array is small compared to the distance to the field point ($r \ll L$). Using this approximation and inserting (3.2) in (3.3) gives

$$p(r,\theta,t) = j\frac{\rho_0 cU_0 k}{4\pi r}\int_{-\infty}^{+\infty} a_p(x)e^{j(\omega t - kr + kx\sin\theta)}dx = \frac{\rho_0 cU_0 k}{4\pi r}e^{j(\omega t - kr)}\int_{-\infty}^{+\infty} a_p(x)e^{jkx\sin\theta}dx, \tag{3.4}$$

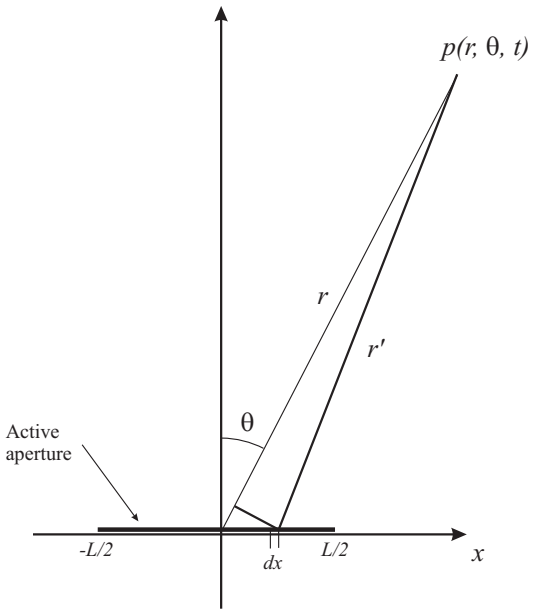

Figure 3.1: Geometry for line aperture.

since ωt and kr are independent of x. Hereby the pressure amplitude of the field for a given frequency can be split into two factors:

$$\begin{aligned} P_{ax}(r) &= \frac{\rho_0 c U_0 k L}{4\pi r} \\ H(\theta) &= \frac{1}{L}\int_{-\infty}^{+\infty} a_p(x) e^{jkx\sin\theta} dx \\ P(r,\theta) &= P_{ax}(r) H(\theta) \end{aligned} \tag{3.5}$$

The first factor $P_{ax}(r)$ characterizes how the field drops off in the axial direction as a factor of distance, and $H(\theta)$ gives the variation of the field as a function of angle. The first term drops off with $1/r$ as for a simple point source and $H(\theta)$ is found from the aperture function $a_p(x)$. A slight rearrangement gives[1]

$$H(\theta) = \frac{1}{L}\int_{-\infty}^{+\infty} a_p(x) e^{j2\pi x f \frac{\sin\theta}{c}} dx = \frac{1}{L}\int_{-\infty}^{+\infty} a_p(x) e^{j2\pi x f'} dx. \tag{3.6}$$

This very closely resembles the standard Fourier integral given by

$$\begin{aligned} G(f) &= \int_{-\infty}^{+\infty} g(t) e^{-j2\pi t f} dt \\ g(t) &= \int_{-\infty}^{+\infty} G(f) e^{j2\pi t f} df \end{aligned} \tag{3.7}$$

There is, thus, a Fourier relation between the radial beam pattern and the aperture function, and the normal Fourier relations can be used for understanding the beam patterns for typical apertures.

[1] The term $1/L$ is included to make $H(\theta)$ a unit less number.

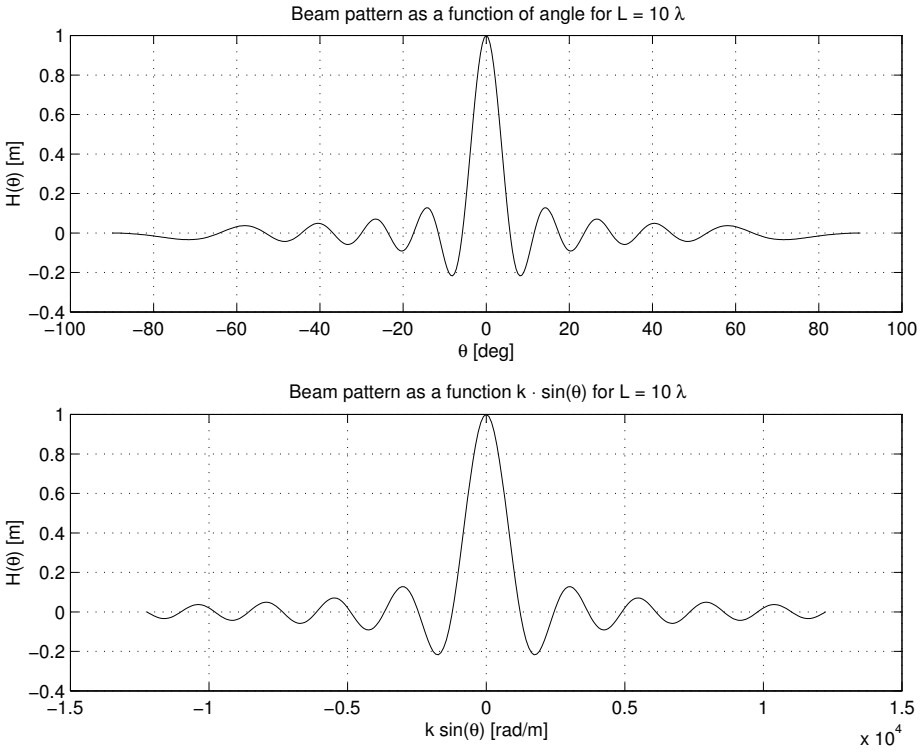

Figure 3.2: Angular beam pattern for a line aperture with a uniform aperture function as a function of angle (top) and as a function of $k\sin(\theta)$ (bottom).

3.1.2 Beam patterns

The first example is for a simple line source, where the aperture function is constant such that

$$a_p(x) = \begin{cases} 1 & |x| \leq L/2 \\ 0 & \text{else} \end{cases} \tag{3.8}$$

The angular factor is then

$$H(\theta) = \frac{\sin(\pi L f \frac{\sin\theta}{c})}{\pi L f \frac{\sin\theta}{c}} = \frac{\sin(\frac{k}{2} L \sin\theta)}{\frac{k}{2} L \sin\theta} \tag{3.9}$$

A plot of the sinc function is shown in Fig. 3.2. A single main lobe can be seen with a number of side lobe peaks. The peaks fall off proportionally to k or f. The angle of the first zero in the function is found at

$$\sin\theta = \frac{c}{Lf} = \frac{\lambda}{L}. \tag{3.10}$$

The angle is, thus, dependent on the frequency and the size of the array. A large array or a high emitted frequency, therefore, gives a narrow main lobe.

The magnitude of the first sidelobe relative to the mainlobe is given by

$$\frac{H(\arcsin(\frac{3c}{2Lf}))}{H(0)} = L\frac{\sin(3\pi/2)}{3\pi/2}/L = \frac{2}{3\pi} \tag{3.11}$$

The relative sidelobe level is, thus, independent of the size of the array and of the frequency, and is solely determined by the aperture function $a_p(x)$ through the Fourier relation. The large discontinuities of $a_p(x)$, thus, give rise to the

high side lobe level, and they can be reduced by selecting an aperture function that is smoother like a Hanning window or a Gaussian shape.

Modern ultrasound transducers consist of a number of elements each radiating ultrasound energy. Neglecting the phasing of the element (see Section 3.2) due to the far-field assumption, the aperture function can be described by

$$a_p(x) = a_{ps}(x) * \sum_{n=-N/2}^{N/2} \delta(x - d_x n), \tag{3.12}$$

where $a_{ps}(x)$ is the aperture function for the individual elements, d_x is the spacing (pitch) between the centers of the individual elements, and N is the number of elements in the array. Using the Fourier relationship the angular beam pattern can be described by

$$H_p(\theta) = H_{ps}(\theta) H_{per}(\theta), \tag{3.13}$$

where

$$\sum_{n=-N/2}^{N/2} \delta(x - d_x n) \leftrightarrow H_{per}(\theta) = \sum_{n=-N/2}^{N/2} e^{-jnd_x ksin\theta}. = \sum_{n=-N/2}^{N/2} e^{-j2\pi \frac{fsin\theta}{c} nd_x}. \tag{3.14}$$

Summing the geometric series gives

$$H_{per}(\theta) = \frac{\sin\left((N+1)\frac{k}{2} d_x \sin\theta\right)}{\sin\left(\frac{k}{2} d_x \sin\theta\right)} \tag{3.15}$$

is the Fourier transform of series of delta functions. This function repeats itself with a period that is a multiple of

$$\begin{aligned} \pi &= \frac{k}{2} d_x \sin\theta \\ \sin\theta &= \frac{\pi}{k d_x} = \frac{\lambda}{d_x}. \end{aligned} \tag{3.16}$$

This repetitive function gives rise to the grating lobes in the field. An example is shown in Fig. 3.3.

The grating lobes are due to the periodic nature of the array, and corresponds to sampling of a continuous time signal. The grating lobes will be outside a ± 90 deg. imaging area if

$$\begin{aligned} \frac{\lambda}{d_x} &= 1 \\ d_x &= \lambda \end{aligned} \tag{3.17}$$

Often the beam is steered in a direction and in order to ensure that grating lobes do not appear in the image, the spacing or pitch of the elements is selected to be $d_x = \lambda/2$. This also includes ample margin for the modern transducers that often have a very broad bandwidth.

An array beam can be steered in a direction by applying a time delay on the individual elements. The difference in arrival time for a given direction θ_0 is

$$\tau = \frac{d_x \sin\theta_0}{c} \tag{3.18}$$

Steering in a direction θ_0 can, therefore, be accomplished by using

$$\sin\theta_0 = \frac{c\tau}{d_x} \tag{3.19}$$

where τ is the delay to apply to the signal on the element closest to the center of the array. A delay of 2τ is then applied on the second element and so forth. The beam pattern for the grating lobe is then replaced by

$$H_{per}(\theta) = \frac{\sin\left((N+1)\frac{k}{2} d_x \sin\left(\theta - \frac{c\tau}{d_x}\right)\right)}{\sin\left(\frac{k}{2} d_x \sin\left(\theta - \frac{c\tau}{d_x}\right)\right)}. \tag{3.20}$$

Notice that the delay is independent of frequency, since it is essentially only determined by the speed of sound.

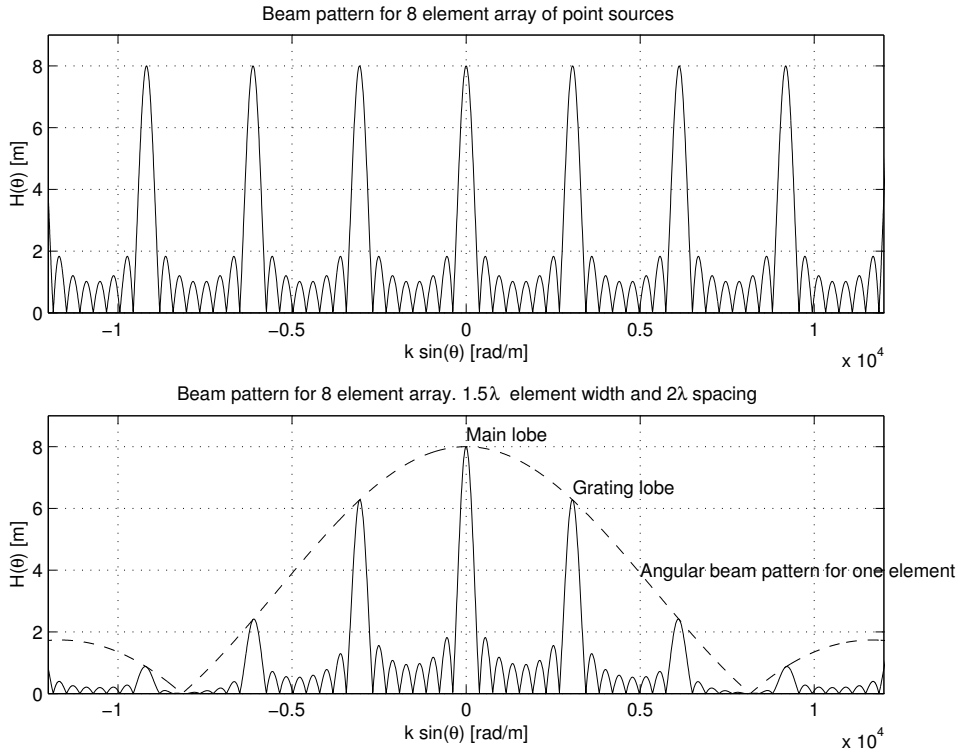

Figure 3.3: Grating lobes for array transducer consisting of 8 point elements (top) and of 8 elements with a size of 1.5λ (bottom). The pitch (or distance between the elements) is 2λ.

3.2 Focusing

The essence of focusing an ultrasound beam is to align the pressure fields from all parts of the aperture to arrive at the field point at the same time. This can be done through a physically curved aperture, through a lens in front of the aperture, or by the use of electronic delays for multi-element arrays. All seek to align the arrival of the waves at a given point through delaying or advancing the fields from the individual elements. The delay (positive or negative) is determined using ray acoustics. The path length from the aperture to the point gives the propagation time and this is adjusted relative to some reference point. The propagation from the center of the aperture element to the field point is

$$t_i = \frac{1}{c}\sqrt{(x_i - x_f)^2 + (y_i - y_f)^2 + (z_i - z_f)^2} \tag{3.21}$$

where (x_f, y_f, z_f) is the position of the focal point, (x_i, y_i, z_i) is the center for the physical element number i, c is the speed of sound, and t_i is the calculated propagation time.

A point is selected on the whole aperture as a reference for the imaging process. The propagation time for this is

$$t_c = \frac{1}{c}\sqrt{(x_c - x_f)^2 + (y_c - y_f)^2 + (z_c - z_f)^2} \tag{3.22}$$

where (x_c, y_c, z_c) is the reference center point on the aperture. The delay to use on each element of the array is then

$$\Delta t_i = \frac{1}{c}\left(\sqrt{(x_c - x_f)^2 + (y_c - y_f)^2 + (z_c - z_f)^2} - \sqrt{(x_i - x_f)^2 + (y_i - y_f)^2 + (z_i - z_f)^2}\right) \tag{3.23}$$

Notice that there is no limit on the selection of the different points, and the beam can, thus, be steered in a preferred direction.

The arguments here have been given for emission from an array, but they are equally valid during reception of the ultrasound waves due to acoustic reciprocity. At reception it is also possible to change the focus as a function of time and thereby obtain a dynamic tracking focus. This is used by all modern ultrasound scanners, Beamformers based on analog technology makes it possible to create several receive foci and the newer digital scanners change the focusing continuously for every depth in receive. A single focus is only possible in transmit and composite imaging is therefore often used in modern imaging. Here several pulse emissions with focusing at different depths in the same direction are used and the received signals are combined to form one image focused in both transmit and receive at different depths (composit imaging).

The focusing can, thus, be defined through time lines as:

From time	Focus at
0	x_1, y_1, z_1
t_1	x_1, y_1, z_1
t_2	x_2, y_2, z_2
$\vdots$	$\vdots$

For each focal zone there is an associated focal point and the time from which this focus is used. The arrival time from the field point to the physical transducer element is used for deciding which focus is used. Another possibility is to set the focusing to be dynamic, so that the focus is changed as a function of time and thereby depth. The focusing is then set as a direction defined by two angles and a starting point on the aperture.

Section 3.1 showed that the side and grating lobes of the array can be reduced by employing apodization of the elements. Again a fixed function can be used in transmit and a dynamic function in receive defined by

From time	Apodize with
0	$a_{1,1}, a_{1,2}, \cdots a_{1,N_e}$
t_1	$a_{1,1}, a_{1,2}, \cdots a_{1,N_e}$
t_2	$a_{2,1}, a_{2,2}, \cdots a_{2,N_e}$
t_3	$a_{3,1}, a_{3,2}, \cdots a_{3,N_e}$
$\vdots$	$\vdots$

Here $a_{1,1}$ is the amplitude scaling value multiplied onto element 1 after time instance t_1. Typically a Hamming or Gaussian shaped function is used for the apodization. In receive the width of the function is often increased to compensate for attenuation effects and for keeping the point spread function roughly constant. The F-number defined by

$$F = \frac{D}{L} \tag{3.24}$$

where L is the total width of the active aperture and D is the distance to the focus, is often kept constant. More of the aperture is often used for larger depths and a compensation for the attenuation is thereby partly made. An example of the use of dynamic apodization is given in Section 3.6.

3.3 Fields from array transducers

Most modern scanners use arrays for generating and receiving the ultrasound fields. These fields are quite simple to calculate, when the spatial impulse response for a single element is known. This is the approach used in the Field II program, and this section will extend the spatial impulse response to multi element transducers and will elaborate on some of the features derived for the fields in Section 3.1.

Since the ultrasound propagation is assumed to be linear, the individual spatial impulse responses can simply be added. If $h_e(\vec{r}_p, t)$ denotes the spatial impulse response for the element at position $\vec{r}_i$ and the field point $\vec{r}_p$, then the spatial impulse response for the array is

$$h_a(\vec{r}_p, t) = \sum_{i=0}^{N-1} h_e(\vec{r}_i, \vec{r}_p, t), \tag{3.25}$$

assuming all N elements to be identical.

Let us assume that the elements are very small and the field point is far away from the array, so h_e is a Dirac function. Then

$$h_a(\vec{r}_p, t) = \frac{k}{R_p} \sum_{i=0}^{N-1} \delta(t - \frac{|\vec{r}_i - \vec{r}_p|}{c}) \tag{3.26}$$

when $R_p = |\vec{r}_a - \vec{r}_p|$, k is a constant of proportionality, and $\vec{r}_a$ is the position of the array. Thus, h_a is a train of Dirac pulses. If the spacing between the elements is D, then

$$h_a(\vec{r}_p, t) = \frac{k}{R_p} \sum_{i=0}^{N-1} \delta\left(t - \frac{|\vec{r}_a + iD\vec{r}_e - \vec{r}_p|}{c}\right), \tag{3.27}$$

where $\vec{r}_e$ is a unit vector pointing in the direction along the elements. The geometry is shown in Fig. 3.4.

The difference in arrival time between elements far from the transducer is

$$\Delta t = \frac{D \sin \Theta}{c}. \tag{3.28}$$

The spatial impulse response is, thus, a series of Dirac pulses separated by Δt.

$$h_a(\vec{r}_p, t) \approx \frac{k}{R_p} \sum_{i=0}^{N-1} \delta\left(t - \frac{R_p}{c} - i\Delta t\right). \tag{3.29}$$

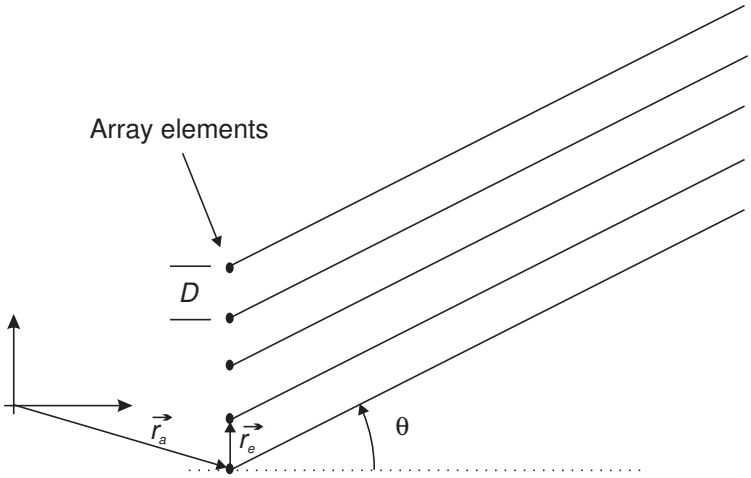

Figure 3.4: Geometry of linear array (from [9], Copyright Cambridge University Press).

The time between the Dirac pulses and the shape of the excitation determines whether signals from individual elements add or cancel out. If the separation in arrival times corresponds to exactly one or more periods of a sine wave, then they are in phase and add constructively. Thus, peaks in the response are found for

$$n\frac{1}{f} = \frac{D\sin\Theta}{c}. \tag{3.30}$$

The main lobe is found for $\Theta = 0$ and the next maximum in the response is found for

$$\Theta = \arcsin\left(\frac{c}{fD}\right) = \arcsin\left(\frac{\lambda}{D}\right). \tag{3.31}$$

For a 3 MHz array with an element spacing of 1 mm, this amounts to $\Theta = 31°$, which will be within the image plane. The received response is, thus, affected by scatterers positioned $31°$ off the image axis, and they will appear in the lines acquired as grating lobes. The first grating lobe can be moved outside the image plane, if the elements are separated by less than a wavelength. Usually, half a wavelength separation is desirable, as this gives some margin for a broad-band pulse and beam steering.

The beam pattern as a function of angle for a particular frequency can be found by Fourier transforming h_a

$$\begin{aligned} H_a(f) &= \frac{k}{R_p}\sum_{i=0}^{N-1}\exp\left(-j2\pi f\left(\frac{R_p}{c}+i\frac{D\sin\Theta}{c}\right)\right) \\ &= \exp(-j2\pi\frac{R_p}{c})\frac{k}{R_p}\sum_{i=0}^{N-1}\exp\left(-j2\pi f\frac{D\sin\Theta}{c}\right)^i \\ &= \frac{\sin(\pi f\frac{D\sin\Theta}{c}N)}{\sin(\pi f\frac{D\sin\Theta}{c})}\exp(-j\pi f(N-1)\frac{D\sin\Theta}{c})\frac{k}{R_p}\exp(-j2\pi\frac{R_p}{c}). \end{aligned} \tag{3.32}$$

The terms $\exp(-j2\pi\frac{R_p}{c})$ and $\exp(-j\pi f(N-1)\frac{D\sin\Theta}{c})$ are constant phase shifts and play no role for the amplitude of the beam profile. Thus, the amplitude of the beam profile is

$$|H_a(f)| = \left|\frac{k}{R_p}\frac{\sin(N\pi\frac{D}{\lambda}\sin\Theta)}{\sin(\pi\frac{D}{\lambda}\sin\Theta)}\right|. \tag{3.33}$$

The beam profile at 3 MHz is shown in Fig. 3.5 for a 64-element array with $D = 1$ mm.

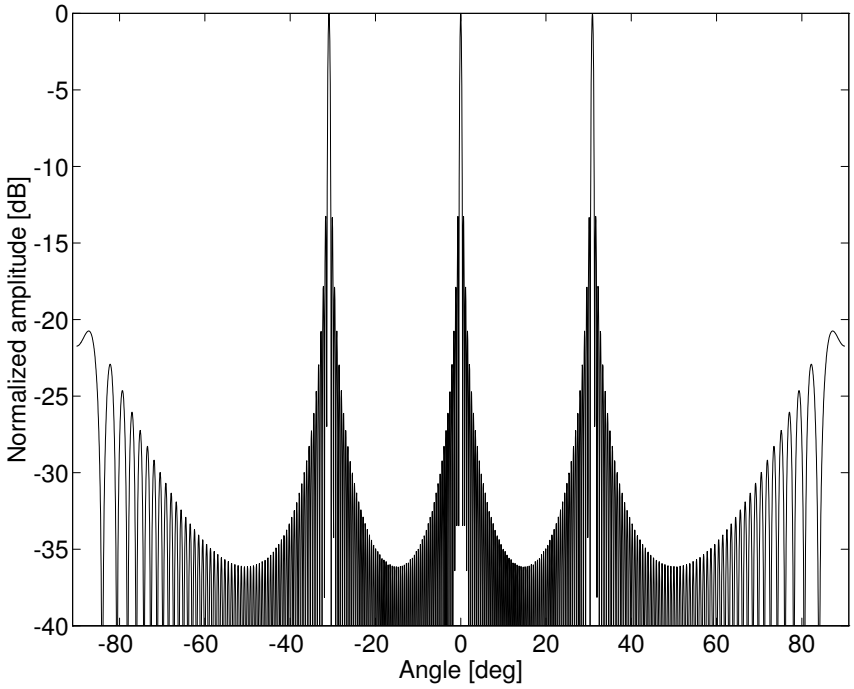

Figure 3.5: Far-field continuous wave beam profile at 3 MHz for linear array consisting of 64 point sources with an inter-element spacing of 1 mm (from [9], Copyright Cambridge University Press).

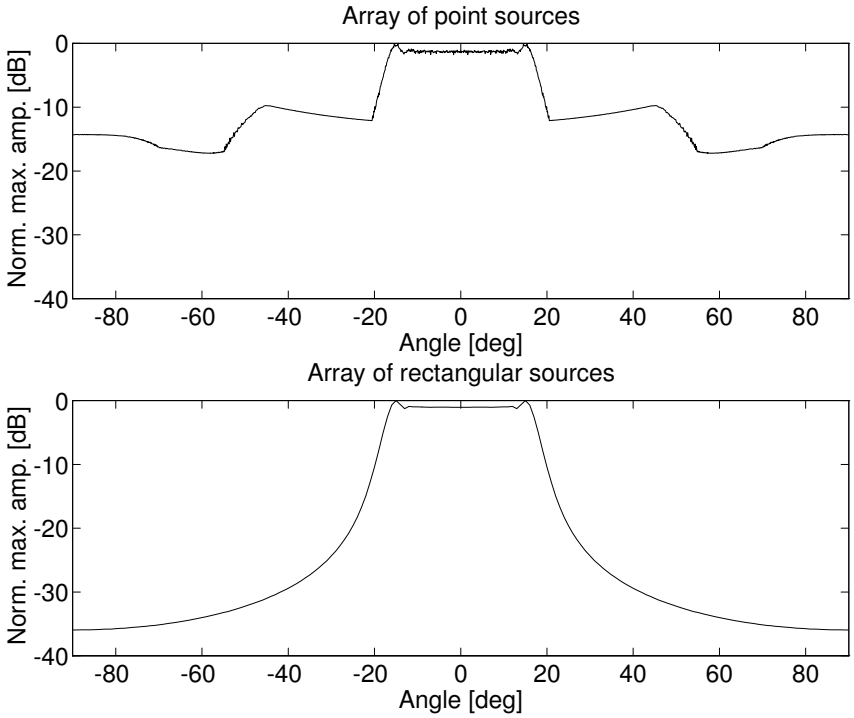

Figure 3.6: Beam profiles for an array consisting of point sources (top) or rectangular elements (bottom). The excitation pulse has a frequency of 3 MHz and the element spacing is 1 mm. The distance to the field point is 100 mm (from [9], Copyright Cambridge University Press).

Several factors change the beam profile for real, pulsed arrays compared with the analysis given here. First, the elements are not points, but rather are rectangular elements with an off-axis spatial impulse response markedly different from a Dirac pulse. Therefore, the spatial impulse responses of the individual elements will overlap and exact cancellation or addition will not take place. Second, the excitation pulse is broad band, which again influences the sidelobes. Examples of simulated responses are shown in Fig. 3.6.

The top graph shows an array of 64 point sources excited with a Gaussian 3 MHz pulse with $B_r = 0.2$. The space between the elements is 1 mm. The maximum of the response at a radial position of 100 mm from the transducer is taken. The bottom graph shows the response when rectangular elements of 1×6 mm are used. This demonstrates the somewhat crude approximation of using the far-field point source CW response to characterize arrays.

Fig. 3.7 shows the different point spread functions encountered when a phased array is used to scan over a 15 cm depth. The array consists of 128 elements each 0.2×5 mm in size, and the kerf between the elements is 0.05 mm. The transmit focus is at 70 mm, and the foci are at 30, 70, and 110 mm during reception. Quite complicated point spread functions are encountered, and they vary substantially with depth in tissue. Notice especially the edge waves, which dominate the response close to the transducer. The edge effect can be reduced by weighting responses from different elements. This is also called apodization. The excitation pulses to elements at the transducer edge are reduced, and this diminishes the edge waves. More examples are shown below in Section 3.6.

3.4 Imaging with arrays

Basically there are three different kinds of images acquired by multi-element array transducers, *i.e.* linear, convex, and phased as shown in Figures 3.8, 3.10, and 3.11. The linear array transducer is shown in Fig. 3.8. It selects the region of

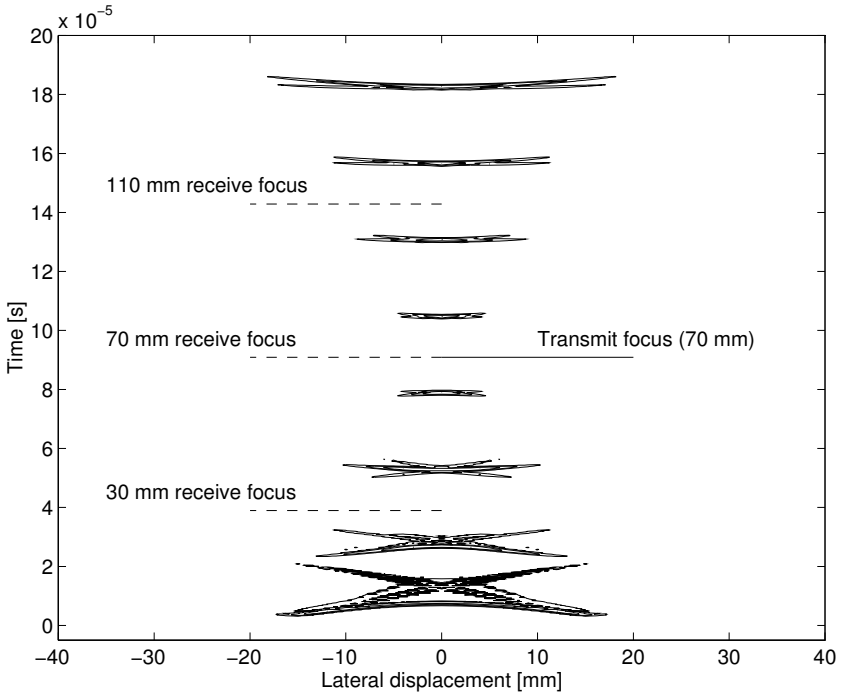

Figure 3.7: Point spread functions for different positions in a B-mode image. Onehundredtwentyeight 0.2 $\times$ 5 mm elements are used for generating and receiving the pulsed field. Three different receive foci are used. The contours shown are from 0 to -24 dB in steps of 6 dB relative to the maximum at the particular field point (from [9], Copyright Cambridge University Press).

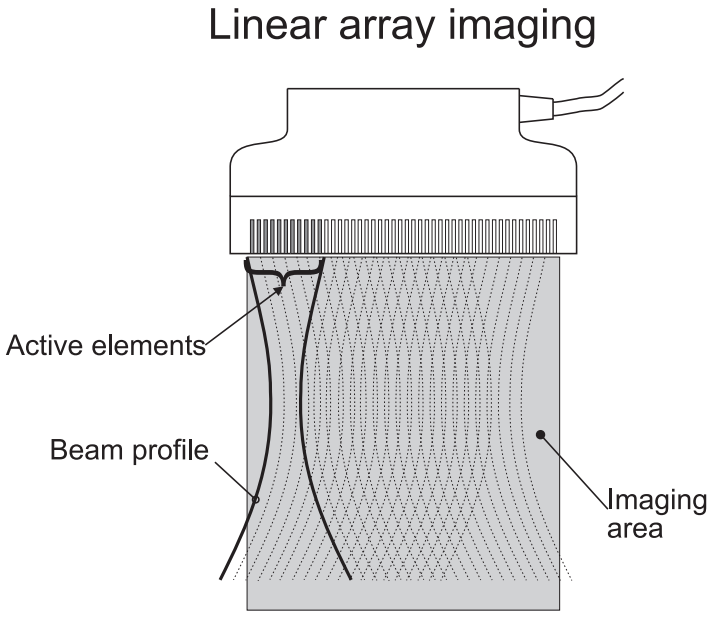

Figure 3.8: Linear array transducer for obtaining a rectangular cross-sectional image.

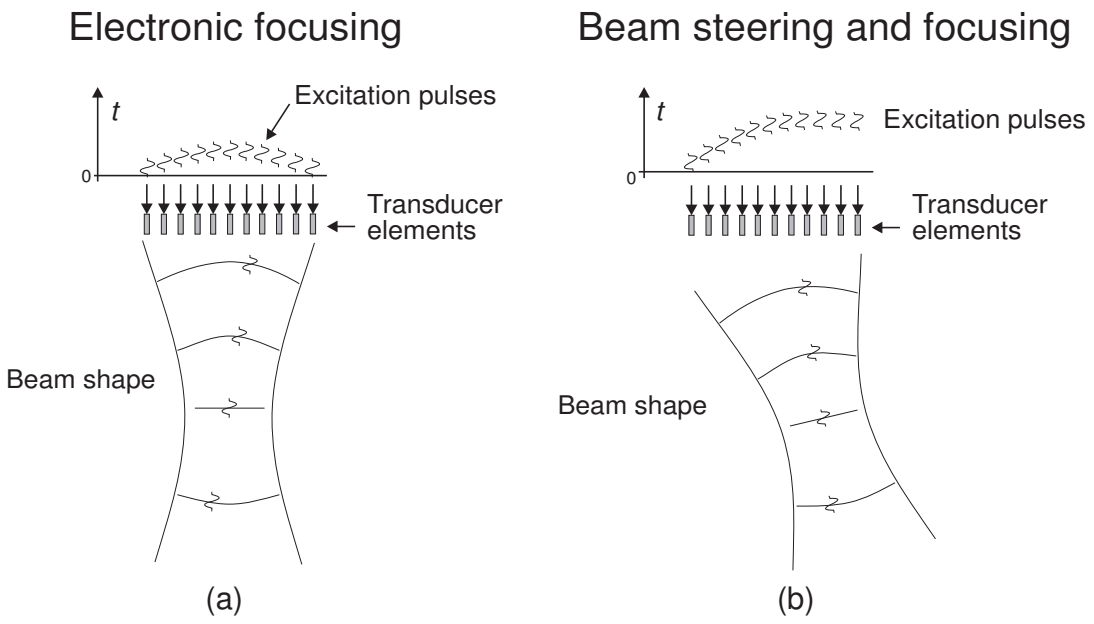

Figure 3.9: Electronic focusing and steering of an ultrasound beam.

investigation by firing a set of elements situated over the region. The beam is moved over the imaging region by firing sets of contiguous elements. Focusing in transmit is achieved by delaying the excitation of the individual elements, so an initially concave beam shape is emitted, as shown in Fig. 3.9.

The beam can also be focused during reception by delaying and adding responses from the different elements. A continuous focus or several focal zones can be maintained as explained in Section 3.2. Only one focal zone is possible in transmit, but a composite image using a set of foci from several transmissions can be made. Often 4 to 8 zones can be individually placed at selected depths in modern scanners. The frame rate is then lowered by the number of transmit foci.

The linear arrays acquire a rectangular image, and the arrays can be quite large to cover a sufficient region of interest (ROI). A larger area can be scanned with a smaller array, if the elements are placed on a convex surface as shown in Fig. 3.10. A sector scan is then obtained. The method of focusing and beam sweeping during transmit and receive is the same as for the linear array, and a substantial number of elements (often 128 or 256) is employed.

The convex and linear arrays are often too large to image the heart when probing between the ribs. A small array size can be used and a large field of view attained by using a phased array as shown in Fig. 3.11. All array elements are used here both during transmit and receive. The direction of the beam is steered by electrically delaying the signals to or from the elements, as shown in Fig. 3.9b. Images can be acquired through a small window and the beam rapidly sweeped over the ROI. The rapid steering of the beam compared to mechanical transducers is of especial importance in flow imaging. This has made the phased array the choice for cardiological investigations through the ribs.

More advanced arrays are even being introduced these years with the increase in number of elements and digital beamforming. Especially elevation focusing (out of the imaging plane) is important. A curved surface as shown in Fig. 3.12 is used for obtaining the elevation focusing essential for an improved image quality. Electronic beamforming can also be used in the elevation direction by dividing the elements in the elevation direction. The elevation focusing in receive can then be dynamically controlled for *e.g.* the array shown in Fig. 3.13.

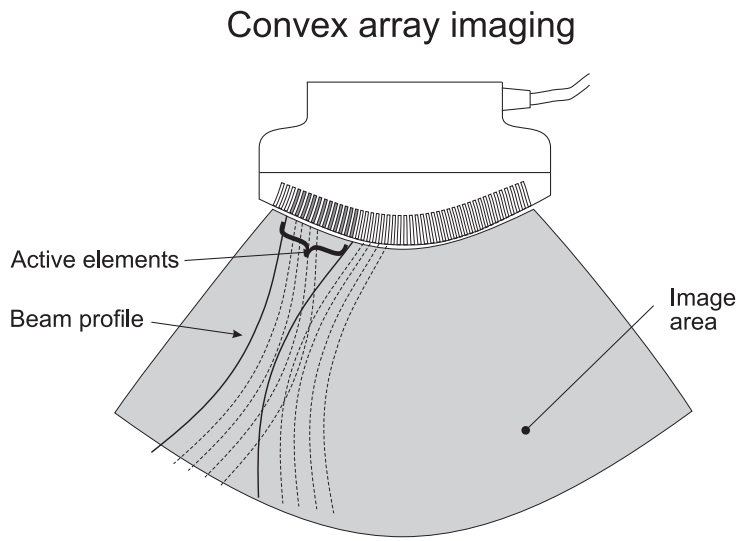

Figure 3.10: Convex array transducer for obtaining a polar cross-sectional image.

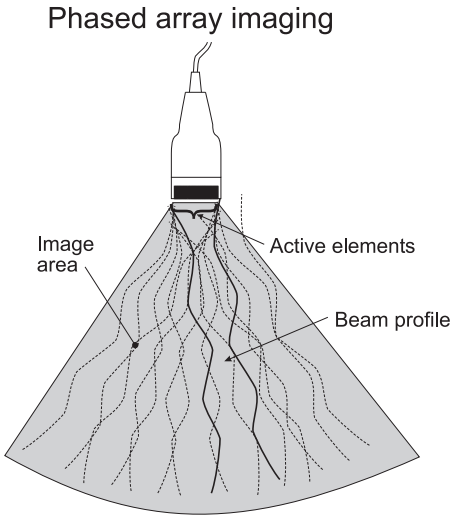

Figure 3.11: Phased array transducer for obtaining a polar cross-sectional image using a transducer with a small foot-print.

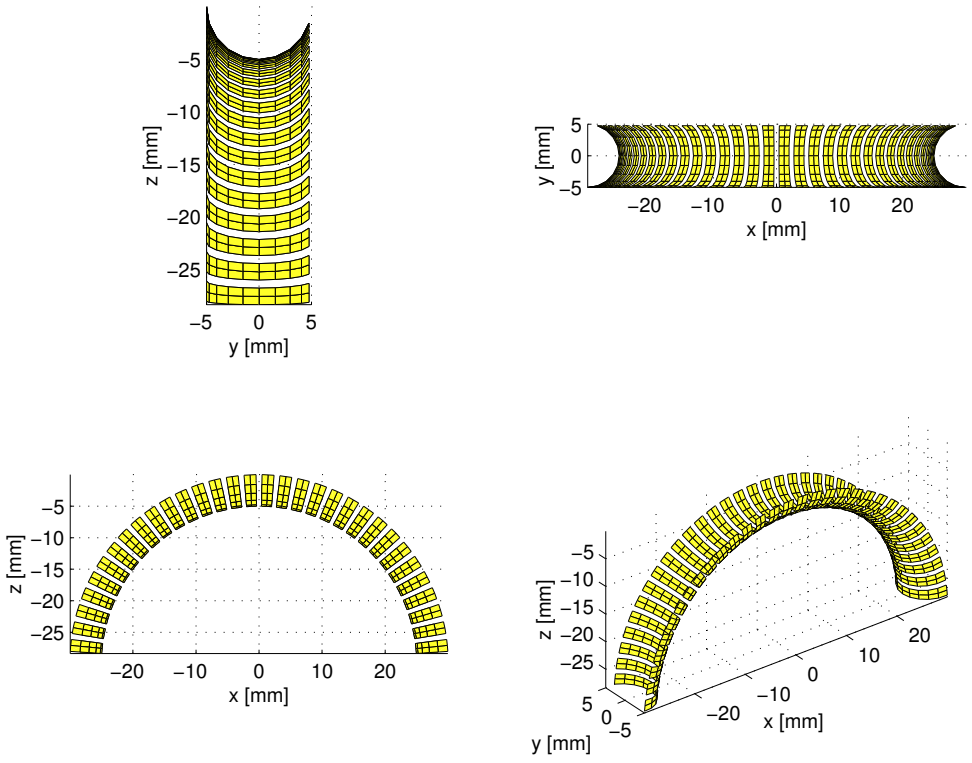

Figure 3.12: Elevation focused convex array transducer for obtaining a rectangular cross-sectional image, which is focused in the out-of-plane direction. The curvature in the elevation direction is exaggerated in the figure for illustration purposes.

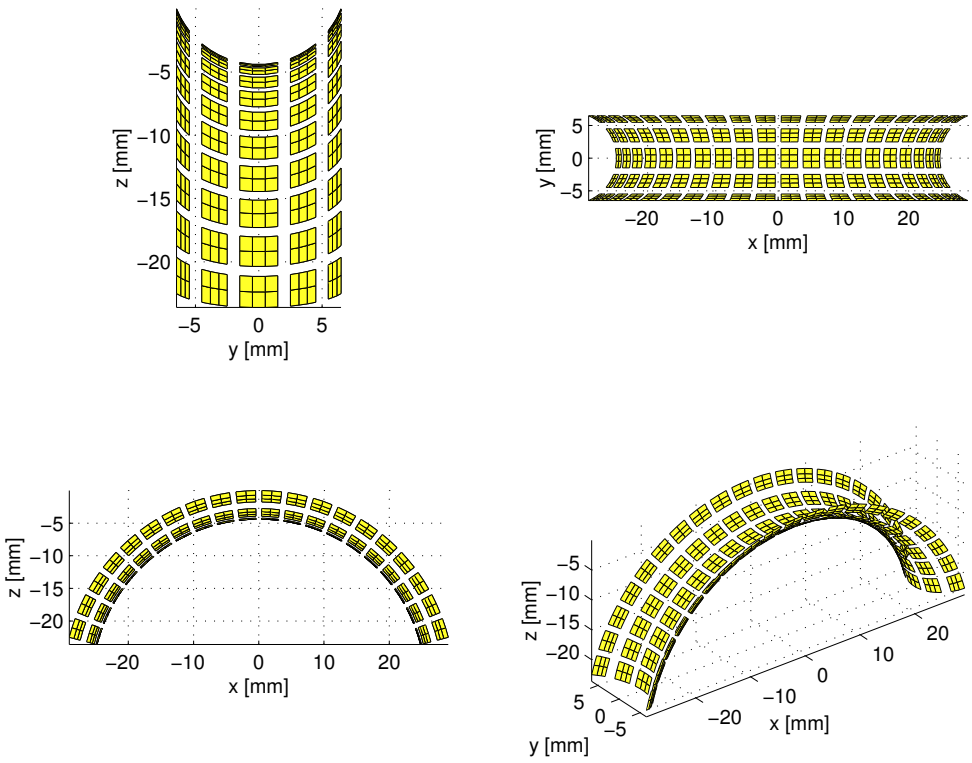

Figure 3.13: Elevation focused convex array transducer with element division in the elevation direction. The curvature in the elevation direction is exaggerated in the figure for illustration purposes

3.5 Simulation of ultrasound imaging

One of the first steps in designing an ultrasound system is the selection of the appropriate number of elements for the array transducers and the number of channels for the beamformer. The focusing strategy in terms of number of focal zones and apodization must also be determined. These choices are often not easy, since it is difficult to determine the effect in the resulting images of increasing the number of channels and selecting more or less advanced focusing schemes. It is therefore beneficial to simulate the whole imaging system in order to quantify the image quality.

The program Field II was rewritten to make it possible to simulate the whole imaging process with time varying focusing and apodization as described in [38] and [21]. This has paved the way for doing realistic simulated imaging with multiple focal zones for transmission and reception and for using dynamic apodization. It is hereby possible to simulate ultrasound imaging for all image types including flow images, and the purpose of this section is to present some standard simulation phantoms that can be used in designing and evaluating ultrasound transducers, beamformers and systems. The phantoms described can be divided into ordinary string/cyst phantoms, artificial human phantoms and flow imaging phantoms. The ordinary computer phantoms include both a string phantoms for evaluating the point spread function as a function of spatial positions as well as a cyst/string phantom. Artificial human phantoms of a fetus in the third month of development and an articial kedney are also shown. The simulation of flow and the associated phantoms will be described in Section 4.5. All the phantoms can be used with any arbitrary transducer configuration like single element, linear, convex, or phased array transducers, with any apodization and focusing scheme.

3.5.1 Simulation model

The first simple treatment of ultrasound is often based on the reflection and transmission of plane waves. It is assumed that the propagating wave impinges on plane boundaries between tissues with different mean acoustic properties. Such boundaries are rarely found in the human body, and seldom show on ultrasound images. This is demonstrated by the image shown in Fig. 3.14. Here the skull of the fetus is not clearly marked. It is quite obvious that there is a clear boundary between the fetus and the surrounding amniotic fluid. The skull boundary is not visible in the image, because the angle between the beam and the boundary has a value such that the sound bounces off in another direction, and, therefore, does not reach the transducer. Despite this, the extent of the head can still be seen. This is due to the scattering of the ultrasound wave. Small changes in density, compressibility, and absorption give rise to a scattered wave radiating in all directions. The backscattered field is received by the transducer and displayed on the screen. One might well argue that scattering is what makes ultrasound images useful for diagnostic purposes, and it is, as will be seen later, the physical phenomena that makes detection of blood velocities possible. Ultrasound scanners are, in fact, optimized to show the backscattered signal, which is considerably weaker than that found from reflecting boundaries. Such reflections will usually be displayed as bright white on the screen, and can potentially saturate the receiving circuits in the scanner. An example can be seen at the neck of the fetus, where a structure is perpendicular to the beam. This strong reflection saturates the input amplifier of this scanner. Typical boundary reflections are encountered from the diaphragm, blood vessel walls, and organ boundaries.

An enlarged view of an image of a liver is seen in Fig. 3.15. The image has a grainy appearance, and not a homogeneous gray or black level as might be expected from homogeneous liver tissue. This type of pattern is called speckle. The displayed signals are the backscatter from the liver tissue, and are due to connective tissue, cells, and fibrious tissue in the liver. These structures are much smaller than one wavelength of the ultrasound, and the speckle pattern displayed does not directly reveal physical structure. It is rather the constructive and destructive interference of scattered signals from all the small structures. So it is not possible to visualize and diagnose microstructure, but the strength of the signal is an indication of pathology. A strong signal from liver tissue, making a bright image, is, *e.g.*, an indication of a fatty or cirrhotic liver.

As the scattered wave emanates from numerous contributors, it is appropriate to characterize it in statistical terms. The amplitude distribution follows a Gaussian distribution [39], and is, thus, fully characterized by its mean and variance. The mean value is zero since the scattered signal is generated by differences in the tissue from the mean acoustic properties.

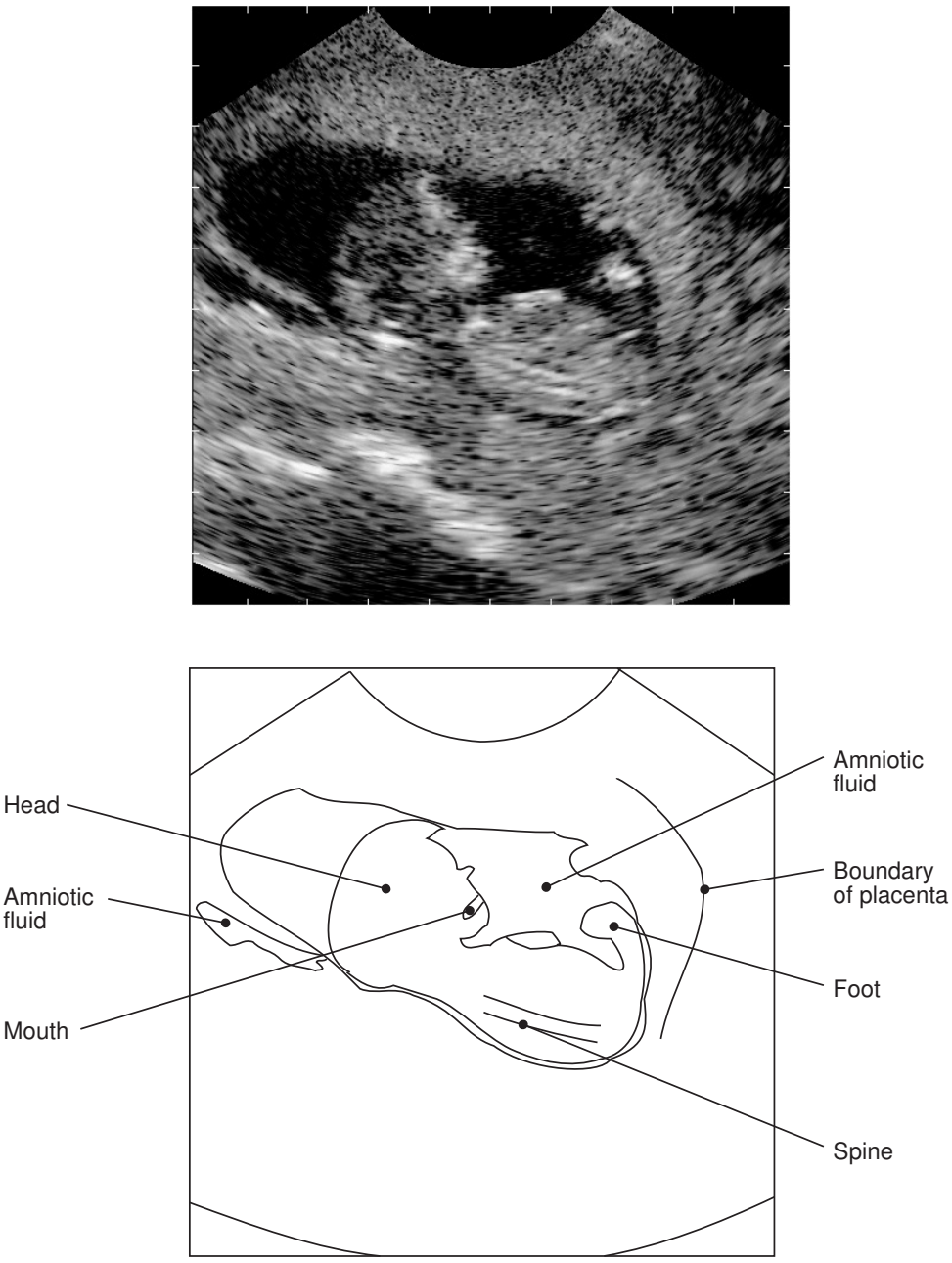

Figure 3.14: Ultrasound image of a 13th week fetus. The markers at the border of the image indicate one centimeter (from [9], Copyright Cambridge University Press).

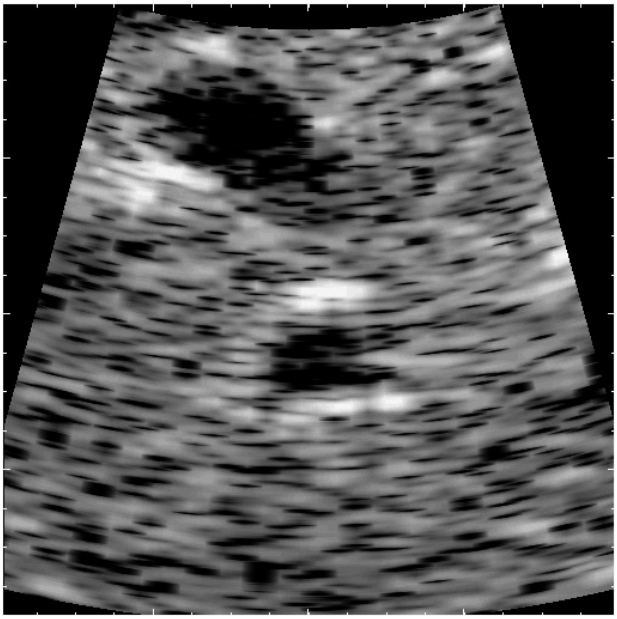

Figure 3.15: 4 $\times$ 4 cm image of a human liver from a healthy 28-year-old man. The completely dark areas are blood vessels (from [9], Copyright Cambridge University Press).

Although the backscattered signal is characterized in statistical terms, one should be careful not to interpret the signal as random in the sense that a new set of values is generated for each measurement. The same signal will result, when a transducer is probing the same structure, if the structure is stationary. Even a slight shift in position will yield a backscattered signal correlated with that from the adjacent position. The shift over which the signals are correlated is essentially dependent on the extent of the ultrasound field. This can also be seen from the image in Fig. 3.15, as the laterally elongated white speckles in the image indicate transverse correlation. The extent of these speckle spots is a rough indication of the point spread function of the system.

The correlation between different measurements is what makes it possible to estimate blood velocities with ultrasound. As there is a strong correlation for small movements, it is possible to detect shifts in position by comparing or, more strictly, correlating successive measurements of moving structure, *e.g.*, blood cells.

Since the backscattered signal depends on the constructive and destructive interference of waves from numerous small tissue structures, it is not meaningful to talk about the reflection strength of the individual structures. Rather, it is the deviations within the tissue and the composition of the tissue that determine the strength of the returned signal. The magnitude of the returned signal is, therefore, described in terms of the power of the scattered signal. Since the small structures reradiate waves in all directions and the scattering structures might be ordered in some direction, the returned power will, in general, be dependent on the relative position between the ultrasound emitter and receiver. Such a medium is called anisotropic, examples of which are muscle and kidney tissue. By comparison, liver tissue is a fairly isotropic scattering medium, when its major vessels are excluded, and so is blood.

It is, thus, important that the simulation approach models the scattering mechanisms in the tissue. This is essentially what the model derived in Chapter 2 does. Here the received signal from the transducer is:

$$p_r(\vec{r},t) = v_{pe}(t) \underset{t}{\star} f_m(\vec{r}) \underset{r}{\star} h_{pe}(\vec{r},t) \tag{3.34}$$

where $\underset{r}{\star}$ denotes spatial convolution. v_{pe} is the pulse-echo impulse, which includes the transducer excitation and the electro-mechanical impulse response during emission and reception of the pulse. f_m accounts for the inhomogeneities

in the tissue due to density and propagation velocity perturbations which give rise to the scattered signal. h_{pe} is the pulse-echo spatial impulse response that relates the transducer geometry to the spatial extent of the scattered field. Explicitly written out these terms are:

$$v_{pe}(t) = \frac{\rho}{2c^2} E_m(t) \underset{t}{\star} \frac{\partial^3 v(t)}{\partial t^3}, \qquad f_m(\vec{r}_1) = \frac{\Delta\rho(\vec{r})}{\rho} - \frac{2\Delta c(\vec{r})}{c}, \qquad h_{pe}(\vec{r},t) = h_t(\vec{r},t) * h_r(\vec{r},t) \tag{3.35}$$

So the received response can be calculated by finding the spatial impulse response for the transmitting and receiving transducer and then convolving with the impulse response of the transducer. A single RF line in an image can be calculated by summing the response from a collection of scatterers in which the scattering strength is determined by the density and speed of sound perturbations in the tissue. Homogeneous tissue can thus be made from a collection of randomly placed scatterers with a scattering strength with a Gaussian distribution, where the variance of the distribution is determined by the backscattering cross-section of the particular tissue. This is the approach taken in these notes.

The computer phantoms typically consist of 100,000 or more discrete scatterers, and simulating 50 to 128 RF lines can take several days depending on the computer used. It is therefore beneficial to split the simulation into concurrently run sessions. This can easily be done by first generating the scatterer's position and amplitude and then storing them in a file. This file can then the be used by a number of workstations to find the RF signal for different imaging directions, which are then stored in separate files; one for each RF line. These files are then used to assemble an image. This is the approach used for the simulations shown here in which 3 Pentium Pro 200 MHz PCs can generate one phantom image over night using Matlab 5 and the Field II program.

3.6 Synthetic phantoms

The first synthetic phantom consists of a number of point targets placed with a distance of 5 mm starting at 15 mm from the transducer surface. A linear sweep image of the points is then made and the resulting image is compressed to show a 40 dB dynamic range. This phantom is suited for showing the spatial variation of the point spread function for a particular transducer, focusing, and apodization scheme.

Twelve examples using this phantom are shown in Fig. 3.16. The top graphs show imaging without apodization and the bottom graphs show images when a Hanning window is used for apodization in both transmit and receive. A 128 elements transducer with a nominal frequency of 3 MHz was used. The element height was 5 mm, the width was a wavelength and the kerf 0.1 mm. The excitation of the transducer consisted of 2 periods of a 3 MHz sinusoid with a Hanning weighting, and the impulse response of both the emit and receive aperture also was a two cycle, Hanning weighted pulse. In the graphs A – C, 64 of the transducer elements were used for imaging, and the scanning was done by translating the 64 active elements over the aperture and focusing in the proper points. In graph D and E 128 elements were used and the imaging was done solely by moving the focal points.

Graph A uses only a single focal point at 60 mm for both emission and reception. B also uses reception focusing at every 20 mm starting from 30 mm. Graph C further adds emission focusing at 10, 20, 40, and 80 mm. D applies the same focal zones as C, but uses 128 elements in the active aperture.

The focusing scheme used for E and F applies a new receive profile for each 2 mm. For analog beamformers this is a small zone size. For digital beamformers it is a large zone size. Digital beamformer can be programmed for each sample and thus a "continuous" beamtracking can be obtained. In imaging systems focusing is used to obtain high detail resolution and high contrast resolution preferably constant for all depths. This is not possible, so compromises must be made. As an example figure F shows the result for multiple transmit zones and receive zones, like E, but now a restriction is put on the active aperture. The size of the aperture is controlled to have a constant F-number (depth of focus in tissue divided by width of aperture), 4 for transmit and 2 for receive, by dynamic apodization. This gives a more homogeneous point spread function throughout the full depth. Especially for the apodized version. Still it can be seen that the composite transmit can be improved in order to avoid the increased width of the point spread function at e.g. 40 and 60 mm.

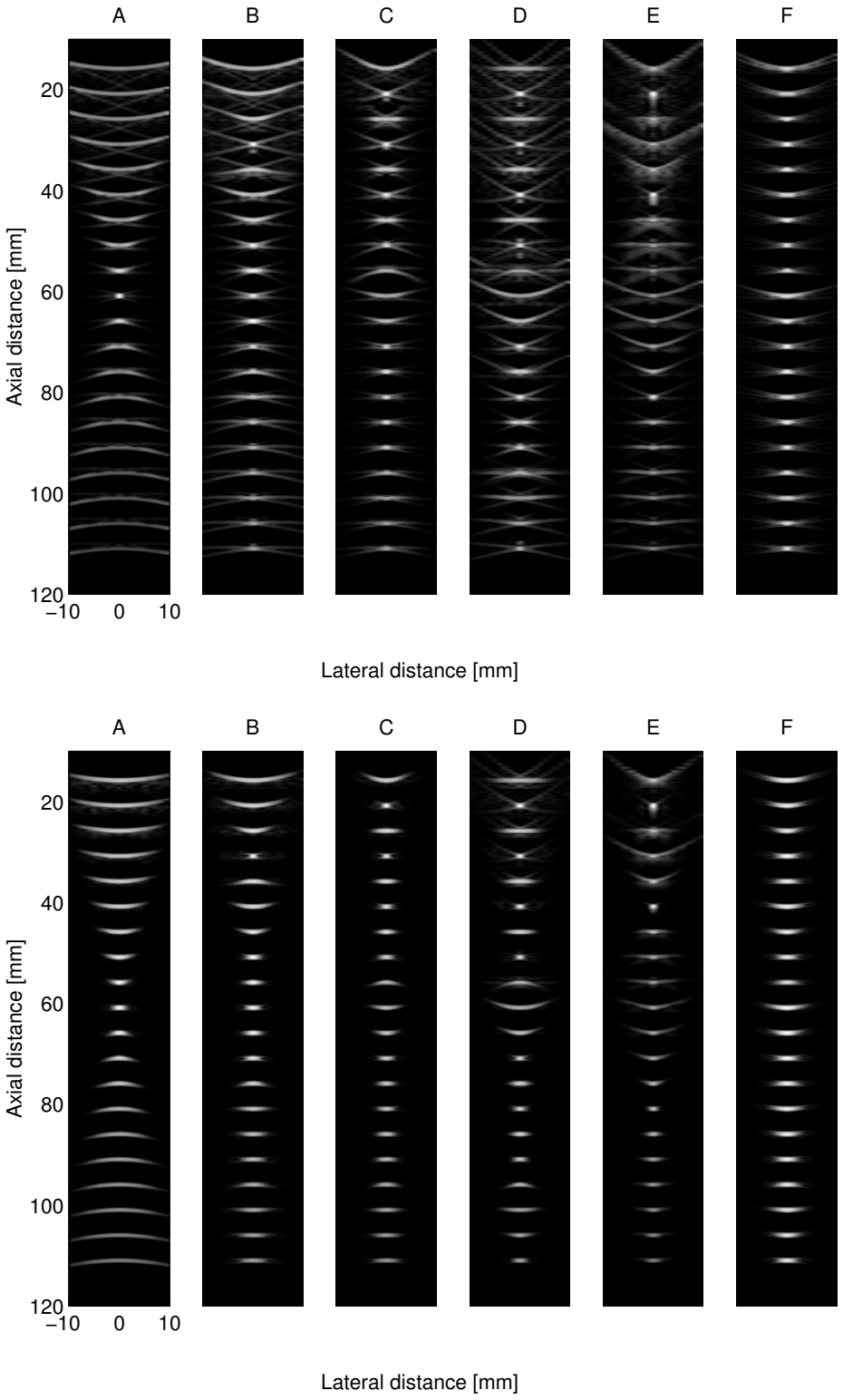

Figure 3.16: Point target phantom imaged for different set-up of transmit and receive focusing and apodization. See text for an explanation of the set-up.

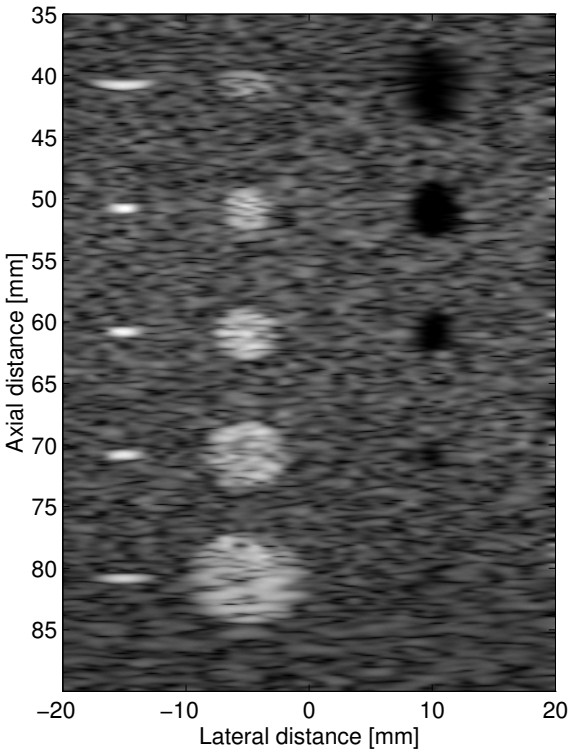

Figure 3.17: Computer phantom with point targets, cyst regions, and strongly reflecting regions.

The next phantom consists of a collection of point targets, five cyst regions, and five highly scattering regions. This can be used for characterizing the contrast-lesion detection capabilities of an imaging system. The scatterers in the phantom are generated by finding their random position within a $60 \times 40 \times 15$ mm cube, and then ascribe a Gaussian distributed amplitude to the scatterers. If the scatterer resides within a cyst region, the amplitude is set to zero. Within the highly scattering region the amplitude is multiplied by 10. The point targets has a fixed amplitude of 100, compared to the standard deviation of the Gaussian distributions of 1. A linear scan of the phantom was done with a 192 element transducer, using 64 active elements with a Hanning apodization in transmit and receive. The element height was 5 mm, the width was a wavelength and the kerf 0.05 mm. The pulses where the same as used for the point phantom mentioned above. A single transmit focus was placed at 60 mm, and receive focusing was done at 20 mm intervals from 30 mm from the transducer surface. The resulting image for 100,000 scatterers is shown in Fig. 3.17. A homogeneous speckle pattern is seen along with all the features of the phantom.

3.7 Anatomic phantoms

The anatomic phantoms are attempts to generate images as they will be seen from real human subjects. This is done by drawing a bitmap image of scattering strength of the region of interest. This map then determines the factor multiplied onto the scattering amplitude generated from the Gaussian distribution, and models the difference in the density and speed of sound perturbations in the tissue. Simulated boundaries were introduced by making lines in the scatterer map along which the strong scatterers were placed. This is marked by completely white lines shown in the scatterer maps. The model is currently two-dimensional, but can readily be expanded to three dimensions. Currently, the elevation direction is merely made by making a 15 mm thickness for the scatterer positions, which are randomly distributed in the interval.

Two different phantoms have been made; a fetus in the third month of development and a left kidney in a longitudinal

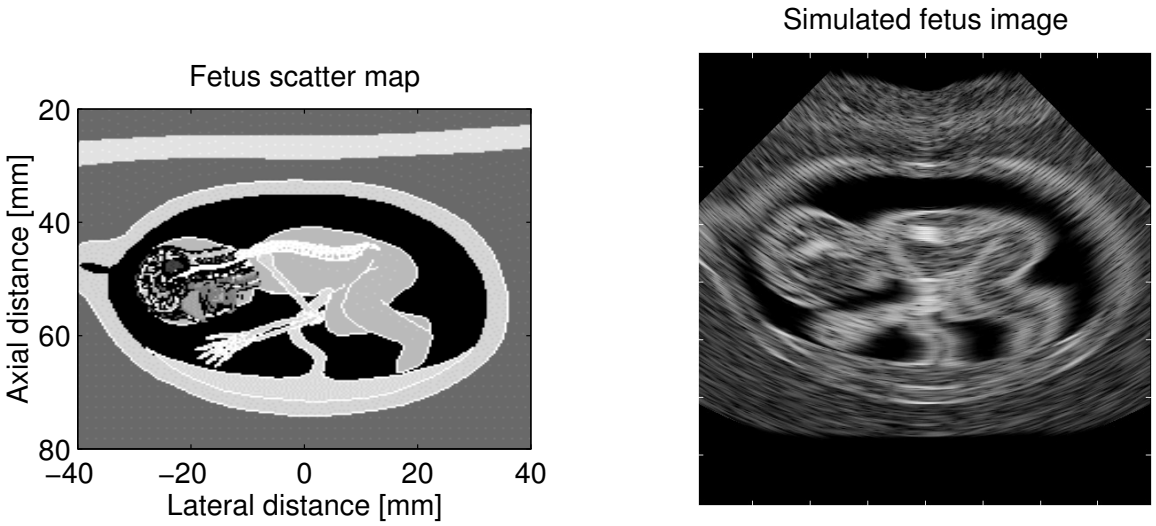

Figure 3.18: Simulation of artificial fetus.

scan. For both was used 200,000 scatterers randomly distributed within the phantom, and with a Gaussian distributed scatterer amplitude with a standard deviation determined by the scatterer map. The phantoms were scanned with a 5 MHz 64 element phased array transducer with $\lambda/2$ spacing and Hanning apodization. A single transmit focus 70 mm from the transducer was used, and focusing during reception is at 40 to 140 mm in 10 mm increments. The images consists of 128 lines with 0.7 degrees between lines.

Fig. 3.19 shows the artificial kidney scatterer map on the left and the resulting image on the right. Note especially the bright regions where the boundary of the kidney is orthogonal to the ultrasound, and thus a large signal is received. Note also the fuzziness of the boundary, where they are parallel with the ultrasound beam, which is also seen on actual ultrasound scans. Fig. 3.18 shows the fetus. Note how the anatomy can be clearly seen at the level of detail of the scatterer map. The same boundary features as for the kidney image is also seen.

The images have many of the features from real scan images, but still lack details. This can be ascribed to the low level of details in the bitmap images, and that only a 2D model is used. But the images do show great potential for making powerful fully synthetic phantoms, that can be used for image quality evaluation.

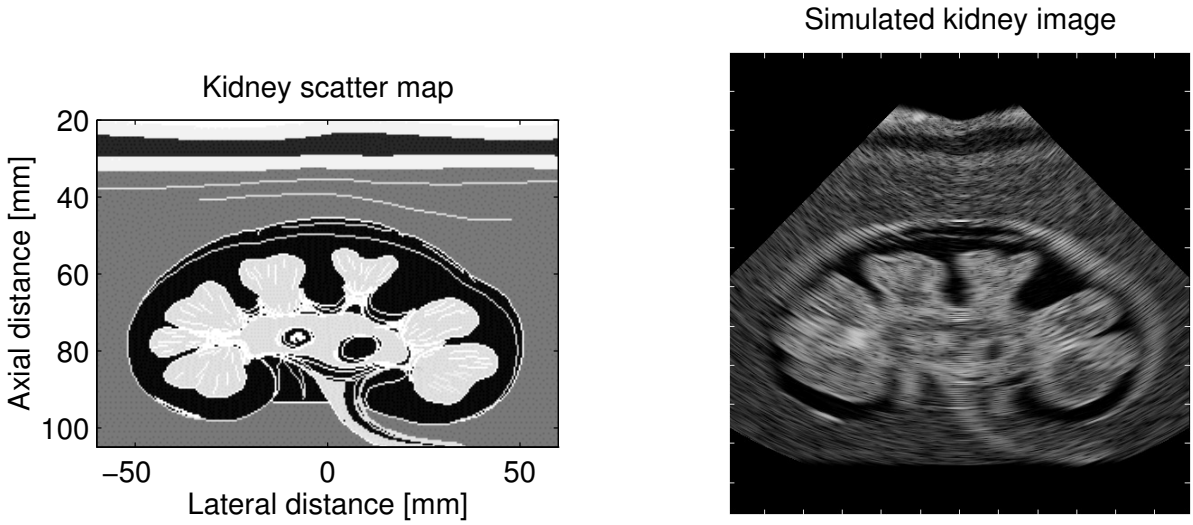

Figure 3.19: Simulation of artificial kidney.

CHAPTER

FOUR

Ultrasound Velocity Imaging

This chapter is taken from the book chapter:

Jørgen Arendt Jensen :

Ultrasound Velocity Imaging

Ultrasound Imaging and Therapy. ed. / Aaron Fenster; James C. Lacefield. CRC Taylor and Francis Group, 2015. p. 65-99 (Imaging in medical diagnosis and therapy)

4.1 Introduction: Blood Velocity Estimation Systems

This Chapter gives an introduction to velocity estimation in medical ultrasound, which is primarily used in cardiovascular imaging, but it can also be applied in *e.g.* strain imaging and tissue motion estimation. The Chapter gives a brief introduction to the human circulation to establish the requirements on blood velocity estimation systems. A simple model for the interaction between ultrasound and point scatterers is derived in Section 4.4 based on the information about scattering from blood in Section 4.3. The model is used in the derivation of velocity estimators based on the signal's frequency content (Section 4.6), phase shift (Section 4.7), and time shift (Section 4.8). These Sections should give a brief introduction to the function of the most prominent methods used in current commercial ultrasound scanners. Newer and more experimental techniques are described in the Sections on vector velocity imaging, synthetic aperture imaging and other applications in Sections 4.9 to 4.12.

The Chapter is necessarily brief in covering the many topics of this field, and the reader is referred to the more in-depth treatment of the topics in [9, 40, 41, 42, 43] along with the references given in the text.

4.2 The human circulation

The major arteries and veins in the human circulation are shown in Fig. 4.1, and the dimensions are indicated in Table 4.1. Their diameters span from cm to microns and the velocities from m/s to less than mm/s in the capillaries. As illustrated, the vessel constantly curves and branches and repeatedly changes dimensions [44]. The blood flow is pulsatile, and the velocity rapidly changes both magnitude and direction as can be seen from the large difference between peak and mean velocities. In addition the peak Reynolds number is often above 2000, which indicates disturbed or turbulent flow in parts of the cardiac cycle.

All of these factors should be considered when devising a system for measuring blood the velocity in the human circulation. Foremost it must be a fast measurement system with 1 – 20 ms temporal resolution to follow the changes in velocity due to the acceleration from the pulsation. It should also have sub-millimeter spatial resolution in order to see changes in flow over space and visualize small vessels. A real-time system is also beneficial, since the flow patterns change rapidly, and it must be possible to quickly find the sites of flow. The system should ideally also be capable of finding and visualizing flow in all directions, since turbulent flow and vortices exists throughout the human circulation. Modern medical ultrasound systems can fulfill many of these demands, and the remaining part of this Chapter describes the physics and signal processing needed to perform velocity estimation along the ultrasound beam and in other directions.

4.3 Ultrasound scattering from blood

The constituents of blood are shown in Table 4.2. The most prominent part is the erythrocytes (red blood cells), where a mm^3 of blood contains roughly 5 million cells. The resolution of ultrasound systems is at best on the order of the cube of the wavelength λ^3, which is given by $\lambda = c/f_0$, where c is the speed of sound and f_0 the center frequency. For a 6 MHz system $\lambda = 0.26$ mm, which is much larger than a single cell. An ultrasound system, thus, only observes a large, random collection of cells.

The scattering from a single point scatterer or small cell can be described by the differential scattering cross section, σ_d. It is defined as the power scattered per unit solid angle at some angle Θ_s divided by the incident intensity [11, 51]:

$$\sigma_d(\Theta_s) = \frac{V_e^2 \pi^2}{\lambda^4} \left[\frac{\kappa_e - \kappa_0}{\kappa_0} + \frac{\rho_e - \rho_0}{\rho_e} \cos \Theta_s \right]^2 , \tag{4.1}$$

where V_e is the volume of the scatterer, ρ_e is a small perturbation in density and κ_e in compressibility from their mean values ρ_0, κ_0. This results in a scattered field as shown in Fig. 4.2, where the scattering is dependent on the angle. It can, however, be seen that a signal is received in all directions.

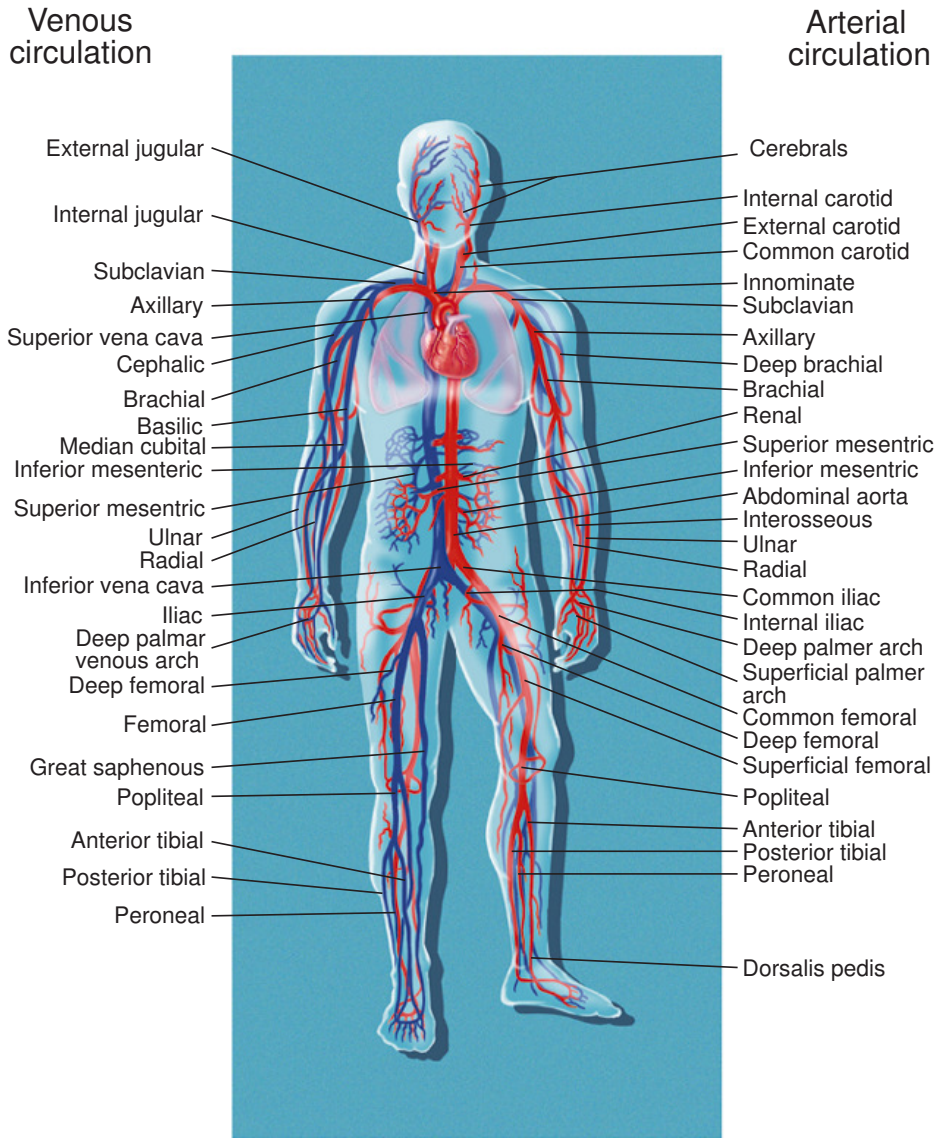

Figure 4.1: Major arteries and veins in the body (reprinted with permission from Abbott Laboratories, Illinois, USA).

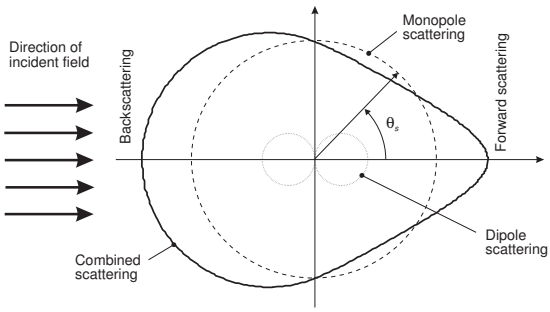

Figure 4.2: Monopole and dipole scattering from a perturbation in either compressibility or density (from [9]).

Table 4.1: Typical dimensions and flows of vessels in the human vascular system (data taken from [45, 46] and Table adapted from [9]).

Vessel	Internal diameter cm	Wall thickness cm	Length cm	Young's modulus $N/m^2 \cdot 10^5$
Ascending aorta	1.0 – 2.4	0.05 – 0.08	5	3 – 6
Descending aorta	0.8 – 1.8	0.05 – 0.08	20	3 – 6
Abdominal aorta	0.5 – 1.2	0.04 – 0.06	15	9 – 11
Femoral artery	0.2 – 0.8	0.02 – 0.06	10	9 – 12
Carotid artery	0.2 – 0.8	0.02 – 0.04	10 – 20	7 – 11
Arteriole	0.001 – 0.008	0.002	0.1 – 0.2	
Capillary	0.0004 – 0.0008	0.0001	0.02 – 0.1	
Inferior vena cava	0.6 – 1.5	0.01 – 0.02	20 – 40	0.4 – 1.0

Vessel	Peak velocity cm/s	Mean velocity cm/s	Reynolds number (peak)	Pulse propagation velocity cm/s
Ascending aorta	20 – 290	10 – 40	4500	400 – 600
Descending aorta	25 – 250	10 – 40	3400	400 – 600
Abdominal aorta	50 – 60	8 – 20	1250	700 – 600
Femoral artery	100 – 120	10 – 15	1000	800 – 1030
Common Carotid artery (range)	68 – 171	19-59		600 – 1100
Common Carotid artery (mean)	108	39		600 – 1100
Arteriole	0.5 – 1.0		0.09	
Capillary	0.02 – 0.17		0.001	
Inferior vena cava	15 – 40		700	100 – 700

	Mass density g/cm^3	Adiabatic compressibility 10^{-12} cm/dyne	Size μm	Particles per mm^3
Erythrocytes	1.092	34.1	2×7	$5 \cdot 10^6$
Leukocytes	-	-	9 – 25	$8 \cdot 10^3$
Platelets	-	-	2 – 4	$250 - 500 \cdot 10^3$
Plasma	1.021	40.9	-	-
0.9% saline	1.005	44.3	-	-

Table 4.2: Properties of the main components of blood. Data from [47, 48, 49, 50] and Table adapted from [9].

The signal received by the ultrasound transducer is therefore independent of the orientation of the vessel and it can be modeled as a random, Gaussian signal, as it emanates from a large collection of independent random scatterers. This give rise to the speckle pattern seen in ultrasound images. The scattering is very weak, as the density and compressibility perturbations are small compared to the surrounding tissue, and often the signal from blood is 20-40 dB lower than from the surrounding tissue. Vessels in an ultrasound image therefore appear black.

It should be noted that the signal received is random, but the same signal is received, if the experiment is repeated for the exact same collection of scatterers. This is a very important feature of ultrasound blood velocity signals and is heavily used in these systems, as will be clear in the following Sections. A small motion of the scatterers will therefore yield a second signal highly correlated with the first signal, when the motion $|v|T_{prf}$ is small compared to the beam width, and the velocity gradient is small across the scatterer collection observed. Here $|v|$ is velocity magnitude and T_{prf} is the time between the measurements.

4.4 Ultrasound signals from flowing blood

The derivation of velocity estimation methods is based on a model of ultrasound interaction between the moving blood and the ultrasound pulse. The model has to capture all the main features of the real received signal without unnecessary features and complications. This section will present a simple model for this interaction, which can readily be used for deriving new estimators and also give basic explanations for how to optimize the techniques. It can also be further expanded to the two- and three-dimensional velocity estimation methods presented in Sections 4.9 and 4.10.

The scattering from blood emanates from a large collection of independent, small point scatterers as described in Section 4.3. The one-dimensional received signal $y(t)$ can therefore be modeled as:

$$y(t) = p(t) * s(t), \tag{4.2}$$

which is the convolution of the basic ultrasound pulse $p(t)$ with the Gaussian, random scattering signal $s(t)$. The ultrasound pulse for flow estimation consists of a number of sinusoidal oscillations ($M_p = 4 - 8$) at the transducer's center frequency, f_0, convolved with the electro-mechanical impulse response of the transducer (from excitation voltage to pressure and from pressure to received voltage) [52]. Modern transducers are so broad band that a simple approximation is given by

$$p(t) = g(t)\sin(2\pi f_0 t), \tag{4.3}$$

where the envelope $g(t)$ is one from $t = 0$ to M_p/f_0 and zero elsewhere.

For a single point scatterer, the scattering can be modeled as a δ-function and the received signal is

$$y_1(t) = p(t) * a\delta\left(t - \frac{2d}{c}\right) = ap\left(t - \frac{2d}{c}\right), \tag{4.4}$$

where d is the distance to the point, c is the speed of sound (1540 m/s in tissue), and a is the scattering amplitude. There is, thus, a propagation delay $2d/c$ between transmitting the signal and receiving the response. For a moving scatterer this response will change as the scatterer moves farther away from the transducer. For a scatterer velocity of $v_z = |v|\cos\theta$ in the axial direction, and a time between measurements of T_{prf}, the second received signal is

$$y_2(t) = p(t) * a\delta\left(t - \frac{2d}{c} - \frac{2v_z T_{prf}}{c}\right) = ap\left(t - \frac{2d}{c} - \frac{2v_z T_{prf}}{c}\right). \tag{4.5}$$

Note that $v_z T_{prf} = T_{prf}|v|\cos\theta$ is the distance the scatterer moved along the ultrasound beam direction, where θ is the beam-to-flow angle. There is therefore an added delay of

$$t_s = \frac{2v_z}{c} T_{prf} \tag{4.6}$$

before the second signal is received. This is directly proportional to the velocity of the moving scatterer, and by determining this delay the axial velocity can directly be calculated. This can be achieved either through the phase shift

estimator described in Section 4.7 or the time shift estimator in Section 4.8. Both estimators essentially just compare or correlate two received signals and find the shift in position between the received responses.

Combining (4.3) and (4.5) gives a model for the received signal for a number of pulse emissions [53, 54]:

$$y(t,i) = ap(t - \frac{2d}{c} - i\frac{2v_z}{c}T_{prf}) = ag(t - \frac{2d}{c} - it_s)\sin(2\pi f_0(t - \frac{2d}{c} - it_s)). \tag{4.7}$$

Here i is the pulse emission number. For pulsed systems the received signal is measured at a single depth corresponding to a fixed time t_x relative to the pulse emission. This is performed by taking out one sample from each pulse emission to create the sampled signal. To simplify things it can assumed that the pulse is long enough and the motion slow enough, so that the pulse amplitude stays roughly constant during the observation time. The sampled signal can then simply be written as

$$\begin{aligned} y(t_x,i) &= a\sin(2\pi f_0(t_x - \frac{2d}{c} - it_s)) \\ &= -a\sin(2\pi\frac{2v_z}{c}f_0 iT_{prf} - \phi_x). \end{aligned} \tag{4.8}$$

Here $\phi_x = 2\pi f_0(\frac{2d}{c} - t_x)$ is a fixed phase shift depending on the measurement depth. The sampling interval is T_{prf} and the frequency of the sampled signal is

$$f_p = \frac{2v_z}{c}f_0, \tag{4.9}$$

which is directly proportional to the velocity. Thus, estimating the frequency of this sampled signal $y(t_x,i)$ can directly reveal the axial velocity as described in the Section 4.6 on spectral velocity estimation. Often it is advantageous to also sample the signal in the depth direction, and this gives

$$y_s(n,i) = ag(n\Delta T - \frac{2d}{c} - it_s)\sin(2\pi f_0(n\Delta T - \frac{2d}{c} - it_s)), \tag{4.10}$$

which is often employed for averaging along the depth direction. Here $\Delta T = 1/f_s$ is the sampling interval and f_s the sampling frequency.

An illustration of the sampling process for a single moving scatterer is shown in Fig. 4.3, where the individual received signals are shown on the left graph. The scatterer is moving away from the transducer, and the time between emission and reception of the signal increases. A single sample is taken out for each received signal at the position of the red line. The resulting sampled signal is shown on the right graph, where the basic emitted pulse can be recognized. A low velocity will yield a long pulse and hence a low frequency of the received signal as indicated by (4.9). A high velocity will compress the signal and thereby give a high frequency. The velocity can be found by three different methods. A Fourier transform can be applied on the signal in the right graph to find the frequency as described in Section 4.6. The phase shift can be determined between the received signals. This is described in Section 4.7. The time shift can be found by correlating consecutive received signals, *i.e.* cross-correlating received signals in the left graph as described in Section 4.8.

The signal model can also be expanded to include a collection of scatterers moving at the same velocity

$$y(t,i) = p(t) * s(t - it_s - iT_{prf}) = p(t - it_s - iT_{prf}) * s(t) = p(t - it_s) * s(t). \tag{4.11}$$

as the same pulse is emitted every time. Using superposition this can just be seen as a summation of individual scatterers moving at their velocity and the model and observations made above can readily be applied.

4.4.1 Is it the Doppler effect?

The ultrasound systems for measuring velocity are often called Doppler systems implying that they rely on the Doppler shift to find the velocity. It is debatable whether this is really true. The Doppler effect can be described as a frequency shift on the received signal. The received signal can be written as:

$$y_D(t) = a\sin(2\pi(1 + \frac{2v_z}{c})f_0 t) \tag{4.12}$$

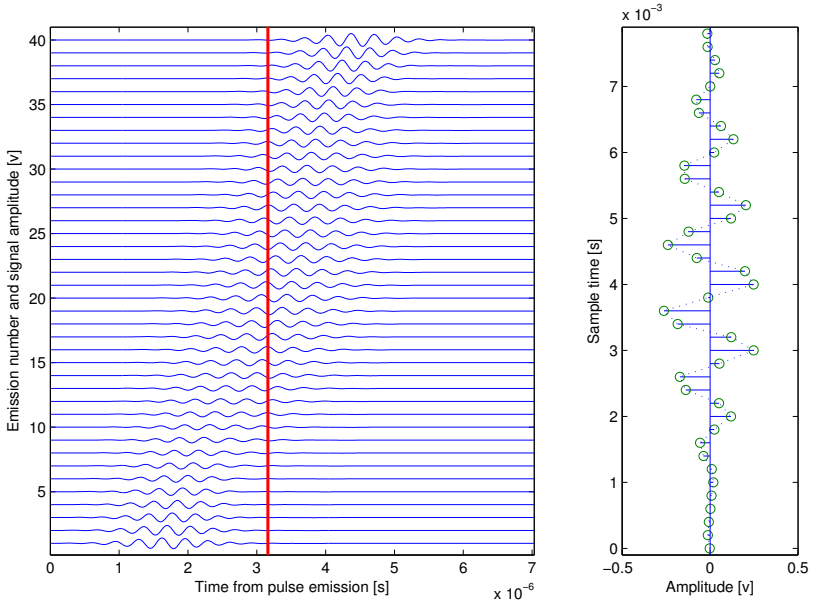

Figure 4.3: Received signals from a single scatterer moving away from the transducer. The solid red line in the left graph indicates the sampling instance for the samples show on the right graph.

for a simple continuous wave source. Here the received frequency is scaled by $(1+2v_z/c)$. There is, thus, a frequency difference of $f_D = \frac{2v_z}{c} f_0$ between the emitted and received signal. This is easy to determine for a continuous wave (CW) source and is used in CW systems, but it is extremely difficult for a pulsed source. Primarily, the shift in frequency is very small, on the order of 1/1000 of the emitted frequency. The shift is therefore minute compared to the bandwidth of the signal, which is roughly $B = f_0/M_p$, M_p being the number of cycles emitted. Secondly, finding this frequency shift assumes that the signal is not affected by other physical effects that shift the mean frequency of the received signal. This is not true in medical ultrasound as the Rayleigh scattering from blood is frequency dependent, and the dispersive attenuation in tissue is quite strong. Even for moderate tissue depths it can span from ten to hundreds of kilohertz of shift in the mean frequency of the received signal, thus, obscuring the Doppler shift [9]. This shift will be different and unknown from patient to patient and would therefore greatly influence the accuracy of the Doppler shift estimation. The Doppler effect is therefore not a reliable estimator of velocity and no pulsed system relies on this effect. Consequently it was not included in the model given in (4.10). Using the time or phase shift between consecutively received signal is a more reliable method, which is not affected much by attenuation, scattering, beam modulation, or non-linear propagation that all affect the received ultrasound signal [9]. The reason for this is that two signals are compared (correlated) and only the difference between two emissions is used in the velocity estimation. This results in a much more reliable system, which does not require an extremely precise frequency content to work. I, therefore, prefer not to call these system Doppler systems as it is confusing to what effect is actually used for the velocity estimation.

4.5 Simulation of flow signals

The model presented above can also be used for simulating the signal from flowing blood. The Field II simulation system [55, 38] uses a model based on spatial impulse responses. The received voltage signal is here described by [6]:

$$v_r(t,\vec{r}_1) = v_{pe}(t) \underset{t}{\star} f_m(\vec{r}_2) \underset{r}{\star} h_{pe}(\vec{r}_1,\vec{r}_2,t), \tag{4.13}$$

where f_m accounts for the scattering by the medium, h_{pe} describes the spatial distribution of the ultrasound field, and v_{pe} is the one-dimensional pulse emanating from the pulse excitation and conversion from voltage to pressure and

back again. $\vec{r}_1$ is the position of the transducer and $\vec{r}_2$ is the position of the scatterers. $\underset{t}{\star}$ and $\underset{r}{\star}$ denote temporal and spatial convolution. This equation describes a summation of the responses from all the point scatterers properly weighted by the ultrasound field strength as described by h_{pe} and convolved with v_{pe}. This yields the signal for a collection of scatterers when the Doppler effect is neglected. For the next emission the scatterer's positions should be propagated as:

$$\vec{r}_2(i+1) = \vec{r}_2(i) + T_{prf}\vec{v}(\vec{r}_2(i), iT_{prf}) \tag{4.14}$$

where $\vec{v}(\vec{r}_2(i), t)$ denotes the velocity vector for this point scatterer for emission i at time $t = iT_{prf}$. Propagating the scatterers and calculating the received signal will then yield a realistic flow signal, which is usable for developing, validating, and evaluating pulsed ultrasound flow systems.

A typical parabolic velocity profile for stationary, laminar flow is:

$$v(r) = \left(1 - \frac{r^2}{R^2}\right) v_0, \tag{4.15}$$

where R is the vessel radius and v_0 is the peak velocity in the vessel. More realistic velocity profiles can be generated by using the Womersley-Evans' description of pulsatile flow [56, 57]. Here a few parameters can be used to describe the full temporal and spatial evolution of the pulsatile flow in *e.g.* the carotid or femoral arteries, and this can readily be included in the simulation. It is also possible to combine this method with computational fluid dynamics using finite element modeling for the flow [58] to capture the formation of turbulence and vortices.

4.6 Estimation of the velocity distribution

The frequency of the flow signals measured is directly proportional to the blood velocity as shown in (4.9). Finding the frequency content of the signal therefore reveals the velocity distribution in the vessel under investigation. This is utilized in spectral estimation systems, which often combine the measurement of velocity with an anatomic B-mode image as shown in Fig. 4.4. The top image shows the anatomy, and the measurement range gate for the flow is indicated by the broken line. The flow measurement is conducted within the vessel, and the "wings" indicate the assumed flow direction. The bottom display shows the velocity distribution as a function of time for five heart beats in the carotid artery.

The velocity distribution changes over the cardiac cycle due to the pulsation of the flow, and the frequency content of the received signal is, thus, not constant. The direction of the flow can also be seen here. For the carotid artery the spectrum is one-sided (only positive frequency components) as the flow is uni-directional towards the brain. It is, thus, important to have processing that can differentiate between velocities towards or away from the transducer. This can be achived by using complex signals with a one sided spectrum. Making a Hilbert transform on the received Radio Frequency (RF) signal and forming the analytic signal [59] then gives

$$r_s(n_x, i) = a g_s(i) \exp(j(2\pi \frac{2v_z}{c} f_0 i T_{prf} - \phi_x)). \tag{4.16}$$

Here the emitted frequency f_0 is scaled by $\frac{2v_z}{c}$, which can be positive or negative depending on the sign of the velocity. Making a Fourier transform of $r_s(n_x, i)$ along the i direction will yield a one-sided spectrum, so that the velocity direction can be determined.

The signal from a vessel consists of a weighted superposition from all the primarily red blood cell scatterers in the vessel. They each flow at slightly different velocities, and calculating the power density spectrum of the signal will give the corresponding velocity distribution of the cells [60, 9]. Displaying the spectrum therefore visualizes the velocity distribution. This has to be shown as a function of time to reveal the dynamic changes in the spectrogram.

Modern ultrasound scanners employ a short time Fourier transform. The complex signal is divided into segments of typically 128 to 256 samples weighted by *e.g.* a von Hann window before Fourier transformation. The process is repeated every 1-5 ms as the spectra are displayed side-by-side as a function of time as shown in Fig. 4.4. Compensating for the beam-to-flow angle then gives a quantitative and real-time display of the velocity distribution at one given position in the vessel.

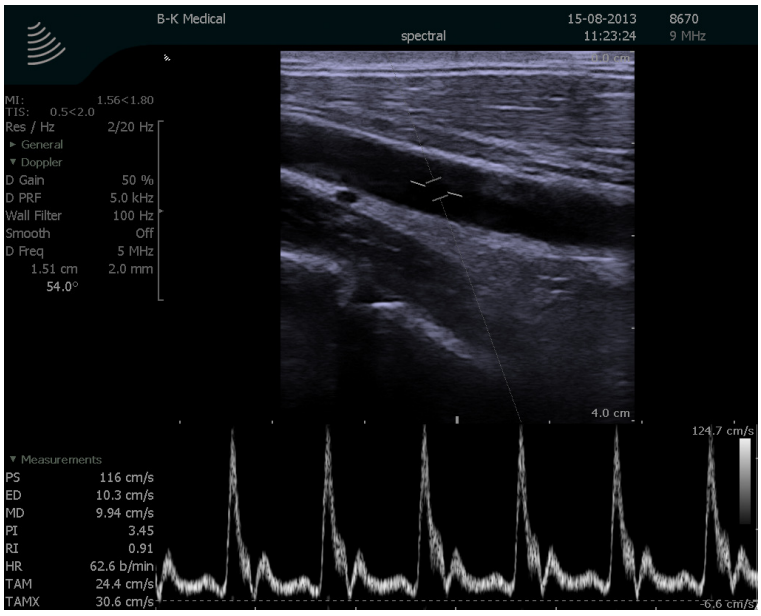

Figure 4.4: Duplex mode ultrasound imaging showing the anatomic B-mode image on the top and the spectral velocity distribution on the bottom (Image courtesy of MD Peter M. Hansen).

The range gate can be selected to be small or large depending on whether the peak velocity or the mean velocity is investigated. The averaging over the range gate can be made either by selecting the length of the emitted pulse or by averaging the spectra across the depth direction by calculating one spectrum for each depth sample n. The spectrogram acquisition method is used clinically when quantitative parameters like peak velocity, mean velocity, or resistive index for the flow must be calculated.

4.7 Axial velocity estimation using the phase

Spectral systems only display the velocity distribution at one single position in the vessel. Often it is preferred to visualize the velocity in a region using the so called Color Flow Mapping (CFM) method. Here data are acquired in a number of directions to construct a real time image of the velocity [61]. The method gives a single value for the velocity at each spatial position, but only a very limited amount of data is available to maintain a reasonable frame rate. Often 8-16 emissions are made in the same direction, and the velocity is found in this direction as a function of depth. The acquisition is then repeated in other directions, and an image of velocity is made and superimposed on the normal B-mode image as shown in Fig. 4.5.

These systems find the velocity from the phase shift between the acquired lines. The complex received signal is in continuous time written as

$$r_t(t) = a g_s(t) \exp(-j(2\pi \frac{2v_z}{c} f_0 t - \phi_x)). \tag{4.17}$$

Taking the derivate of its phase gives

$$\phi' = \frac{d\phi}{dt} = \frac{d(-2\pi \frac{2v_z}{c} f_0 t + \phi_x))}{dt} = -2\pi \frac{2v_z}{c} f_0, \tag{4.18}$$

so that the estimated velocity is

$$\hat{v}_z = -\frac{\phi'}{4\pi f_0} c. \tag{4.19}$$

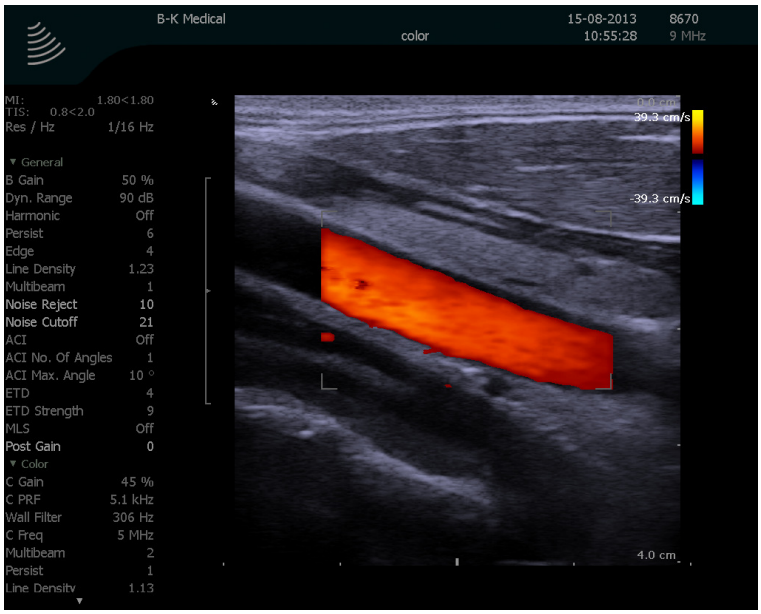

Figure 4.5: CFM image of the carotid artery. The red colors indicate velocity towards the transducer and blue away from the transducer (Image courtesy of MD Peter M. Hansen).

The discrete version can be written as

$$r_s(n_x, i) = a g_s(i) \exp(-j(2\pi \frac{2v_z}{c} f_0 i T_{prf} - \phi_x)) = x(i) + jy(i). \tag{4.20}$$

The phase difference can be found from

$$\begin{aligned} \Delta\phi &= \phi(i+1) - \phi(i) = \arctan \frac{y(i+1)}{x(i+1)} - \arctan \frac{y(i)}{x(i)} \\ &= -(2\pi \frac{2v_z}{c} f_0 (i+1) T_{prf} - \phi_x) + (2\pi \frac{2v_z}{c} f_0 i T_{prf} - \phi_x) \\ &= -2\pi \frac{2v_z}{c} f_0 T_{prf} \end{aligned} \tag{4.21}$$

and the velocity can be estimated from

$$\hat{v}_z = -\frac{\Delta\phi}{4\pi T_{prf} f_0} c = \frac{\Delta\phi}{2\pi} \frac{f_{prf}}{2f_0} c = -\frac{\Delta\phi}{2\pi} \frac{f_{prf}}{2} \lambda = -\frac{\Delta\phi}{4\pi} \frac{\lambda}{T_{prf}}. \tag{4.22}$$

The maximum unique phase difference that can be estimated is $\Delta\phi = \pm\pi$, and the largest unique velocity is therefore $\hat{v}_{z,max} = \frac{\lambda}{4T_{prf}}$. This is determined by the wavelength used and the pulse repetition time or essentially sampling interval. The pulse repetition time of course has to be sufficiently large to cover the full depth and must be larger than $T_{prf} > 2d/c$. Combining the two limitations gives the depth-velocity limitation:

$$\hat{v}_{z,max} < \frac{c}{4} \frac{\lambda}{2d} = \frac{c}{8df_0} c, \tag{4.23}$$

which limits the maximum detectable velocity for a given depth, and is a limitation imposed by the use of a phase estimation system.

The velocity estimation is not performed by taking the phase difference between two measurements, but rather by combing the two arctan operations from:

$$\tan(\Delta\phi) = \tan\left(\arctan\left(\frac{y(i+1)}{x(i+1)}\right) - \arctan\left(\frac{y(i)}{x(i)}\right)\right)$$

$$= \frac{\frac{y(i+1)}{x(i+1)} - \frac{y(i)}{x(i)}}{1 + \frac{y(i+1)}{x(i+1)}\frac{y(i)}{x(i)}}$$
$$= \frac{y(i+)x(i) - y(i)x(i+1)}{x(i+1)x(i) + y(i+1)y(i)} \tag{4.24}$$

using that

$$\tan(A-B) = \frac{\tan(A) - \tan(B)}{1 + \tan(A)\tan(B)}. \tag{4.25}$$

Then

$$\arctan\left(\frac{y(i+1)x(i) - y(i)x(i+1)}{x(i+1)x(i) + y(i+1)y(i)}\right) = -2\pi f_0 \frac{2v_z}{c} T_{prf} \tag{4.26}$$

or

$$\hat{v}_z = -c\frac{f_{prf}}{4\pi f_0} \arctan\left(\frac{y(i+1)x(i) - y(i)x(i+1)}{x(i+1)x(i) + y(i+1)y(i)}\right). \tag{4.27}$$

This simple algebraic equation directly yields the velocity from comparing two emissions. Often the signal-to-noise ratio from blood signals is low due to the weak scattering from blood, and therefore it is advantageous to average over a number of emissions as

$$\hat{v}_z = -c\frac{f_{prf}}{4\pi f_0} \arctan\left(\frac{\sum_{i=1}^{M} y(i+1)x(i) - y(i)x(i+1)}{\sum_{i=1}^{M} x(i+1)x(i) + y(i+1)y(i)}\right), \tag{4.28}$$

where M is the number of emissions. This can also be calculated as the phase of the lag one autocorrelation of the received signal [61]. Further averaging can be made along the depth direction as the data is highly correlated over a pulse length. This is calculated as [62]:

$$\hat{v}_z(N_x) = -c\frac{f_{prf}}{4\pi f_0} \arctan\left(\frac{\sum_{i=1}^{M}\sum_{n=-N_p/2}^{N_p/2} y(n+N_x, i+1)x(n+N_x, i) - y(n+N_x, i)x(n+N_x, i+1)}{\sum_{i=1}^{M}\sum_{n=-N_p/2}^{N_p/2} x(n+N_x, i+1)x(n+N_x, i) + y(n+N_x, i+1)y(n+N_x, i)}\right) \tag{4.29}$$

when the real part of received data is given as $x(n,i)$ and $y(n,i)$ is the imaginary part. Here n is the time index (depth) and i is the pulse emission number. N_x is the starting sample for the depth to estimate the velocity. N_p is the number of RF samples to average over and typically corresponds to one pulse length. This is the approach suggested by Loupas et al. [62] and is the one used in nearly all modern scanners.

4.7.1 Stationary echo canceling

At vessel boundaries the received signal consists of both reflections from the vessel boundary and the scattered signal from blood. Often the reflection signal is 20 to 40 dB larger in amplitude compared with the signal from blood, and it therefore makes velocity estimation heavily biased or impossible. The reflection signal is often assumed to be stationary and thereby constant over the number of pulse emissions. Subtracting two consecutive signals will therefore remove the stationary component and leave a signal suitable for velocity estimation:

$$r_{es}(n,i) = r_s(n,i) - r_s(n,i+1) \tag{4.30}$$

For a fully stationary signal this will give zero whereas the flow signal will be filtered depending on the correlation between the two emissions. This filtration on the flow part $r_f(n,i)$ of the signal can be calculated from

$$r_e(n,i) = r_f(n,i) - r_f(n,i+1) = r_f(n,i) - r_f(n,i)\exp(j2\pi\frac{2v_z}{c}f_0 T_{prf}), \tag{4.31}$$

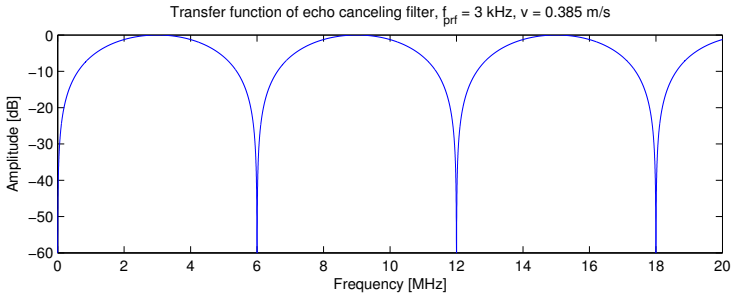

Figure 4.6: Transfer function of echo canceling filter.

assuming that the signals are so highly correlated that the shift in position due to the flow can be described by a simple phase shift. In the Fourier domain this gives

$$R_e(f) = R_f(f)(1 - \exp(j2\pi \frac{2v_z}{c} f T_{prf})), \tag{4.32}$$

where the Fourier transform is taken along the emissions (i). The transfer function of the filter is therefore

$$H(f) = (1 - \exp(j2\pi \frac{2v_z}{c} f T_{prf})) = 2j \sin(\pi \frac{2v_z}{c} T_{prf} f). \tag{4.33}$$

The transfer function of this filter is shown in Fig. 4.6 for $v_z = 0.385$ m/s and $f_{prf} = 3$ kHz. It can be seen that the filter reduces the energy of the RF signal significantly around a band of 6 MHz and at low frequencies. It is an unavoidable side-effect of echo canceling filtration that the energy of the flow signal is reduced and the signal-to-noise ratio is therefore reduced. The effect is especially noticeable at low flow velocities. Here the second signal is very similar to the first measurement since the time shift $t_s = 2v_z/cT_{prf}$ is small. The subtraction therefore removes most of the energy and the noise power in the two measurements are added.

The reduction in signal-to-noise ratio due to the stationary echo canceling can be analytically calculated for a Gaussian pulse and is [9, 63]:

$$\begin{aligned} R_{\text{snr}} &= \sqrt{\frac{2\sqrt{2} + \exp(-\frac{2}{B_r^2})}{2\sqrt{2} + \exp(-\frac{2}{B_r^2})\xi_1 - 2\sqrt{2}\xi_2 \cos(2\pi \frac{f_0}{f_{sh}})}} \\ \xi_1 &= 1 - \exp\left(-\frac{1}{2}\left(\frac{\pi B_r f_0}{f_{sh}}\right)^2\right) \\ \xi_2 &= \exp\left(-\left(\frac{\pi B_r f_0}{f_{sh}}\right)^2\right) \\ f_{sh} &= \frac{c}{2v_z} f_{prf}, \end{aligned} \tag{4.34}$$

where the pulse is given by

$$p(t) = \exp(-2(B_r f_0 \pi)^2 t^2) \cos(2\pi f_0 t). \tag{4.35}$$

Here B_r is the relative bandwidth and f_0 is the center frequency. The reduction for $f_0 = 3$ MHz, $f_{prf} = 3$ kHz and $B_r = 0.08$ is shown in Fig. 4.7. At zero velocity the decrease is infinite as the two signals are identical and no velocity can be found. The reduction decreases progressively for increasing velocity and a gain in SNR is found at the maximum detectable velocity. Here the two signals are inverted compared to each other and the subtraction then yields an addition of the two. The amplitude is therefore doubled and the noise power is doubled, hence giving an improvement of 3 dB in SNR. The curve in Fig. 4.7 is dependent on the echo canceling filter used and on the pulse emitted $p(t)$, but there will also be an infinite loss at zero velocity.

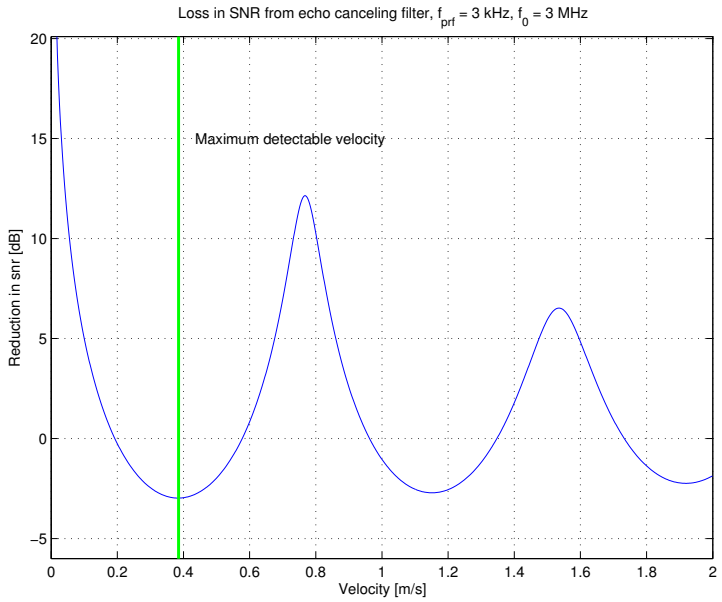

Figure 4.7: Loss in signal-to-noise ratio due to the echo canceling filter.

Another method is to subtract the mean value of all the received lines as

$$r_e(n,i) = r_s(n,i) - \frac{1}{M}\sum_{k=1}^{M} r_s(n,k). \tag{4.36}$$

This gives a sharper cut-off in transfer function of the filter and less noise added to the response.

Many different echo canceling filters have been suggested [64, 65], but it still remains a very challenging part of velocity estimation and probably the one factor most affecting the outcome of the estimation.

4.8 Axial velocity estimation using the time shift

It is also possible to estimate the velocity directly from the time shift between the signals. Two consecutive signals are related by:

$$y_c(t,i+1) = y_c(t - \frac{2v_z}{c}T_{prf}, i) = y_c(t - t_s, i) \tag{4.37}$$

Cross-correlating two consecutive signals can then be used for finding the time shift and, hence, the velocity. This is calculated by [54, 53]:

$$R_{12}(\tau,i) = \int_T y_c(t,i)y_c(t+\tau,i+1)dt = \int_T y_c(t,i)y_c(t-t_s+\tau,i)dt = R_{11}(\tau - t_s) \tag{4.38}$$

Using (4.2) the autocorrelation can be rewritten as

$$\begin{aligned} R_{11}(\tau - t_s, i) &= \int_T p(t) * s(t,i)p(t) * s(t - t_s + \tau, i)dt = R_{pp}(\tau) * \int_T s(t,i)s(t - t_s + \tau, i)dt \\ &= R_{pp}(\tau)P_s\delta(\tau - t_s) = P_s R_{pp}(\tau - t_s), \end{aligned} \tag{4.39}$$

where P_s is the scattering power, and the scattering signal is assumed to be random and white. $R_{pp}(\tau)$ is the autocorrelation of the emitted pulse, and this has a unique maximum value at $\tau = 0$. $R_{pp}(\tau - t_s)$ therefore has a unique

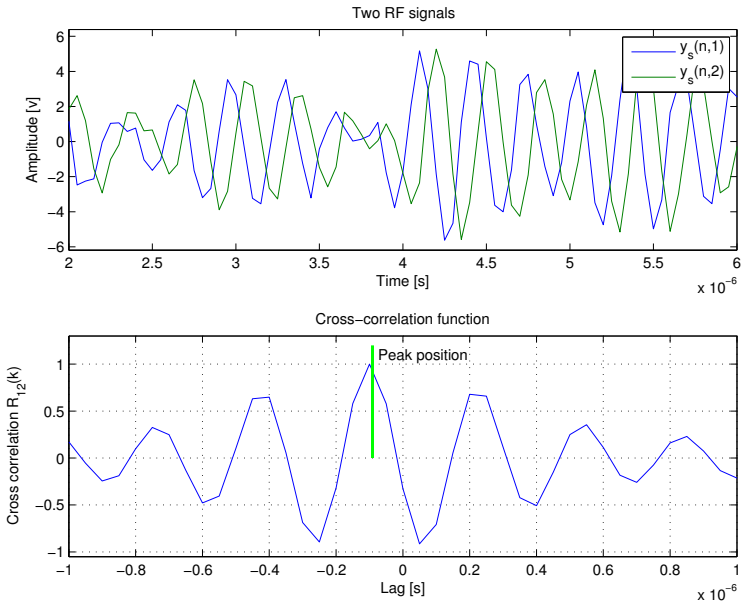

Figure 4.8: Illustration of the cross-correlation. The top graph shows the two signals to be correlated and the bottom graph shows their cross-correlation.

maximum at $\tau = t_s$, and the velocity can be found from

$$\hat{v}_z = c\frac{\hat{t}_s}{2T_{prf}}. \tag{4.40}$$

The cross-correlation is calculated from the discrete sampled signals $y_s(n,i)$ as

$$R_{12d}(k,N_x) = \sum_{i=1}^{N_e-1}\sum_{n=-N_n/2}^{N_n/2} y_s(n+N_x,i)y_s(n+k+N_x,i+1) \tag{4.41}$$

where N_e is the number of emissions to average over, N_n is the number of samples to average over, and N_x is the sample number (depth) at which to find the velocity at. The position of the peak n_s in $R_{12}(k,N_x)$ is then found at the velocity calculated from

$$\hat{v}_z = c\frac{\hat{n}_s/f_s}{2T_{prf}}, \tag{4.42}$$

where f_s is the RF sampling frequency.

The cross-correlation function is shown in Fig. 4.8. The upper graph shows the two signals used where the time shift readily can be seen. The lower graph shows the cross-correlation of the signals along with an indication of the peak position. A 3 MHz Gaussian pulse was used in the simulation along with $f_{prf} = 5$ kHz and a 20 MHz sampling frequency. The velocity was 0.35 m/s, which gave a time shift of $t_s = 0.156$ μs.

The time shift is usually comparable the sampling interval $1/f_s$, and the velocity estimates will be heavily quantized. This can be solved by fitting a second-order polynomial around the cross-correlation peak and then finding the peak value of the polynomial. The interpolation is calculated by [66]:

$$n_{int} = n_s - \frac{\hat{R}_{12d}(n_s+1) - \hat{R}_{12d}(n_s-1)}{2(\hat{R}_{12d}(n_s+1) - 2\hat{R}_{12d}(n_s) + \hat{R}_{12d}(n_s-1))} \tag{4.43}$$

and the interpolated estimate is given by

$$\hat{v}_{int} = \frac{c}{2}\frac{n_{int}f_{prf}}{f_s}. \tag{4.44}$$

This gives an increased resolution, if the cross-correlation estimate is sufficiently noise-free.

Several factors affect how well this estimator works. A short pulse should be used for the emission to provide the narrowest possible cross-correlation function. The averaging should by performed over a sufficient number of samples to give a good estimate, but should also be limited to a region where the velocity can be assumed to be constant in space. Also, the number of emissions averaged over time should be sufficient to ensure a good result without lowering the frame rate too much.

The cross-correlation method can find velocities higher than the autocorrelation approach as it is not restricted to a phase shift of $\pm\pi$. In theory any kind of velocity can be found, but this can lead to false peak detection [67]. Here a global maximum in the correlation function beyond the correct peak is found. As the cross-correlation is determined by the autocorrelation of the pulse, these erroneous peak will reside at $k/f_0 + n_s$, leading to a large error in the estimated velocity. This can be difficult to correct and gives spike artifacts in the image display. Often the search range for finding the maximum is therefore limited to lie around zero velocity. No false peaks arise if the search range is limited to $-f_s/(2f_0) < k < f_s/(2f_0)$ which gives the same maximum velocity as the autocorrelation or phase shift approach.

It is difficult to decide which of the two methods are best. Often the cross-correlation gives better accuracies on the estimates, but this is off-set by its lower sensitivty, which comes from using a shorter pulse. In general the decision is dependent on the actual measurement situation and setup.

4.9 Two-dimensional vector velocity estimation

The methods described so far only find the velocity along the ultrasound beam direction, and this is often perpendicular to the flow direction. The velocity component found is therefore often the smallest and least important. Many angle compensation schemes have been devised [68, 69] but they all rely on the assumption that a single angle applied for the whole cardiac cycle and region of interest, which in general is not correct. Due to the pulsating nature of the flow, the velocity will often be in all directions and changes both magnitude and direction over the cardiac cycle. There is, thus, a real need for vector velocity estimation methods.

The problem has been acknowledged for many years, and a number of authors have suggested schemes for finding the velocity vector. Fox [70] used two crossing beams to find the velocity for two directions and then combine it to yield the 2-D velocity vector. Newhouse et al. [71] suggested using the bandwidth of the received signal to determine the lateral component. Trahey et al. [72] used a speckle tracking approach for searching for the velocity vector.

Currently the only method that has been introduced on commercial FDA approved scanners is the Transverse Oscillation (TO) approach developed by Jensen and Munk [73, 74]. A similar approach was also suggested by [75].

The traditional axial velocity estimation methods rely on the axial oscillation to find the velocity. The TO method introduces an oscillation transverse to the ultrasound propagation direction to make the received signals sensitive to a transverse motion. Such a transverse field is shown in Fig. 4.9. The figure shows a contour plot of the linear point spread function (PSF), and oscillations can be seen both in the lateral and axial direction. Two fields are needed to make a complex field with an in-phase and quadrature component that can be used for finding the sign of the velocity in the lateral direction.

The lateral oscillation is generated by utilizing a special apodization on the transducer during receive processing. At the focus there is a Fourier relation between the transducer's apodization function and the ultrasound field [76]. To generate a sinusoidal oscillation, the receive apodization should ideally, derived for a continuous field, consist of two sinc shaped peaks with a distance of D. This will give a lateral wavelength of:

$$\lambda_x = \lambda \frac{2D}{P_d}, \tag{4.45}$$

where P_d is the depth in tissue. Sending out a fairly broad beam and focusing the two fields in receive with this apodization function will yield the fields shown in Fig. 4.9. The signals at the dashed line are shown in Fig. 4.10,

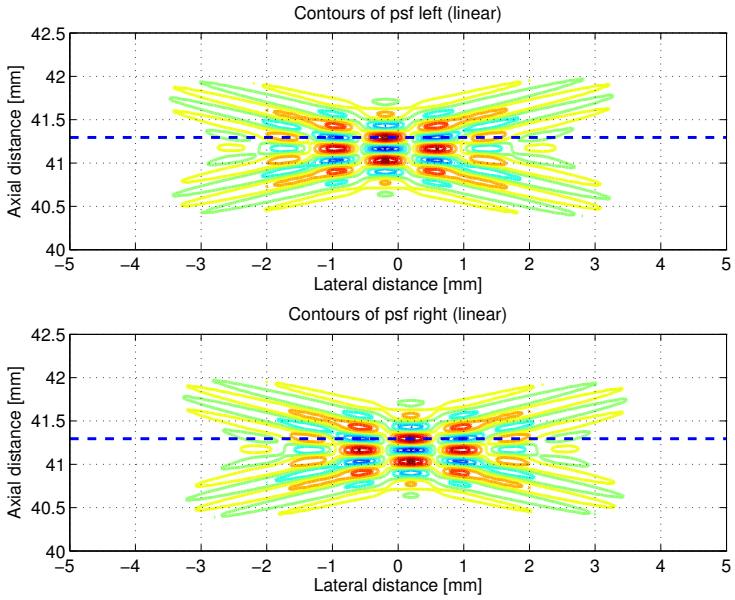

Figure 4.9: Ultrasound fields employed in TO velocity estimation. The top graph shows the left field and the bottom the right field.

where the blue curve is from the left field and the dashed green curve is from the right field. These two signals should ideally be 90° phase shifted compared to each other to generate a one-side spectrum. For a pulsed field (4.45) is not accurate enough to ensure this and computer optimization has been made to adjust the focusing to give the best possible result [77]. This has been done for a convex array probe by minimizing the amplitude spectrum of the complex field for negative spatial frequencies as shown in the lower graph in Fig. 4.10. This ensures a nearly one sided spectrum and thereby the best possible estimate in terms of bias and standard deviation.

The receive beamforming yields signals usable for the vector velocity estimation. They are combined into the complex signal $r_{sq}(i)$ and a temporal Hilbert transform of this gives the signal $r_{sqh}(i)$. From these two new signals are made:

$$\begin{aligned} r_1(i) &= r_{sq}(i) + jr_{sqh}(i) \\ r_2(i) &= r_{sq}(i) - jr_{sqh}(i). \end{aligned} \tag{4.46}$$

The velocity components are then estimated by the TO estimators derived in [74]. They are given by:

$$v_x = \frac{\lambda_x}{2\pi 2T_{prf}} \arctan\left(\frac{\Im\{R_1(1)\}\Re\{R_2(1)\} + \Im\{R_2(1)\}\Re\{R_1(1)\}}{\Re\{R_1(1)\}\Re\{R_2(1)\} - \Im\{R_1(1)\}\Im\{R_2(1)\}}\right) \tag{4.47}$$

and

$$v_z = \frac{c}{2\pi 4T_{prf} f_0} \arctan\left(\frac{\Im\{R_1(1)\}\Re\{R_2(1)\} - \Im\{R_2(1)\}\Re\{R_1(1)\}}{\Re\{R_1(1)\}\Re\{R_2(1)\} + \Im\{R_1(1)\}\Im\{R_2(1)\}}\right). \tag{4.48}$$

where $R_1(1)$ is the complex lag one autocorrelation value for $r_1(i)$, and $R_2(1)$ is the complex lag one autocorrelation value for $r_2(i)$.$\Im$ denotes imaginary par and $\Re$ the real part. These give the velocity vector in the imaging plane.

Fig. 4.11 shows a vector flow image (VFI) of the carotid bifurcation measured by a linear array probe and the TO approach. The image is acquired right after peak systole. The vectors show magnitude and direction of the flow, while the color intensities show velocity magnitude. A vortex can be seen in the carotid bulb. The vortex appears right after peak systole and disappears in roughly 100 ms. This is a normal flow pattern in humans and shows the value of vector flow imaging. It is important to note that there is no single correct beam-to-flow angle in this image. Both magnitude and direction change rapidly as a function of both time and space, making it essential to have a vector flow estimation system to capture the full complexity of the hemodynamics.

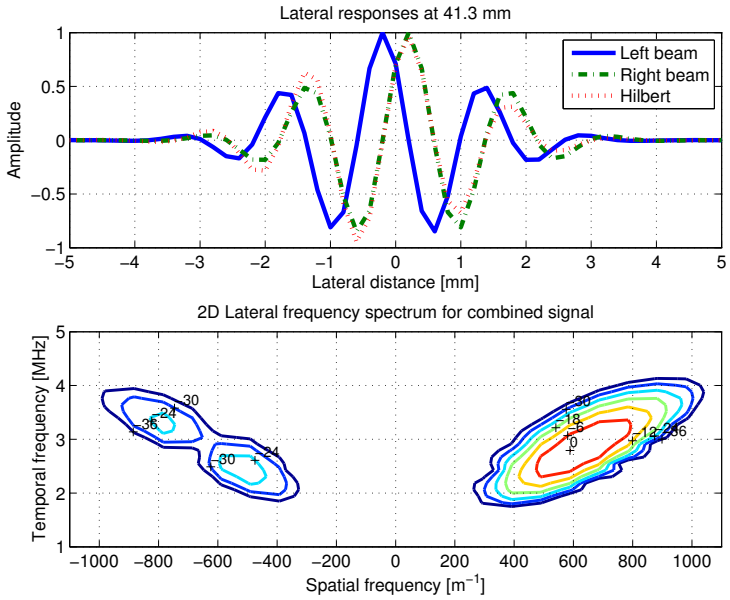

Figure 4.10: Lateral left and right responses in the TO fields at the maximum compared to the Hilbert transform of the left field. The bottom graph shows the 2-D Fourier transform of the complex TO psf.

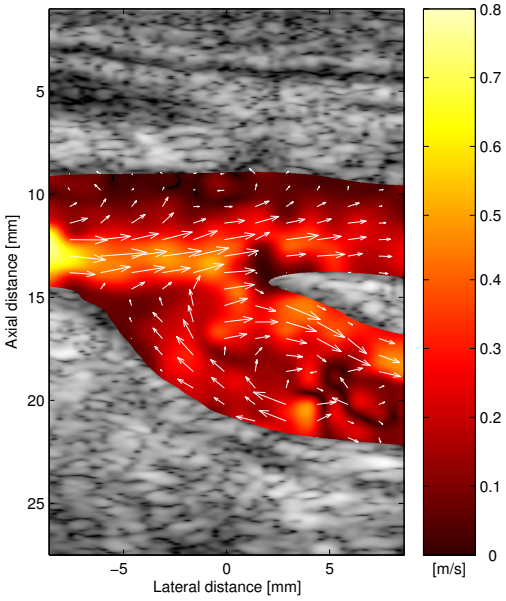

Figure 4.11: Vector flow image of the carotid bifurcation right after peak systole, where a vortex is present in the carotid bulb (from [78]).

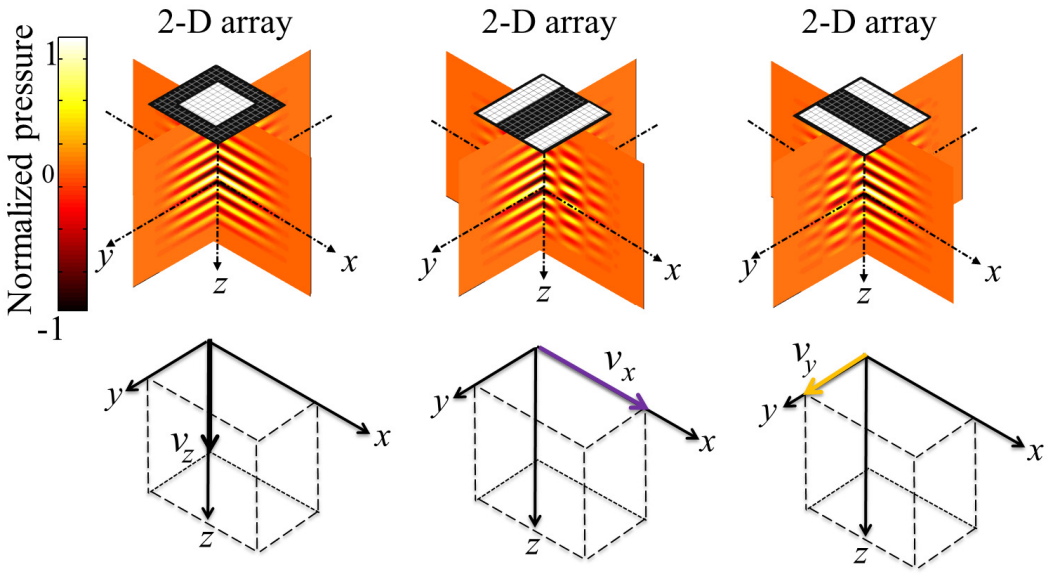

Figure 4.12: Receive apodization profiles applied to generate the TO fields for all three velocity components. The white shaded areas indicate the active elements in the 32 x 32 array (from [79]).

4.10 Three-dimensional vector velocity estimation

The TO approach can also be extended to full three-dimensional imaging by using a 2-D matrix transducer. Here 5 lines are beamformed in parallel during the receive processing to get a set of lines for the transverse, elevation, and axial velocity components. The beamforming is visualized in Fig. 4.12, where the active elements used in the beamformation are shaded white and the corresponding velocity direction is indicated below the array. Slices into the corresponding ultrasound fields are also shown below the transducer, and the oscillations in the axial, transverse, and elevation planes can be seen.

The approach has been implemented on the SARUS experimental ultrasound scanner [80] connected to a Vermon 32 x 32 3MHz matrix array transducer [81, 82, 79]. Parabolic flow in a recirculating flow rig was measured, and the result is shown in Fig. 4.13. The flow is in the elevation direction (out of the imaging plane) of the image shown in the bottom, and both 1-D and 2-D velocity estimation systems would show no velocity. The arrows indicate the out-of-plane motion amplitude and direction and show the parabolic velocity profile.

The approach has also been used *in-vivo* as shown in Fig. 4.14 for the carotid artery. Two intersecting B-mode images have been acquired, and the 3-D velocity vectors have been found at the intersection of the two planes. The estimated velocity magnitude as a function of time is shown in the lower graph, and the velocity vector is shown around the peak systole in the cardiac cycle. This method has the potential of showing the full dynamics of the complex flow in the human circulation in real time for a complete evaluation of the hemodynamics.

4.11 Synthetic aperture and plane wave flow estimation

The measurements systems described so far are all sequential in nature. They acquire the flow lines in one direction at a time, and this makes the measurement slow, especially when images consist of many directions or many emissions have to be used for flow estimation. Triplex imaging shows both the B-mode, CFM image, and spectral information simultaneously and therefore needs to split the acquisition time between the three modes. This often makes the resulting frame rate unacceptable low for clinical use for large depths. This will also be a very limiting factor for 3-D

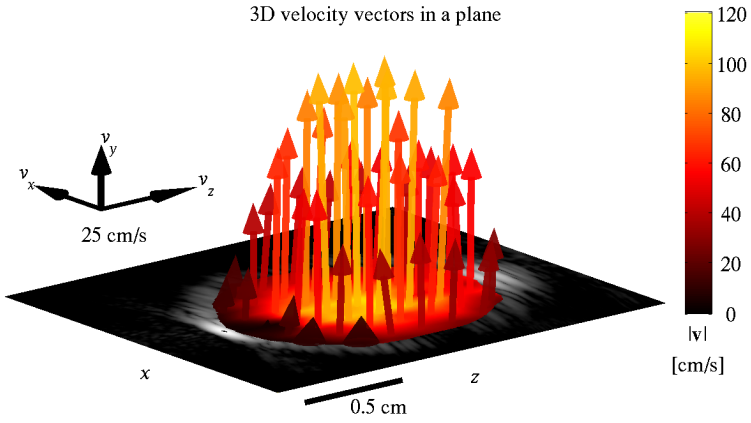

Figure 4.13: 3D vector velocity image for a parabolic, stationary flow(from [79]).

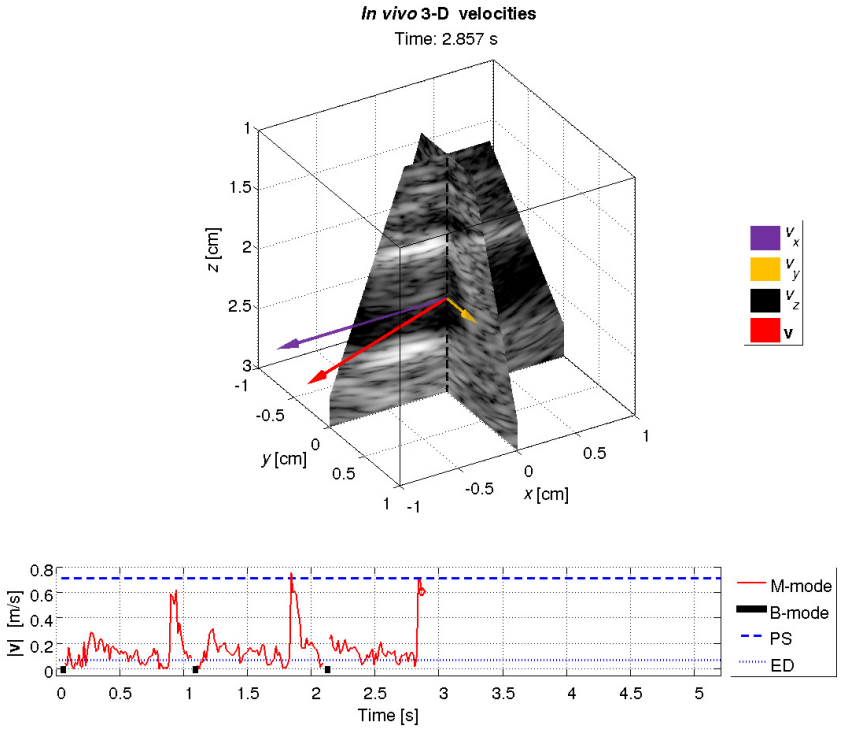

Figure 4.14: In-vivo 3-D vector velocity image taken around peak systole in the carotid artery of a healthy volunteer (Courtesy of Dr. Michael Johannes Pihl).

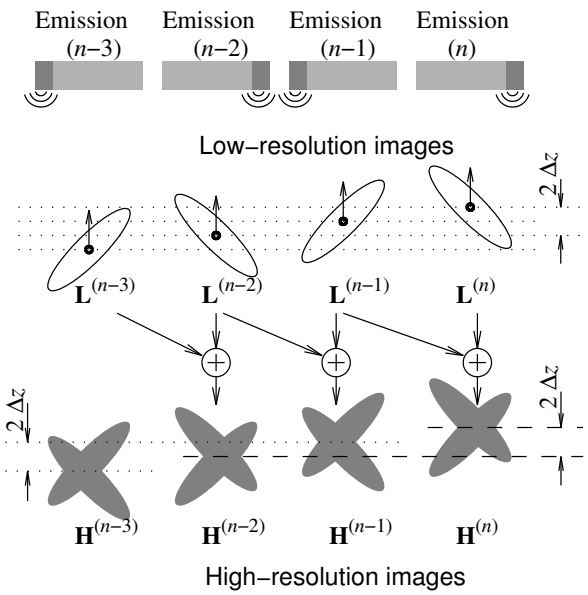

Figure 4.15: Acquisition of SA flow data and beamforming of high resolution images (from [93]).

flow imaging, which often has to resort to ECG gating when acquiring full volumes. Another drawback of traditional imaging is the use of transmit focusing. This cannot be made dynamic, and the images are only optimally focused at one single depth.

These problems can be solved by employing new imaging schemes based on synthetic aperture (SA) imaging [83, 84, 4, 85, 86, 87, 88, 89] and plane wave imaging [90, 91, 92]. Both these techniques insonify the whole region to interrogate and reconstruct the images during receive beamforming. This potentially can lead to very fast imaging and can also be used for flow imaging with very significant advantages.

The SA method is shown in Fig. 4.15. The transducer on the top emits a spherical wave, and the scattered signal is then received on all elements of the transducer. This process is repeated for a number of emission sources N_l on the aperture, and the data are collected for all receiving elements. From the received data for a single emission, a full low resolution (LR) image can be made. It is only focused in receive, but combining all the LR images yields a high resolution (HR) image. This is also focused during transmit as all the emitted fields are summed in phase [94]. The approach gives better focused images than traditional beamforming [95] with at least a preserved penetration depth when coded excitation is used.

The imaging scheme can also be used for flow estimation, although the data are acquired over a number of emissions, and therefore are shifted relative to each other. This is also illustrated in Fig. 4.15 for a short sequence. The point spread function for the low resolution images are shown below for a point scatterer moving towards the transducer. The LR point spread functions (PSFs) are different for the different emissions and can therefore not be directly correlated to find the velocity. Adding the low resolution images gives the PSF for the HR images, and it can be seen that these have the same shape, when the emission sequence combined is the same apart from the motion in position. The basic idea is therefore only to correlate the HR PSFs with the same emission sequence for finding the flow. This can also be performed recursively, so that a new correlation function is made for every new LR image [89].

The approach is illustrated in Fig. 4.16. The HR signals in one direction is shown on the top divided into segments. The length of the emission sequence is N_l and therefore emission n and $n + N_l$ can be correlated. This can then be averaged with $n + 1$ correlated with $n + 1 + N_l$ as the time shift t_s is the same. It is therefore possible to continuously average the correlation function, and therefore use all data to get a very precise estimate of the correlation and thereby the velocity. This can be performed for all directions in the HR image continuously.

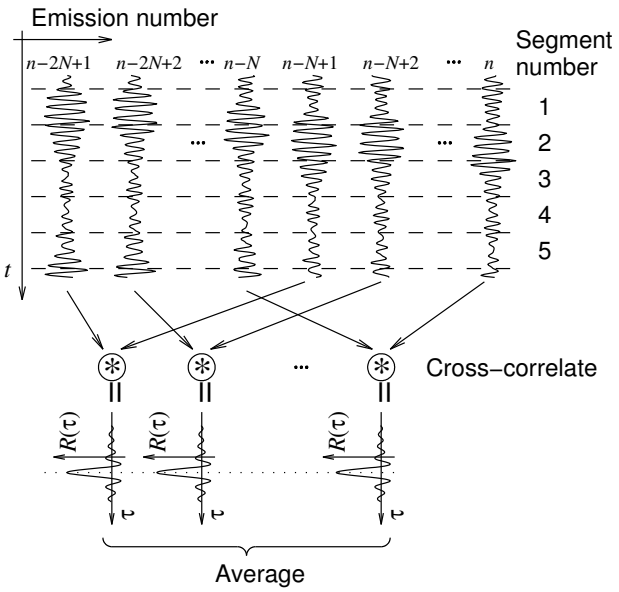

Figure 4.16: Averaging of cross-correlation functions in SA flow imaging (from [93]).

This has a number of advantages. The data can be acquired continuously, and data for flow imaging is, therefore, continuously available everywhere in the image. This makes it possible to average over very large amounts of data and makes echo canceling much easier [93]. Initialization effects for the filter can be neglected as the data are continuous, and this makes a large difference for *e.g.* low velocity flow. The cut-off frequency of the traditional echo canceling filter is proportional to f_{prf}/M where M here can be made arbitrarily large. The correlation estimates can also be averaged over a larger time interval T_i. The length N_h is only limited by the acceleration a_f of the flow. For a cross-correlation system there should at most be $\frac{1}{2}$ sampling interval shift due to acceleration:

$$a_f N_l T_{prf} N_h < \frac{1}{2 f_s T_{prf}} \frac{c}{2} \tag{4.49}$$

or

$$T_i = N_l T_{prf} N_h < \frac{f_{prf}}{2 f_s} \frac{c}{2 a_f} \tag{4.50}$$

to avoid de-correlation in the estimate of the cross-correlation function.

The data can also be focused in any direction as complete data sets are acquired, and the position of both the emitting sources and the receivers are known. The signals for velocity estimation can therefore be focused along the flow lines, if the beam-to-flow angle is known. This focusing scheme is shown in Fig.4.17. For each depth the data are focused along the flow and then used in a cross-correlation scheme to find the velocity [96, 97].

The estimated profiles for such a scheme are shown in Fig. 4.18 at a beam-to-flow angle of 60°. A linear array was used with an 8 emission SA sequence using a chirp pulse. Data from 64 elements were acquired for each emission, and 16 sequences, for a total of 128 emission, were averaged. All the 20 estimated velocity profiles are shown on the top and the mean $\pm$ 3 std are shown on the bottom. The mean relative standard deviation was 0.36% [96]. The approach also works for fully transverse flow and can yield a fast and quantitative display of the vector velocity.

It is also possible to determine the angle from the data. Here the directional lines are beamformed in all directions, and the one with the highest relative correlation indicates the angle [98]. An example of an in-vivo SA vector flow image from the carotid artery is shown in Fig. 4.19, where both velocities and angles have been estimated.

The data can also be used for visualizing the location of flow. This is done by finding the energy of the signals after echo canceling in a B-flow system [99] or power Doppler mode and show this. The intensity of the signal is then

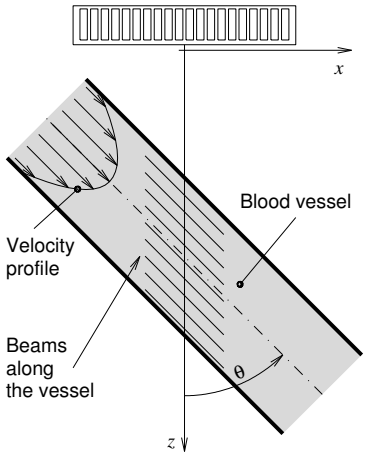

Figure 4.17: Directional beamforming along the flow lines (from [96]).

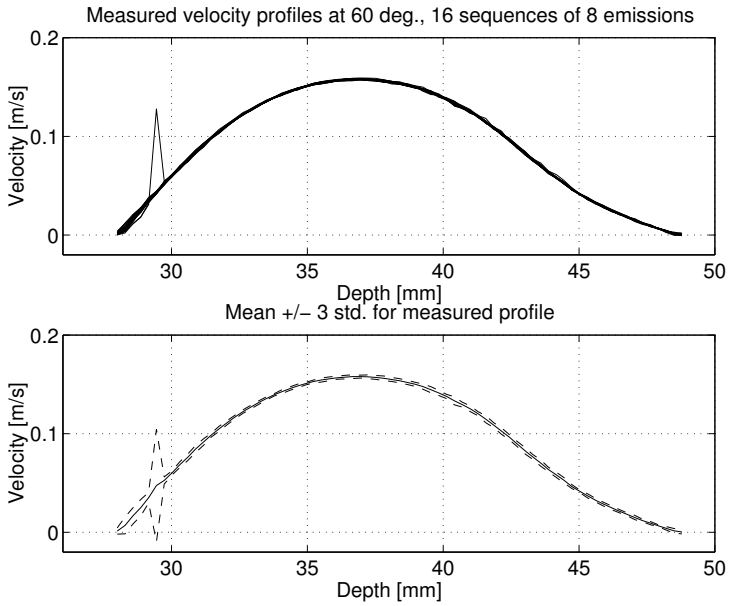

Figure 4.18: Estimated velocity profiles (top) at a beam-to-flow angle of 60°and mean value $\pm$ 3 standard deviations for SA vector flow imaging (from [96]).

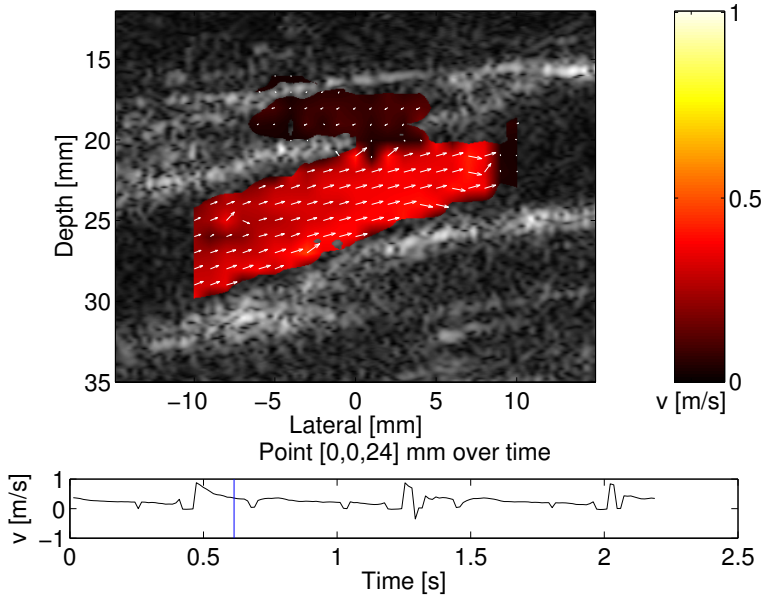

Figure 4.19: In-vivo SA vector flow imaging from the carotid artery (from [98])

roughly proportional to the velocity. An example of a SA B-flow image is shown in Fig. 4.20 at two different time instances in the cardiac cycle.

Another method for making fast and continuous imaging is to utilize plane wave emission. Here the full transducer is employed to transmit a plane wave, and then data are acquired for all the receiving elements [90]. The full image can then be reconstructed as for SA imaging. The image is only focused during receive and will have a lower resolution and higher side-lobes than conventional images. This can be compensated by using a number of plane waves at different angles as illustrated in Fig. 4.21. Combining these with a proper apodization can then lead to a full HR image [101]. This imaging scheme has the same advantages as SA imaging with a continuous data stream that can be used for increasing the sensitivity of flow estimation.

These imaging schemes can also be made very fast, and this is beneficial for looking at transitory and very fast flow phenomena, which are abundant in the human circulation [102, 103]. An plane wave vector flow image is shown in Fig. 4.22. A single plane wave was continuously emitted and the full image was beamformed for each emission. This was used in a speckle tracking scheme to find the velocity vectors and resulted in 100 independent vector velocity images per second [104]. A valve in the jugular vein and the carotid artery were imaged. The left image shows the open valve on the top, where a clockwise vortex is found behind the valve leaflets. The valve is incompetent and does not close correctly as shown in the right graph, where a noticeable reverse flow is seen. The vortex behind the leaflet has also changed direction. The middle image shows secondary rotational flow in the carotid artery during peak systole indicating the importance of having a full three-dimensional flow system.

SA and plane wave flow imaging is excellent for observing slow moving flow due to the long observation time possible. This has been demonstrated in [105, 101], which used plane wave imaging for mapping the brain function of a rat. The new acquisition methods can, thus, obtain data suitable for both fast vector velocity imaging and slow flow estimation for functional ultrasound imaging.

4.12 Motion estimation and other uses

The methods described can in general also be used for motion estimation. Tissue motion can be found by leaving out the echo canceling filter, and then all the methods can be applied for strain imaging [106], radiation force imaging

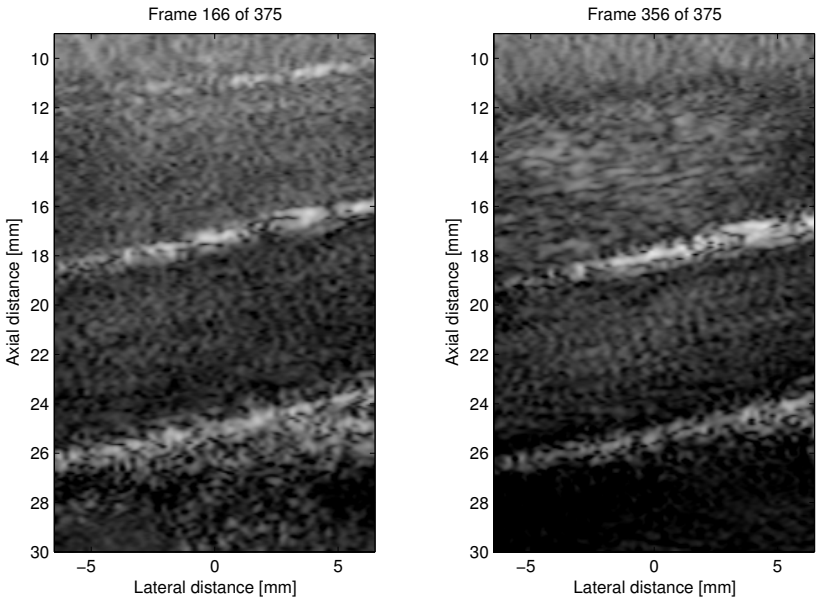

Figure 4.20: SA B-flow image of jugular vein and carotid artery (from [100]).

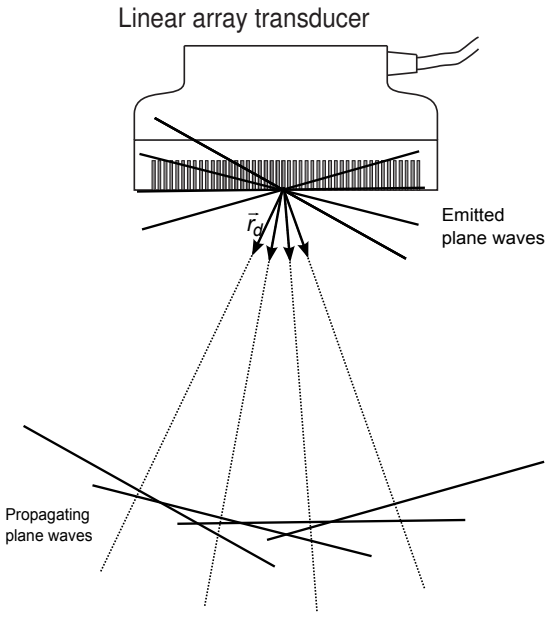

Figure 4.21: Plane wave imaging.

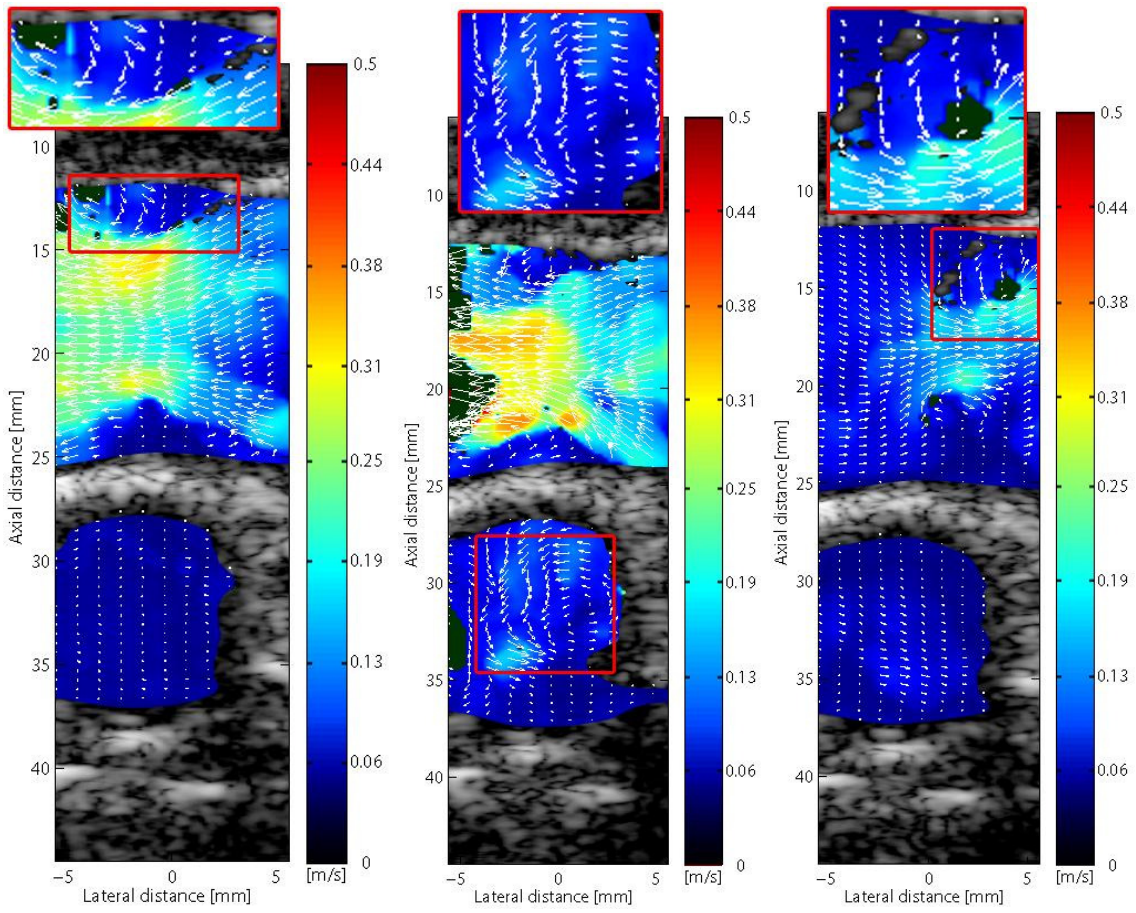

Figure 4.22: In-vivo plane wave vector flow images acquired at a frame rate of 100 Hz. The left image shows flow through a valve in the jugular vein at peak systole. The right image shows reverse flow during diastole. Note how the vortices behind the valve leaflet change rotation direction. Secondary flow is also seen in the middle image in the carotid artery below the jugular vein. (from [104]).

[107, 108], shear wave imaging [90], tissue Doppler [109] and others methods relying on the detection of motion or velocity. In general the methods have an improved performance for tissue, due to the increased signal-to-noise ratio and the lack of the echo canceling filter. It is therefore possible to calculate the derivatives necessary for some of these methods.

The velocity estimates are also used in deriving quantitative numbers useful for diagnostic purposes. Especially the new vector velocity estimates can be used for making the diagnosis more quantitative by calculating *e.g.* the volume flow [110], deriving quantities for indicating turbulence [111], and finding mean or peak velocities. It is also possible to use the vector velocity data for calculating flow gradients by solving the Navier-Stokes equations [112].

The development within velocity estimation is by no means complete. The combination of SA and plane wave imaging with 2-D and 3-D vector velocity and functional imaging is still a very active research area, and more complete information about the complex flow in the human body can be obtained. It will in real time reveal the many places for transient turbulences, vortices, and other multi-directional flow, and it will become possible to derive many more quantitative parameters for characterizing the patient's circulation.

CHAPTER

FIVE

Synthetic aperture ultrasound imaging

Taken from the paper:

Jørgen Arendt Jensen, Svetoslav Ivanov Nikolov, Kim Løkke Gammelmark and Morten Høgholm Pedersen

Synthetic aperture ultrasound imaging

Ultrasonics, Vol. 44, 2006, p. e5-e15.

Available online at www.sciencedirect.com
ScienceDirect
Ultrasonics 44 (2006) e5–e15
Ultrasonics
www.elsevier.com/locate/ultras

Synthetic aperture ultrasound imaging

Jørgen Arendt Jensen *, Svetoslav Ivanov Nikolov, Kim Løkke Gammelmark, Morten Høgholm Pedersen

Center for Fast Ultrasound Imaging, Ørsted•DTU, Building 348, Technical University of Denmark, DK-2800 Lyngby, Denmark

Available online 11 August 2006

Abstract

The paper describes the use of synthetic aperture (SA) imaging in medical ultrasound. SA imaging is a radical break with today's commercial systems, where the image is acquired sequentially one image line at a time. This puts a strict limit on the frame rate and the possibility of acquiring a sufficient amount of data for high precision flow estimation. These constrictions can be lifted by employing SA imaging. Here data is acquired simultaneously from all directions over a number of emissions, and the full image can be reconstructed from this data. The paper demonstrates the many benefits of SA imaging. Due to the complete data set, it is possible to have both dynamic transmit and receive focusing to improve contrast and resolution. It is also possible to improve penetration depth by employing codes during ultrasound transmission. Data sets for vector flow imaging can be acquired using short imaging sequences, whereby both the correct velocity magnitude and angle can be estimated. A number of examples of both phantom and in vivo SA images will be presented measured by the experimental ultrasound scanner RASMUS to demonstrate the many benefits of SA imaging.

Keywords: Ultrasound imaging; Synthetic aperture; Vector velocity estimation

1. Introduction

The paper gives a review of synthetic aperture (SA) techniques for medical ultrasound with a description of the current status and the obstacles towards obtaining real-time SA imaging. Synthetic aperture techniques were originally conceived for radar systems in the 1950s and were initially implemented using digital computers in the late 1970s and more advanced techniques were introduced in the late 1980s [1]. There are many similarities between Radar and ultrasound systems, but there are also very significant differences. A SA Radar system usually employs one transmitter and receiver, and the aperture in synthesized by moving the antenna over the region of interest in an airplane or satellite. In medical ultrasound, the array has a fixed number of elements and is usually stationary. The synthesizing is performed by acquiring data from parts of the array to reduce the amount of electronic channels. For Radar, the object is most often in the far-field of the array, whereas the object always is in the near-field of a medical ultrasound system, which complicates the reconstruction. Since the medical array is stationary, it is possible to repeat measurements rapidly, which is not the case for a SA Radar systems. The position between the different elements is also fixed in ultrasound, whereas the deviations from a straight flight path for airplane often have to be compensated for in Radar systems. A vital difference is also that the dynamic range in a Radar image is significantly less than the 40–80 dB dynamic range in ultrasound images.

All these factors affect the implementation of a medical SA ultrasound system and many details have to be changed compared to SA Radar systems to obtain a successful implementation. This paper will describe some of the choices to be made to make a complete SA system that includes vector flow estimation.

Synthetic aperture imaging has been investigated in ultrasonics since the late 1960 and early 1970 [2,3]. In the 1970s and 1980s, it was primarily explored for nondestructive testing (NDT) using a more or less direct implementation of the SA principle, known today as monostatic synthetic aperture imaging [4]. With the introduction of

* Corresponding author. Fax: +45 45 88 01 17.
E-mail address: jaj@oersted.dtu.dk (J.A. Jensen).

0041-624X/$ - see front matter © 2006 Elsevier B.V. All rights reserved.
doi:10.1016/j.ultras.2006.07.017

transducer arrays in the 1970s, focus was gradually directed towards this application area to pursue real-time implementations [5–7].

Until the beginning of 1990, the idea of applying the synthetic aperture imaging approach for medical ultrasound imaging had only been considered occasionally [3,8]. In 1992, O'Donnell and Thomas published a method intended for intravascular imaging based on synthetic aperture imaging utilizing a circular aperture [9]. To overcome the problem with low SNR and impedance matching between the transducer and receiver circuit, the single element transmission was replaced by simultaneous excitation of a multi-element subaperture. Due to the circular surface of the transducer, the subaperture generated a spherical wave with limited angular extend at each emission, thus, permitting synthetic aperture focusing to be applied. This was the first direct attempt to apply synthetic aperture imaging for medical ultrasound imaging. Since then, the application of multi-element subapertures to increase the SNR of synthetic aperture imaging has been investigated using phased array transducers by Karaman and colleagues for small scale systems [10,11], by Lockwood and colleagues for sparse synthetic aperture systems with primary focus on 3D imaging applications [12,13], and by Nikolov and colleagues for recursive ultrasound imaging [14]. In all cases, the multi-element subaperture was used to emulate the radiation pattern of the single element transmission by applying de-focusing delays in such a way that a spherical wave with limited angular extend was produced. The definition of synthetic transmit aperture (STA) imaging was introduced by Chiao and colleagues in [15]. This paper also considered the feasibility of applying spatial encoding to enable transmission on several elements simultaneously, while separating the individual transmissions in the receiver using addition and subtraction of the received signals. A third approach, which utilizes orthogonal Golay codes to increase the SNR, while transmitting simultaneously on several elements, was also considered by Chiao and Thomas in [16].

The influence of motion in STA imaging and methods for compensation have been investigated in several publications [17–21]. Commonly it is reported that axial motion is the dominant factor causing image quality degradation due to the significantly higher spatial frequency in this dimension. The presented motion estimation methods are generally based on time-domain cross-correlation of reference signals to find the shift in position in the axial dimension. Since tissue motion is inherently three dimensional, it is however likely, that to retain the advantages of STA imaging, at least two dimensional (2D) motion correction to compensate successfully for scan plane tissue motion is required.

2. Conventional ultrasound imaging

Conventional ultrasound images are acquired sequentially one image line at a time. The acquisition rate is, thus, limited by the speed of sound c, and the maximum frame rate f_r for an image with N_l lines to a depth of D is

$$f_r = \frac{c}{2DN_l}. \tag{1}$$

For larger depths and increasing number of lines the frame rate gets progressively lower. The approximate 3-dB resolution of an imaging array consisting of N elements with a pitch of D_p is given by

$$b_{3\,dB} = 0.5\frac{D_i}{ND_p}\lambda = 0.5\frac{D_i}{ND_p}\frac{c}{f_0}, \tag{2}$$

where D_i is focus depth and f_0 is center frequency. Assuming the image to cover the full size of the array and a pitch $D_p = \lambda/2$ then gives a frame rate of

$$N_l = \frac{ND_p}{b_{3\,dB}} = 2\frac{f_0}{D_i c}, \quad f_r = \frac{D_i f_0}{DN^2} \tag{3}$$

for a properly sampled image. Current systems increase the number of active elements in the beamformer and better engineering makes it possible to increase the transducer center frequency for the same penetration depth, which lowers the frame rate, if the image quality has to be maintained.

For flow estimation the problem is increased, since several pulse-echo lines have to be acquired from the same direction in order to estimate the blood velocity [22]. Often 8–16 lines have to be used per estimate and this correspondingly lowers the frame rate. It is 6.4 Hz for a depth of 15 cm, 100 image directions and 8 lines per direction for, e.g., scanning the heart. This is an unacceptable low rate, and the area for estimating the velocity is often limited in conventional systems.

A further problem in conventional imaging is the single transmit focus, so that the imaging is only optimally focused at one depth. This can be overcome by making compound imaging using a number of transmit foci, but the frame rate is then correspondingly decreased.

There are, thus, good reasons for developing alternatives to conventional imaging, where the frame rate and single transmit focusing problems can be solved. One alternative is to use synthetic aperture imaging. It will be shown that this can solve both the frame rate and focusing problem, but it also has several problems associated with it in terms of penetration depth, flow estimation, and implementation. The following sections will address these issues and refer to solutions in the literature.

3. Introduction to synthetic aperture imaging

The basic method for acquiring synthetic aperture ultrasound images is shown in Fig. 1. A single element in the transducer aperture is used for transmitting a spherical wave covering the full image region. The received signals for all or part of the elements in the aperture are sampled for each transmission. This data can be used for making a low resolution image, which is only focused in receive due to the un-focused transmission.

Focusing is performed by finding the geometric distance from the transmitting element to the imaging point and back to the receiving element. Dividing this distance by the speed of sound c gives the time instance $t_p(i,j)$ to take out the proper signal value for summation. For an image point $\vec{r}_p$ the time is, thus:

$$t_p(i,j) = \frac{|\vec{r}_p - \vec{r}_e(i)| + |\vec{r}_p - \vec{r}_r(j)|}{c} \quad (4)$$

where $\vec{r}_e(i)$ denotes the position of the transmitting element i and $\vec{r}_r(j)$ the receiving element j's position. This is done for every point in the resulting image to yield a low resolution image. Combining the low resolution images then results in a high resolution image, since fully dynamic focusing has been performed for all points in the image. The final focused signal $y_f(\vec{r}_p)$ is then:

$$y_f(\vec{r}_p) = \sum_{j=1}^{N} \sum_{i=1}^{M} a(t_p(i,j),i,j) y_r(t_p(i,j),i,j) \quad (5)$$

where $y_r(t,i,j)$ is the received signal for emission i on element j, $a(t_p(i,j),i,j)$ is the weighting function (apodization) applied onto this signal, N is the number of transducer elements, and M is the number of emissions. The transmit focusing is, thus, synthesized by combining the low resolution images, and the focusing calculation makes the transmit focus dynamic for all points in the image. The focus is, therefore, both dynamic in transmit and receive and the highest possible resolution for delay-sum beamforcing is obtained everywhere in the image. Note that the focused signal is a function of space, and that this can be anywhere in the image. Focusing can, thus, be performed in any order and direction, and this will later be used to describe a vector flow system in Section 6. It is also only needed to focus at the points, that are actually shown in the final image as suggested in [23,24]. This, however, necessitates that the complex Hilbert transformed received signal is beamformed to find the instantaneous envelope.

SA imaging makes it possible to decouple frame rate and pulse repetition time, as only a sparse set of emissions can be used for creating a full image. Very fast imaging can, therefore, be made albeit with a lower resolution and higher side-lobes. This can be seen in Fig. 2, where the angular resolution is seen for different number of emissions [25]. A 64 channel fully sampled system was used together with a 5 MHz linear array transducer with a pitch of 0.21 mm. The resolution is determined by the width of the transmitting and receiving aperture and the side-lobe levels are determined by the apodization and the number of emissions.

Very fast imaging at the pulse repetition frequency can be attained by using recursive imaging [14]. The approach uses that the SA acquisition sequence is repeated, so that emission 1 is performed again after all emissions have been made. A full image can be made by combining all emissions, which can be from 1 to M or from 2 to M and 1. The new emission 1 can, thus, replace the old emission 1, which can be done by subtracting the old and adding the new emission. This can be done recursively, which results

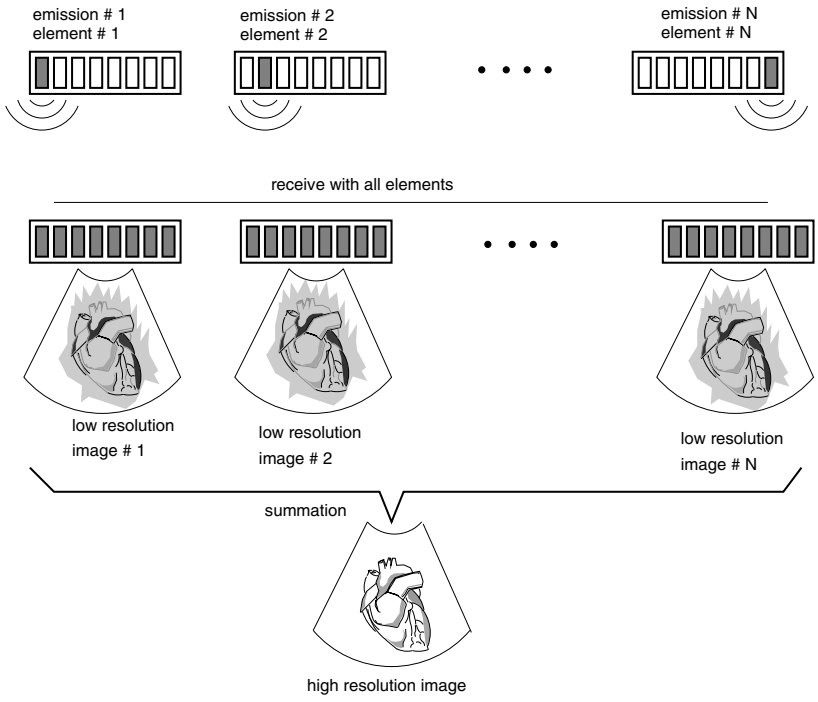

Fig. 1. Basic principle of synthetic aperture ultrasound imaging (from [25]).

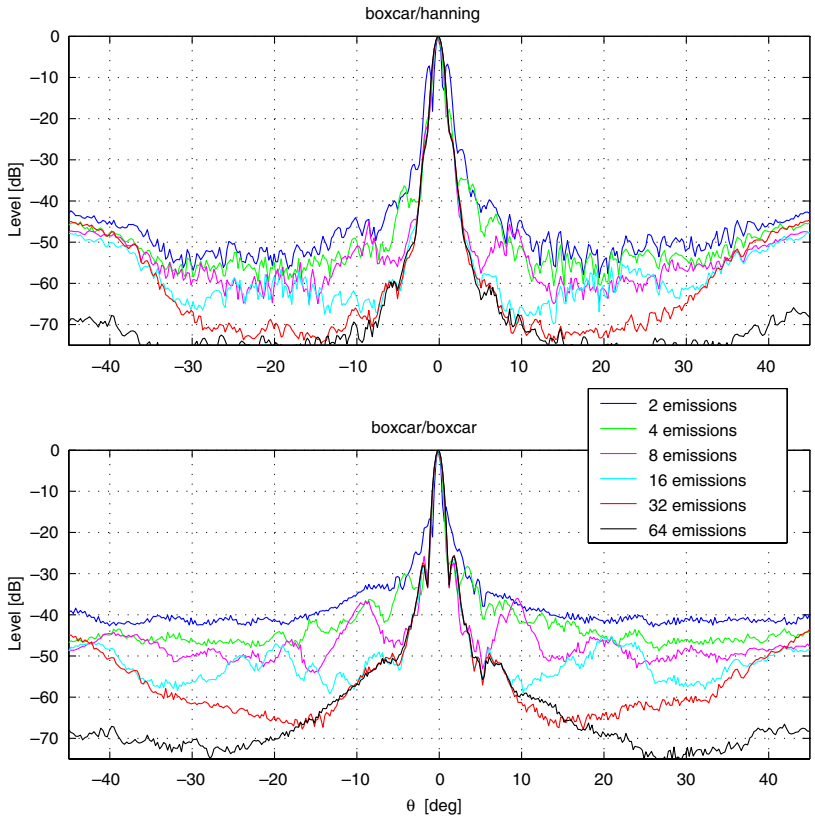

Fig. 2. Angular resolution of a SA imaging system for different number of emissions, when using a boxcar apodization in transmit and a boxcar (bottom) or Hanning apodization in receive (top) (from [25]).

in a new image after every emission. Such an approach can yield very high frame rates and can be used for velocity imaging as described in Section 6.

4. Penetration problem

A major problem in SA imaging is the limited penetration depth, since an un-focused wave is used in transmit and only a single element emits energy. The problem can be solved by combining several elements for transmission and using longer waveforms emitting more energy. Karman et al. [10] suggested combining several elements N_t in transmit, with a delay curve to de-focus the emission to emulate a spherical wave. This can increase the emitted amplitude be a factor of $\sqrt{N_t}$.

It can be combined with using a chirp excitation [26,27] to increase the energy as used in Radar systems [28]. A chirp makes a linear frequency sweep from, e.g., low to high frequencies in the transducer's bandwidth B. Applying a matched filter to the received signal compresses the chirp to a short pulse. The filter is a time reversed version of the pulse and therefore, has the conjugated phase of the chirp. Making the convolution cancels out the phase of the chirp, which makes the resulting signal a linear phase signal and the received signal corresponds to the autocorrelation function of the chirp. Covering the bandwidth of the transducer then gives a resulting pulse or autocorrelation that has a duration proportional to $1/B$. Directly using a rectangular chirp in ultrasound is not possible, as the compressed chirps has temporal side-lobes, which can be as high as -13 dB. This severely limits the contrast of the ultrasound image that has a dynamic range of, e.g., 60 dB. The problem can be solved by applying tapering to the emitted chirp and by applying a window on the matched filter as shown in Fig. 3. The approach was developed in [29–31] that also showed a modest increase in axial resolution of 0.4λ for a gain in signal-to-noise ratio of 10 dB using the modified chirp scheme.

The two approaches can be combined in SA imaging as suggested in [32] to increase the penetration depth. Compared to a conventional ultrasound image the improvement in signal-to-noise ratio is [32]:

$$I_{\mathrm{snr}} = \frac{MN_t}{N_{ct^2}} \frac{N_{Rs}}{N_{Rc}} \frac{T_p}{T_c} \tag{6}$$

where M is the number of emissions for the SA image, N_{Rs} is the number of receive elements and T_p is the duration of the chirp. For the conventional image N_{ct} elements are used in transmit for a pulse of duration T_c seconds and N_{Rc} elements are beamformed in reception. Using the parameters

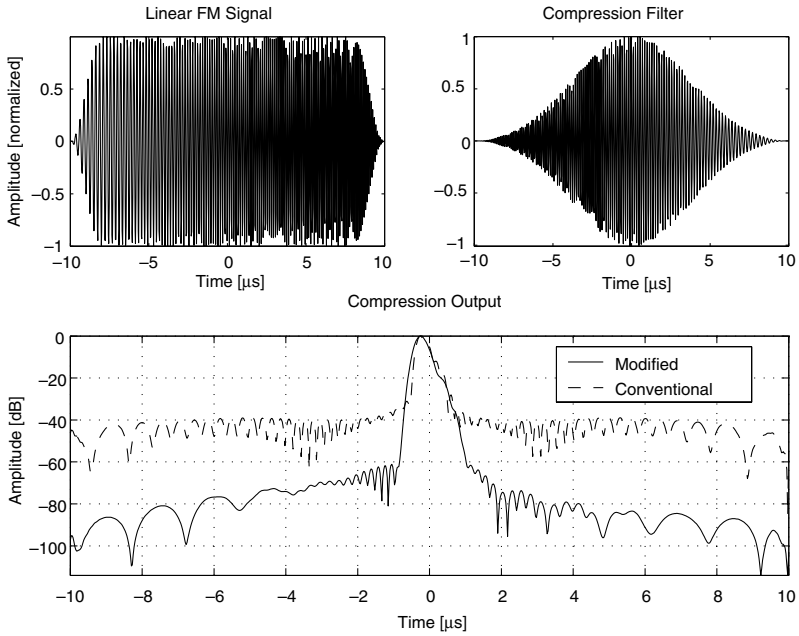

Fig. 3. Top left: Modified linear FM signal with a 7 MHz center frequency and 7 MHz bandwidth. A Tukey window with a duration of 10% has been applied. Top right: Modified compression filter using a Chebychev window with 70 dB relative side-lobe attenuation. Bottom: Compression output for the conventional FM signal (dashed) and the modified FM signal (solid). The effect of a linear array transducer has been introduced in the compression outputs (from [32]).

$M = 96$, $N_t = 33$, $N_{ct} = 64$, $N_{Rs} = 128$, $N_{Rc} = 64$, $T_p = 20$ μs, $T_c = 0.29$ μs for a 7 MHz system theoretically gives a gain of 17 dB. The actual measurement is shown in Fig. 4 and the calculated gain in Fig. 5. The increase in penetration depth is roughly 4 cm or a 40% gain. An improved focusing scheme has increased the gain by up to 6 dB and further increased the penetration depth [33].

5. Equipment and implementation

The data acquisition in SA imaging is radically different from a normal ultrasound system since data have to be stored for all receiving channels and for a number of emissions. Experiments with SA imaging must, thus, be conducted with dedicated equipment, and only few research groups have access to such systems as no commercial SA research systems are available.

We have developed the remotely accessible software configurable multichannel ultrasound sampling (RASMUS) system specifically tailored for acquiring SA images [34,35]. The system houses 128 transmitter channels that can send arbitrary coded signals with a sampling frequency of 40 MHz and a precision of 12 bits. The coded signals can be different from emission to emission and from channel to channel. It also houses 64 receivers that sample at 40 MHz and 12 bits. They are connected to 1-to-2 multiplexers, so that 128 elements can be sampled over two pulse emissions. The receivers each have associated 256 Mbytes of RAM and can, therefore, sample continuously for more than 3 s to cover a number of heart cycles. The total RAM in the system is more than 24 Gbytes and more than 72 large FPGAs can be used for processing the data [35]. All conventional ultrasound imaging methods can be implemented, but real-time SA imaging is not possible. The data are here stored in the RAM and later processed on a Linux cluster. All the measurements presented in this paper are made with the RASMUS system. A photo of the system and one receiver board for 16 channels is shown in Fig. 6.

6. Flow estimation

In SA imaging, it is possible to focus the received data in any direction and in any order. It does not have to be along the direction of the emitted beam, since the emission is spherical and illuminates the full region of interest. It is, thus, possible to track motion of objects in any direction. This can be used to devise a full vector velocity imaging system.

Conventional ultrasound velocity systems estimate the velocity by finding the shift in position of the scatterers over time [22]. This is done by acquiring lines from the same direction 8 to 16 times and then correlate the data to find the shift in position between lines as either a phase shift [36] or as a time shift [37]. Dividing the spatial shift by the time then gives the velocity. The methods only find the velocity along the ultrasound direction, the standard deviation is often high, and the frame rate is lowered by the number of emissions per direction.

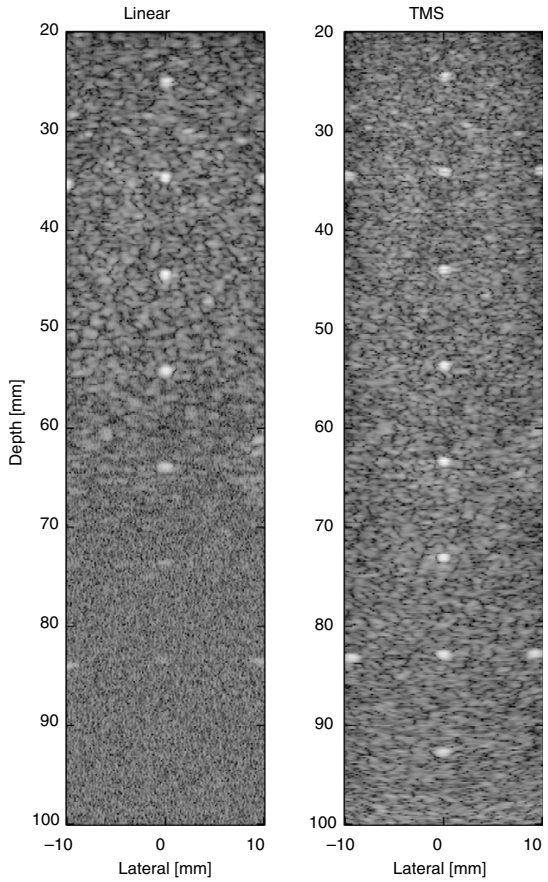

Fig. 4. Measured linear array image (left) and TMS image (right) on a multi-target phantom with 0.5 dB/(cm MHz) attenuation. The scanned section contains twisted nylon wires spaced axially by 1 cm throughout the imaged region. The dynamic range in the images is 50 dB (from [32]).

In SA imaging, the received data can be focused along the direction of the flow as shown in Fig. 7. A short sequence of emissions of $M = 4$–8 is used and the high resolution image lines $y(x')$ are then focused along the flow direction x'. A velocity $\vec{v}$ results in a displacement between high resolution images of

$$\Delta x' = |\vec{v}| M T_{\text{prf}} \tag{7}$$

where T_{prf} is the time between emissions. Data for the first high resolution image line is $y_1(x')$ and the next high resolution image line is $y_2(x') = y_1(x' - \Delta x')$. Cross-correlating the two lines gives a peak at $\Delta x'$ and dividing by MT_{prf} then yields the true velocity magnitude $|\vec{v}|$. This can be done in any direction, also transverse to the normal ultrasound direction of propagation, and the correct velocity magnitude can, therefore, be found [38,39].

The approach has been investigated using a re-circulating flow rig. A 7 MHz linear array with 128 elements was used together with the RASMUS system. A sequence with 8 emissions, using 11 elements and a 20 μs chirp was employed. The flow estimation was performed for 128

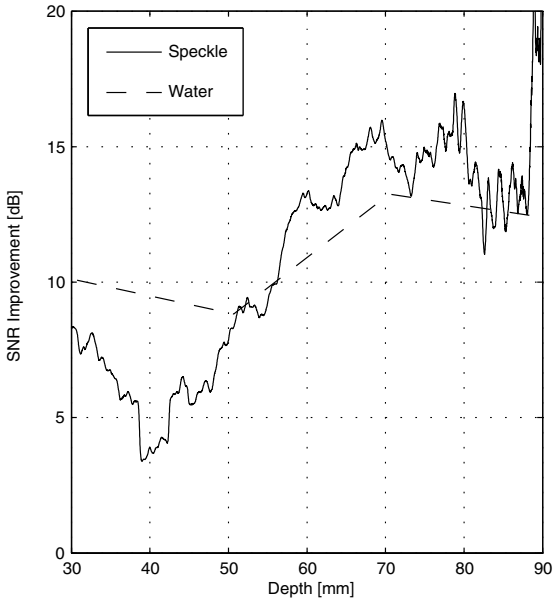

Fig. 5. Calculated SNR improvement obtained by TMS imaging in water (dashed) and in the tissue mimicking phantom (solid) (from [32]).

emissions and the flow profiles for a fully transverse flow is shown in Fig. 8. The relative standard deviation is 1.2% over the full profile, where a normal system would show a velocity of 0. At 60°, the relative standard deviation is 0.36% [38]. The 128 emissions can also be used for making a full color flow image as shown in Fig. 9 for the flow rig and in vivo for the carotid artery and jugular vein in Fig. 10. The estimates are shown without any averaging or image processing as is used in commercial scanners.

The advantages of the approach is that the velocity can be accurately found in any direction, and that the color flow imaging can be done very fast. Only 128 emissions are needed, where a normal system would need roughly 800 for 100 image directions. The data is also continuously available for all image directions and the velocity can be estimated for as many emissions as the velocity can be assumed constant. The continuous data also makes it easier to perform stationary echo canceling to separate tissue and blood signals, since filters can have any length and initialization can be neglected.

The flow angle must be known before beamforming in the flow direction, and this was in the previous examples estimated from the B-mode image. It can, however, also be estimated from the actual data. For the actual direction the correlation of the data $y_1(x')$ and $y_2(x')$ is highest. For other directions the correlation will drop, since the velocities along that line are different due to the velocity profile of the blood [22]. Calculating the maximum normalized correlation as a function of angle as in [40], thus, gives an index from which the maximum determines the angle as shown in Fig. 11. The function here has a peak at the correct value of 90°. The angle estimates for the profiles

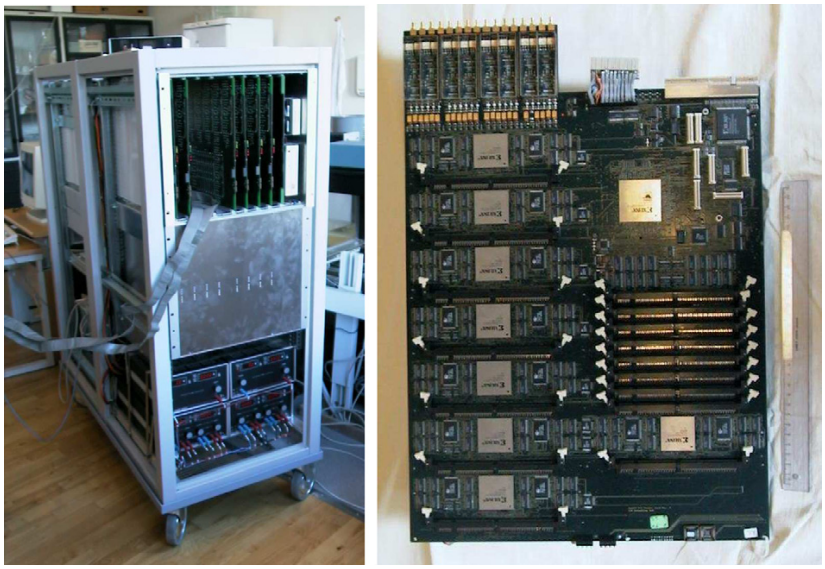

Fig. 6. Photos of the RASMUS scanner (left) with one of the 8 channel receiver boards. The digital part of the system is shown with the 64 receivers in the top cabinet, the 128 transmitters in the middle, and the analog power supplies on the bottom. The analog front-end and transducer plug are at the other side of the 19 in. racks. (from [35]).

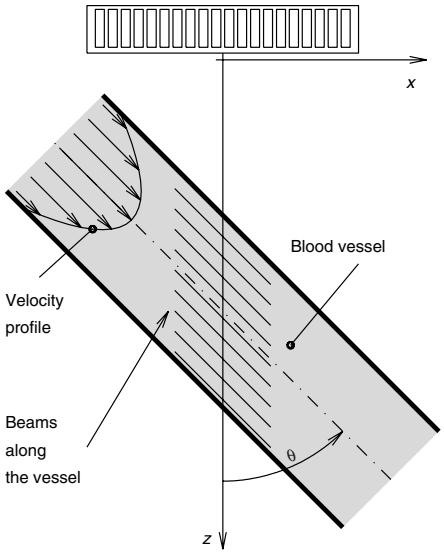

Fig. 7. Beamforming is made along the laminar flow (from [38]).

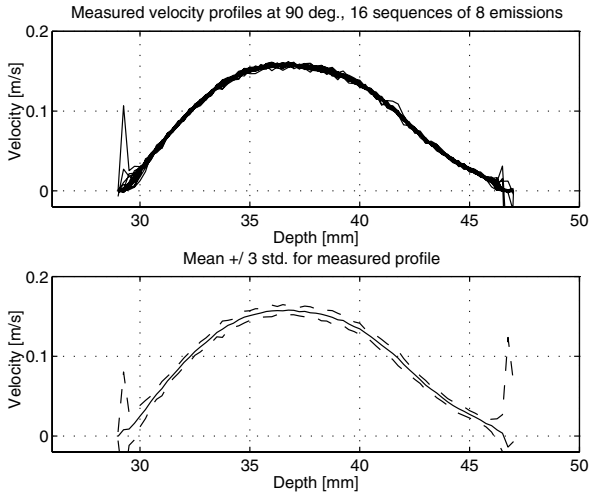

Fig. 8. Estimated profiles from the flow rig at a 90° flow angle. The top graph shows 20 independent profiles estimated and the bottom graph shows the mean profile (solid line) ± 3 standard deviations (dashed lines). From [38].

shown in Fig. 9 are shown in Fig. 12. The mean value is 90.0003° and the standard deviation is 1.32° [40]. The resulting color flow image with arrows indicating direction and magnitude is shown in Fig. 13.

7. Motion compensation

The accurate velocity estimation can also be used for compensating for tissue motion during the SA acquisition process. High quality SA images will often take up to 100 emissions and high tissue velocities will degrade the image quality since the individual low resolution images are not summed in phase. The B-mode sequence can then be inter-spaced with a flow sequence and the tissue velocity can be estimated from this data. Knowing the velocity is then used for correcting the position of the low resolution images that then can be summed in phase. This was suggested in [32,25], where

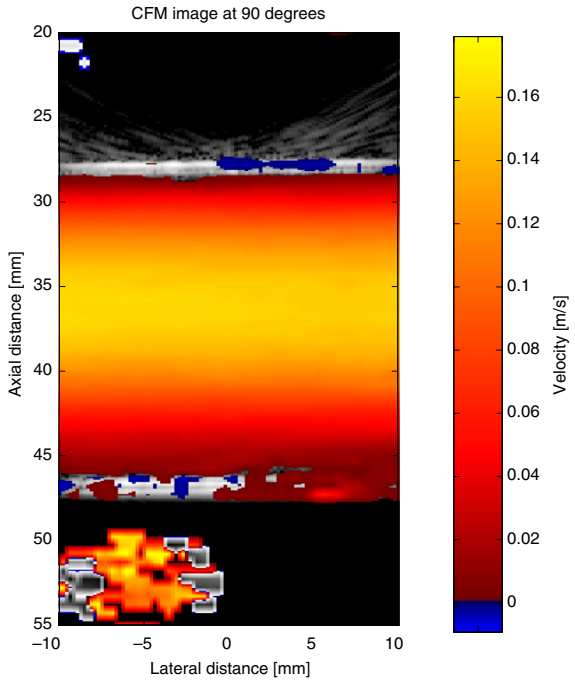

Fig. 9. Synthetic aperture color flow map image of flow rig data at a 90° flow angle obtained using 128 emissions (from [38]). (For interpretation of the references in color in this figure legend, the reader is referred to the web version of this article.)

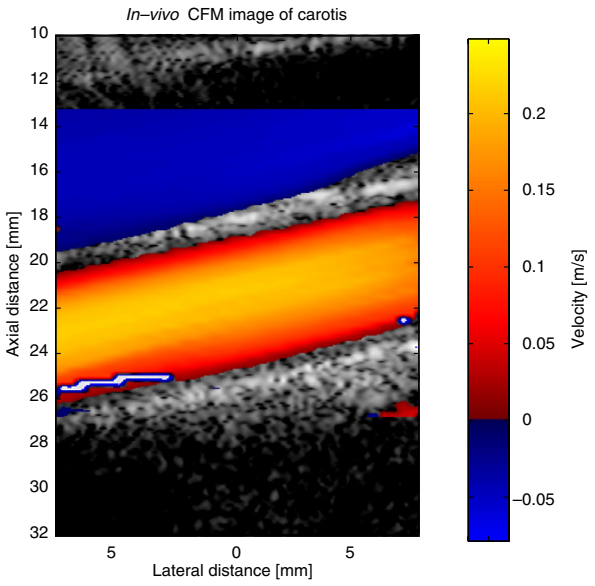

Fig. 10. In vivo color flow map image at a 77° flow angle for the jugular vein and carotid artery. The color scale indicates the velocity along the flow direction, where red hues indicate forward flow and blue reverse flow (from [38]). (For interpretation of the references in color in this figure legend, the reader is referred to the web version of this article.)

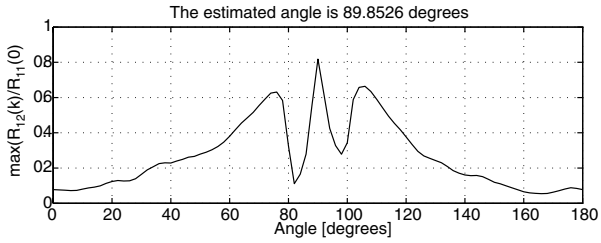

Fig. 11. Normalized maximum correlation as a function of beam formation angle.

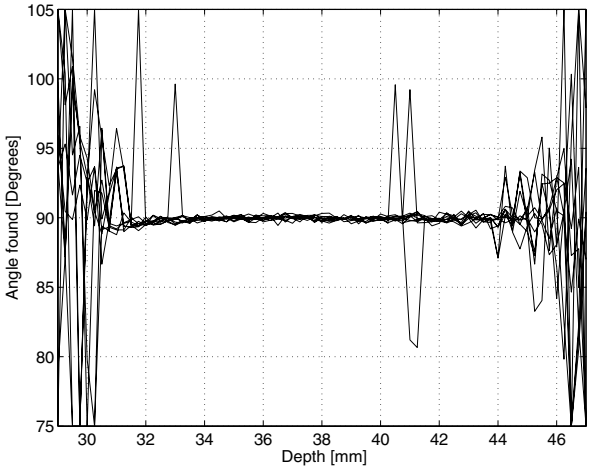

Fig. 12. Estimated velocity angles for a true velocity angle of 90° (from [40]).

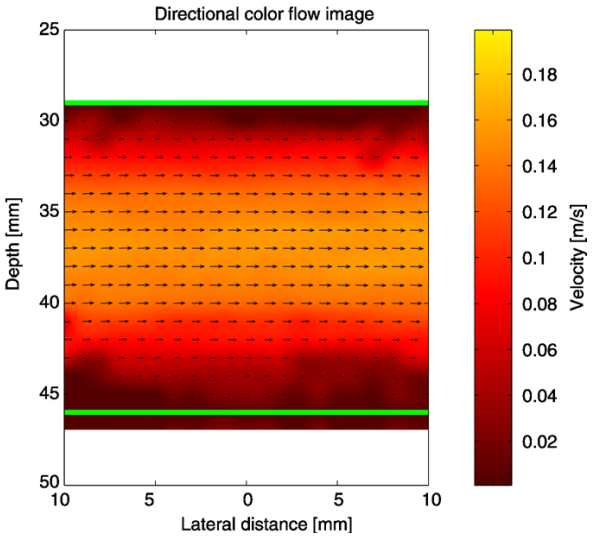

Fig. 13. Vector flow image for data from Fig. 9, when the direction also is estimated. The color show the transverse velocity and the arrows shows velocity magnitude and direction. (For interpretation of the references in color in this figure legend, the reader is referred to the web version of this article.)

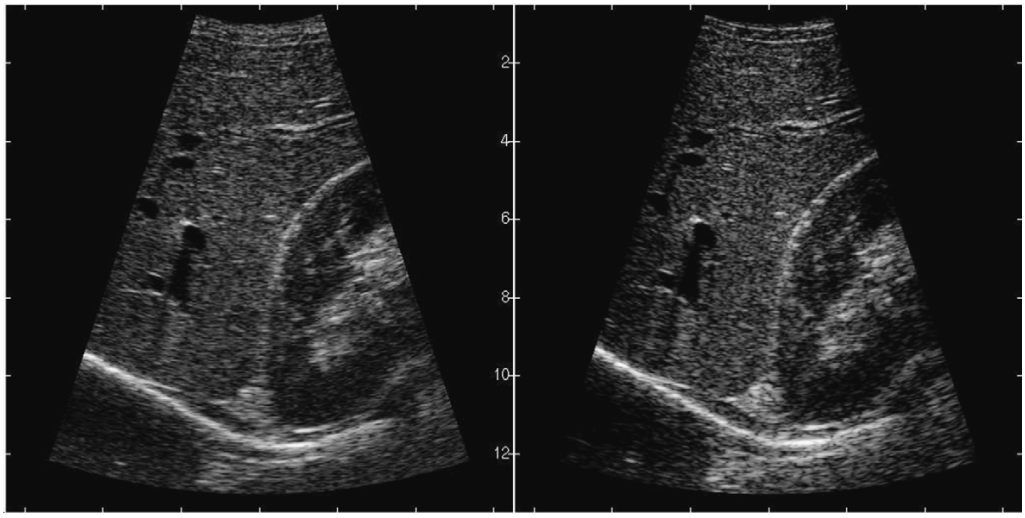

Fig. 14. Examples in vivo images. Left part is the conventional and right is the STA image showing the longitudinal section of right liver lobe showing cross-sections of hepatic vein branches, longitudinal section of a portal a vein branch (upper left part), the kidney, and diaphragm at the bottom.

is was shown that the scheme removes the motion artifacts. Other motion compensation schemes have been studied in [17,19,25].

8. Clinical results

From the previous sections, it can be seen that SA imaging has a large array of advantages compared to conventional ultrasound imaging. It is, however, not clear whether these advantages also translate to the clinical image, and it is, therefore, important to conduct pre-clinical trials to realistically study the performance of SA systems. This can be done with the RASMUS system described in Section 5. It is here possible to acquire in vivo real-time data and then make off-line processing for finding the clinical performance. This has been done in [41,42], where the system was programmed to acquire both a conventional convex array image and a SA image. The sequences were acquired interleaved to have the same region of interest, transducer, and measurement system at the same time. The only change is, thus, the imaging method. An example of such images are shown in Fig. 14 for the liver and right kidney. Seven human volunteers were scanned at two positions for both SA and conventional imaging yielding 28 videos. The sequences were presented to three experienced medical doctors in a double blinded experiment and they were asked to evaluate the images in terms of penetration depth and relative performance between the two images.

The clinical evaluation showed a minute (0.48 cm) but significant ($P = 0.008$) increase in penetration depth using synthetic aperture with coded excitation. Image quality evaluation showed highly significant ($P < 0.001$) improvement in SA images compared to conventional images, which was also expected by the authors due to the apparent improved resolution throughout the SA images.

9. Advanced coded imaging

In the approaches shown in this paper only a single emission center is active at the same time. This limits the emitted energy and the amount of information acquired per emission. It is quite inexpensive to make a transmitter compared to a receiver, and it is, therefore, an advantage to use several emissions simultaneously. Several authors have addressed this problem. Hadamard encoding was suggested in [15] to spatially encode the waveforms, where the Hadamard matrix is multiplied onto the waveforms for the multiple transmissions for a number of transmissions. The Hadamard matrix can also be used for decoding the waveforms, provided the object under investigation is stationary.

This problems was solved in the spread spectrum approach suggested in [43,44]. Here each transmitter is assigned a narrow frequency band. The signals for the individual sources can then be separated using matched filters provided that the bands are disjoint. The high resolution image can then be made by repeating the procedure for all frequency bands for all emitters and then combine all the received signals after filtration. The approach can be used for flow estimation, since the separation is not done over a number of emissions [44].

Methods for even doing single excitation imaging has also be suggested by a number of authors [45–49] and the research fields is still very active. It can potentially lead to a higher penetration and more precise flow images, if the problems with the, e.g., image quality, intensity levels, and computational load can be solved.

10. Summary

This paper has given examples of how medical SA ultrasound imaging can be acquired and processed. It has been

shown that problems with penetration depth, flow, and motion can be solved, and that high quality in vivo SA images can be acquired. It has been demonstrated in pre-clinical studies on human volunteers that the SA image resolution and penetration depth are larger than for conventional ultrasound images. Further, the data can be used for vectorial velocity estimation, where both direction and magnitude of the flow vectors can be determined in any direction with a relative standard deviation of a few percent making it possible to construct quantitative SA vector flow systems.

References

[1] M. Soumekh, Synthetic Aperture Radar. Signal Processing with MATLAB Algorithms, John Wiley & Sons, Inc., New York, 1999.

[2] J.J. Flaherty, K.R. Erikson, V.M. Lund. Synthetic aperture ultrasound imaging systems, United States Patent, US 3,548,642, 1967.

[3] C.B. Burckhardt, P-A. Grandchamp, H. Hoffmann, An experimental 2 MHz synthetic aperture sonar system intended for medical use, IEEE Trans. Son. Ultrason. 21 (1) (1974) 1–6.

[4] J.T. Ylitalo, H. Ermert, Ultrasound synthetic aperture imaging: monostatic approach, IEEE Trans. Ultrason. Ferroelec. Freq. Contr. 41 (1994) 333–339.

[5] P.D. Corl, P.M. Grant, G.S. Kino, A digital synthetic focus acoustic imaging system for NDE, in: Proceedings of the IEEE Ultrasonic Symposium, 1978, pp. 263–268.

[6] G.S. Kino, D. Corl, S. Bennett, K. Peterson, Real time synthetic aperture imaging system, in: Proceedings of the IEEE Ultrasonic Symposium, 1980, pp. 722–731.

[7] D.K. Peterson, G.S. Kino, Real-time digital image reconstruction: a description of imaging hardware and an analysis of quantization errors, IEEE Trans. Son. Ultrason. 31 (1984) 337–351.

[8] K. Nagai, A new synthetic-aperture focusing method for ultrasonic *B*-scan imaging by the fourier transform, IEEE Trans. Son. Ultrason. SU-32 (4) (1985) 531–536.

[9] M. O'Donnell, L.J. Thomas, Efficient synthetic aperture imaging from a circular aperture with possible application to catheter-based imaging, IEEE Trans. Ultrason. Ferroelec. Freq. Contr. 39 (1992) 366–380.

[10] M. Karaman, P.C. Li, M. O'Donnell, Synthetic aperture imaging for small scale systems, IEEE Trans. Ultrason. Ferroelec. Freq. Contr. 42 (1995) 429–442.

[11] M. Karaman, M. O'Donnell, Subaperture processing for ultrasonic imaging, IEEE Trans. Ultrason. Ferroelec. Freq. Contr. 45 (1998) 126–135.

[12] G.R. Lockwood, F.S. Foster, Design of sparse array imaging systems, in: Proceedings of the IEEE Ultrasonic Symposium, 1995 pp. 1237–1243.

[13] G.R. Lockwood, J.R. Talman, S.S. Brunke, Real-time 3-D ultrasound imaging using sparse synthetic aperture beamforming, IEEE Trans. Ultrason. Ferroelec. Freq. Contr. 45 (1998) 980–988.

[14] S.I. Nikolov, K. Gammelmark, J.A. Jensen, Recursive ultrasound imaging, in: Proceedings of the IEEE Ultrasonic Symposium, vol. 2, 1999, pp. 1621–1625.

[15] R.Y. Chiao, L.J. Thomas, S.D. Silverstein, Sparse array imaging with spatially-encoded transmits, in: Proceedings of the IEEE Ultrasonic Symposium, 1997, pp. 1679–1682.

[16] R.Y. Chiao, L.J. Thomas, Synthetic transmit aperture using orthogonal golay coded excitation, in: Proceedings of the IEEE Ultrasonic Symposium, 2000, pp. 1469–1472.

[17] G.E. Trahey, L.F. Nock, Synthetic receive aperture imaging with phase correction for motion and for tissue inhomogenities – part II: effects of and correction for motion, IEEE Trans. Ultrason. Ferroelec. Freq. Contr. 39 (1992) 496–501.

[18] H.Ş. Bilge, M. Karaman, M. O'Donnell, Motion estimation using common spatial frequencies in synthetic aperture imaging, in: Proceedings of the IEEE Ultrasonic Symposium, 1996, pp. 1551–1554.

[19] M. Karaman, H.Ş. Bilge, M. O'Donnell, Adaptive multi-element synthetic aperture imaging with motion and phase aberation correction, IEEE Trans. Ultrason. Ferroelec. Freq. Contr. 42 (1998) 1077–1087.

[20] C.R. Hazard, G.R. Lockwood, Effects of motion artifacts on a synthetic aperture beamformer for real-time 3D ultrasound, in: Proceedings of the IEEE Ultrasonic Symposium, 1999, pp. 1221–1224.

[21] J.S. Jeong, J.S. Hwang, M.H. Bae, T.K. Song, Effects and limitations of motion compensation in synthetic aperture techniques, in: Proceedings of the IEEE Ultrasonic Symposium, 2000, pp. 1759–1762.

[22] J.A. Jensen, Estimation of Blood Velocities Using Ultrasound: A Signal Processing Approach, Cambridge University Press, New York, 1996.

[23] M. Karaman, A. Atalar, H. Köymen, VLSI circuits for adaptive digital beamforming in ultrasound imaging, IEEE Trans. Med. Imag. 12 (1993) 711–720.

[24] B.G. Tomov, J.A. Jensen, Compact implementation of dynamic receive apodization in ultrasound scanners. in: Proceedings of the SPIE – Medical Imaging, 2004, pp. 260–271.

[25] S.I. Nikolov, Synthetic aperture tissue and flow ultrasound imaging, PhD Thesis, Ørsted. DTU, Technical University of Denmark, 2800, Lyngby, Denmark, 2001.

[26] Y. Takeuchi, An investigation of a spread energy method for medical ultrasound systems – part one: theory and investigations, Ultrasonics (1979) pp. 175–182.

[27] M. O'Donnell, Coded excitation system for improving the penetration of real-time phased-array imaging systems, IEEE Trans. Ultrason. Ferroelec. Freq. Contr. 39 (1992) 341–351.

[28] M.I. Skolnik, Introduction to Radar Systems, McGraw-Hill, New York, 1980.

[29] T. Misaridis, Ultrasound imaging using coded signals, PhD Thesis, Ørsted. DTU, Technical University of Denmark, Lyngby, Denmark, 2001.

[30] T.X. Misaridis, K. Gammelmark, C.H. Jørgensen, N. Lindberg, A.H. Thomsen, M.H. Pedersen, J.A. Jensen, Potential of coded excitation in medical ultrasound imaging, Ultrasonics 38 (2000) 183–189.

[31] T. Misaridis, J.A. Jensen, Use of modulated excitation signals in ultrasound. Part I: basic concepts and expected benefits, IEEE Trans. Ultrason. Ferroelec. Freq. Contr. (2005) 192–207.

[32] K.L. Gammelmark, J.A. Jensen, Multielement synthetic transmit aperture imaging using temporal encoding, IEEE Trans. Med. Imag. 22 (4) (2003) 552–563.

[33] K. Gammelmark, Improving the Image Quality of Synthetic Transmit Aperture Ultrasound Images, PhD Thesis, Ørsted. DTU, Technical University of Denmark, 2800, Lyngby, Denmark, 2004.

[34] J.A. Jensen, O. Holm, L.J. Jensen, H. Bendsen, H.M. Pedersen, K. Salomonsen, J. Hansen, S. Nikolov, Experimental ultrasound system for real-time synthetic imaging. in: Proceedings of the IEEE Ultrasonic Symposium, vol. 2, 1999, pp. 1595–1599.

[35] J.A. Jensen, O. Holm, L.J. Jensen, H. Bendsen, S.I. Nikolov, B.G. Tomov, P. Munk, M. Hansen, K. Salomonsen, J. Hansen, K. Gormsen, H.M. Pedersen, K.L. Gammelmark, Ultrasound research scanner for real-time synthetic aperture image acquisition, IEEE Trans. Ultrason. Ferroelec. Freq. Contr. 52 (5) (2005).

[36] C. Kasai, K. Namekawa, A. Koyano, R. Omoto, Real-time two-dimensional blood flow imaging using an autocorrelation technique, IEEE Trans. Son. Ultrason. 32 (1985) 458–463.

[37] O. Bonnefous, P. Pesqué, Time domain formulation of pulse-Doppler ultrasound and blood velocity estimation by cross correlation, Ultrason. Imag. 8 (1986) 73–85.

[38] J.A. Jensen, S.I. Nikolov, Directional synthetic aperture flow imaging, IEEE Trans. Ultrason. Ferroelec. Freq. Contr. (2004) 1107–1118.

[39] J.A. Jensen, S.I. Nikolov, Transverse flow imaging using synthetic aperture directional beamforming, in: Proceedings of the IEEE Ultrasonic Symposium, 2002, pp. 1488–1492.
[40] J.A. Jensen, Velocity vector estimation in synthetic aperture flow and B-mode imaging, in: IEEE International Symposium on Biomedical Imaging from Nano to Macro, 2004, pp. 32–35.
[41] M.H. Pedersen, K.L. Gammelmark, J.A. Jensen, Preliminary in vivo evaluation of convex array synthetic aperture imaging, in: Proceedings of the SPIE – Progress in Biomedical Optics and Imaging, 2004, pp. 33–43.
[42] M.H. Pedersen, K.L. Gammelmark, J.A. Jensen, In vivo evaluation of convex array synthetic aperture imaging, Ultrasound Med. Biol., accepted for publication.
[43] F. Gran, J.A. Jensen, Multi element synthetic aperture transmission using a frequency division approach, in: Proceedings of the IEEE Ultrasonic Symposium, 2003, pp. 1942–1946.
[44] F. Gran, J.A. Jensen, Spatio-temporal encoding using narrow-band linearly frequency modulated signals in synthetic aperture ultrasound imaging, in: Proceedings of the SPIE – Progress in Biomedical Optics and Imaging, Ultrasonic Imaging and Signal Processing, vol. 5750, 2005, pp. 405–416.
[45] J. Shen, E.S. Ebbini, A new coded-excitation ultrasound imaging system-part 1: basic principles, IEEE Trans. Ultrason. Ferroelec. Freq. Contr. 43 (1) (1996) 131–140.
[46] J. Shen, E.S. Ebbini, A new coded-excitation ultrasound imaging system-part 2: operator design, IEEE Trans. Ultrason. Ferroelec. Freq. Contr. 43 (1) (1996) 141–148.
[47] F. Gran, J.A. Jensen, A. Jakobsson, A code division technique for multiple element synthetic aperture transmission, in: Proceedings of the SPIE – Progress in Biomedical Optics and Imaging, vol. 5373, 2004, pp. 300–306.
[48] T. Misaridis, P. Munk, J.A. Jensen, Parallel multi-focusing using plane wave decomposition, in: Proceedings of the IEEE Ultrasonic Symposium vol. 2, 2003, pp. 1565–1568.
[49] T. Misaridis, J.A. Jensen, Use of modulated excitation signals in ultrasound. Part III: high frame rate imaging, IEEE Trans. Ultrason. Ferroelec. Freq. Contr. (2005) 220–230.

CHAPTER

SIX

Sequential beamforming for synthetic aperture imaging

Taken from the paper:

Jacob Kortbek, Jørgen Arendt Jensen and Kim Løkke Gammelmark,

Sequential beamforming for synthetic aperture imaging

Ultrasonics, Vol. 53, No. 1, 2013, p. 1-16.

Ultrasonics 53 (2013) 1–16

Contents lists available at SciVerse ScienceDirect

Ultrasonics

journal homepage: www.elsevier.com/locate/ultras

Sequential beamforming for synthetic aperture imaging

Jacob Kortbek [a,b,*], Jørgen Arendt Jensen [b], Kim Løkke Gammelmark [a]

[a] BK Medical, 2730 Herlev, Denmark
[b] Department of Electrical Engineering, Center for Fast Ultrasound, Technical University of Denmark, Denmark

ARTICLE INFO

Article history:
Received 6 December 2010
Received in revised form 2 March 2012
Accepted 1 June 2012
Available online 28 June 2012

Keywords:
Beamforming
Synthetic aperture
Ultrasound imaging

ABSTRACT

Synthetic aperture sequential beamforming (SASB) is a novel technique which allows to implement synthetic aperture beamforming on a system with a restricted complexity, and without storing RF-data. The objective is to improve lateral resolution and obtain a more depth independent resolution compared to conventional ultrasound imaging. SASB is a two-stage procedure using two separate beamformers. The initial step is to construct and store a set of B-mode image lines using a single focal point in both transmit and receive. The focal points are considered virtual sources and virtual receivers making up a virtual array. The second stage applies the focused image lines from the first stage as input data, and take advantage of the virtual array in the delay and sum beamforming. The size of the virtual array is dynamically expanded and the image is dynamically focused in both transmit and receive and a range independent lateral resolution is obtained. The SASB method has been investigated using simulations in Field II and by off-line processing of data acquired with a commercial scanner. The lateral resolution increases with a decreasing $F\#$. Grating lobes appear if $F\# \leqslant 2$ for a linear array with λ-pitch. The performance of SASB with the virtual source at 20 mm and $F\# = 1.5$ is compared with conventional dynamic receive focusing (DRF). The axial resolution is the same for the two methods. For the lateral resolution there is improvement in FWHM of at least a factor of 2 and the improvement at -40 dB is at least a factor of 3. With SASB the resolution is almost constant throughout the range. For DRF the FWHM increases almost linearly with range and the resolution at -40 dB is fluctuating with range. The theoretical potential improvement in SNR of SASB over DRF has been estimated. An improvement is attained at the entire range, and at a depth of 80 mm the improvement is 8 dB.

Contents

* Corresponding author at: BK Medical, 2730 Herlev, Denmark.
E-mail address: jbk@bkmed.dk (J. Kortbek).

0041-624X/$ - see front matter © 2012 Elsevier B.V. All rights reserved.
http://dx.doi.org/10.1016/j.ultras.2012.06.006

1. Introduction

Inspired by synthetic aperture (SA) radar techniques [1–3], SA ultrasound imaging has been investigated thoroughly for many years. In synthetic transmit aperture (STA) imaging [4,5] a single element is used to transmit a spherical wave that occupies the entire region of interest. The backscattered signals are registered using a multi-element receive aperture and RF-samples from all channels are stored. Delay-and-sum (DAS) beamforming can be applied to these data to construct a low-resolution image (LRI), hence an image constructed from a single emission. Several emissions from single elements across the aperture will synthesize a larger aperture and the LRI's from these emissions can be added into a single high-resolution image (HRI). The HRI is dynamically focused in both transmit and receive yielding an improvement in resolution [6]. This has been confirmed with side-by-side comparisons with conventional ultrasound imaging in pre-clinical trials by Pedersen et al. [7]. This imaging technique sets high demands on processing capabilities, data transport, and storage and makes implementation of a full SA system very challenging and costly. The method investigated in this paper is another variation on SA processing. The objective is to reduce the demands on the system making it a more realistic task to implement, while still preserving benefits in imaging performance.

Many variations of synthetic aperture focusing (SAF) and examples of implementation have been reported with improvements in both frame rate, penetration, and lateral resolution. A simple real-time single channel system with a multiplexer for array imaging was described by Peterson and Kino [8] back in 1984. In the mono-static approach [6] the same element serves as a transmitter and a receiver. A SA technique suitable for a hand held system using a multi-element transmit and receive aperture was described by Karaman et al. [4]. Lockwood and Hazard described a sparse SA beamforming technique for three-dimensional ultrasound imaging using a few transmit pulses for each image [9,10]. A SA method for a circular aperture was investigated by O'Donnell and Thomas [11].

The concept of using the transmit focal point as a virtual source (VS) or a virtual aperture was introduced by Passmann and Ermert [12]. Virtual sources in SAF was further investigated by Frazier and O'Brien [13], Nikolov and Jensen [14,15], and Bae and Jeong [16]. It was shown that the virtual source coincides with the focal point of the transducer, and that a depth independent resolution can be achieved.

Mono-static SA focusing applied to imaging with a single rotating mechanically focused concave element was investigated by Kortbek et al. [17]. Such an imaging system can e.g. be found in an anorectal ultrasound transducer. One objective of this study was to improve lateral resolution. This was done by storing the RF-lines (the beamformed image-lines before envelope detection) from every emission and feeding these to a SA beamformer. Due to the small radius of rotation, the synthesized aperture only experiences a moderate lateral expansion, and the improvement in lateral resolution was not significant.

In this paper the same SAF technique is applied but to linear array imaging. Here the synthesized aperture becomes considerable larger with a lateral translation of the VS than with a rotation. Instead of having a VS created from a single concave element physically focused in both transmit and receive, the VS is now created from a sub-aperture – a group of elements. This offers more flexibility, since the position and the opening angle of the VS are determined by the electronic focusing instead of the physical concave shape of the single element transducer. The receive focusing is a simple fixed focusing with the receive focal point at the same position as the transmit focal point. This first beamformer, thus, mimics the focusing that is a consequence of the concave single element transducer. The focused RF-lines from every emission are stored and transferred to a SA beamformer just as the one applied with the rotating transducer. Two beamformers are, thus, applied sequentially – a simple fixed focus beamformer and a SA beamformer, and the method is denoted Synthetic Aperture Sequential Beamforming (SASB).

One objective of SASB is to improve the penetration depth. The primary objective though is to improve lateral resolution and obtain a more range independent resolution compared to conventional ultrasound imaging. Contrary to a full SA setup only a single RF-line is beamformed and stored for each emission. This reduces the system requirements significantly. For simplicity the method is investigated using a linear array, but it might as well apply to other types of imaging. The investigation comprises performance evaluation at a large imaging range. This is done without consideration for the typical use of the specific transducer but as a mean to demonstrate the properties of the method.

The SASB method is described in more detail in Section 2. Section 3 presents results from the Field II [18,19] simulation study. A parameter study shows the performance and artifacts of the method and compare with conventional dynamic receive focusing (DRF). Section 4 presents imaging examples and signal-to-noise ratio (SNR) calculations with data acquired from phantom measurements with a commercial scanner.

2. Method

Synthetic aperture sequential beamforming (SASB) is a two-stage procedure which can be applied to B-mode imaging with any array transducer. The initial step is to construct and store a set of B-mode image lines using a conventional sliding sub-aperture. These 1st stage lines are obtained with a single focal point in both transmit and receive. The second stage consists of an additional beamformer using the focused image-lines from the first stage as input data. The concept of virtual sources and means of calculating the focusing delays are briefly discussed in Section 2.1 before presenting the SASB in more detail in Section 2.2.

2.1. Virtual sources and focusing delays

In delay-and-sum receive focusing appropriate delays are applied to the responses of the individual transducer elements originating from the focusing point and coherently adding these responses. The delays are found from the round trip time-of-flight (TOF), which is the propagation time of the emitted wave in its path from the transmit origin, $\vec{r}_e$ to the focusing point (FP), $\vec{r}_{fp}$ and return to one of the elements of the receive aperture, $\vec{r}_r$ as illustrated in Fig. 1. This could be the case of mono-static SAF.

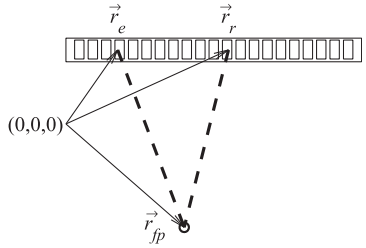

Fig. 1. Wave propagation path (dotted line) for calculating the time-of-flight in receive focusing. The transmit origin, $\vec{r}_e$ and the receive point, $\vec{r}_r$ are illustrated as different elements of an array.

$$t_{tof} = \frac{d}{c} = \frac{|\vec{r}_{fp} - \vec{r}_e| + |\vec{r}_r - \vec{r}_{fp}|}{c}. \quad (1)$$

d is the length of the path, and c is the speed of sound. The sample index of the temporal RF signal is calculated by simply multiplying t_{tof} with the sampling frequency, f_s. The transmit origin is not necessarily well defined, if the emitted pressure wave does not emanate from a single element point source as illustrated in Fig. 1. In multi-element synthetic aperture imaging [4] a multi-element transmit sub-aperture is introduced as an alternative to mono-static SAF to ensure sufficient transmitted energy. Here the pressure wave is the result of numerous waves emitted from multiple elements. With a focused transmission the focal point is introduced as a virtual source, since a spherical wave emanates from this point in a limited angular region. With a known position of the source this allows for the SAF delays to be calculated.

Applying a VS instead of a single element source has consequences for the calculations of SA focusing delays. Time-delay calculations for different applications was discussed by Kortbek et al. [20]. In dynamic receive beamforming a new set of delay values is calculated for each focusing point (FP). Assuming the speed of sound c is known, the delay value, t_d for the receiving element with position $\vec{r}_r$ is calculated in accordance with Fig. 2 (left)

$$t_{d_{fp}}(\vec{r}_r) = \frac{|\vec{r}_{tfp} - \vec{r}_e| \pm |\vec{r}_{fp} - \vec{r}_{tfp}|}{c} + \frac{|\vec{r}_r - \vec{r}_{fp}|}{c} \quad (2)$$

The transmit origin, $\vec{r}_e$ is the center element of the transmit sub-aperture. $\vec{r}_{tfp}$ and $\vec{r}_{fp}$ are the positions of the transmit focal point and the receive focusing point respectively. The ± in (2) refer to whether the FP is above or below the VS. With SASB the first stage beamformer has a fixed receive focus and the delay values, t_d are calculated in accordance with Fig. 2 (right)

$$\begin{aligned} t_{d_{fp}}(z_v) &= \frac{1}{c}(|\vec{r}_{tfp} - \vec{r}_e| \pm |\vec{r}_{fp} - \vec{r}_{tfp}| \pm |\vec{r}_{tfp} - \vec{r}_{fp}| + |\vec{r}_r - \vec{r}_{tfp}|) \\ &= \frac{1}{c}(2z_v \pm 2|\vec{r}_{tfp} - \vec{r}_{fp}|) \end{aligned} \quad (3)$$

where z_v is the distance from the aperture to the VS. With dynamic receive beamforming the differences between the individual channel delays changes with the position of the focusing point due to the term $|\vec{r}_r - \vec{r}_{fp}|$ in (2). A new set of delay values are, thus, calculated for each focusing point. With fixed receive focusing as in (3) only a single set of delay values is calculated and for each focusing point a constant is added. This is an important issue in respect to the complexity of the beamformer. With dynamic focusing the delay calculations involve among others the computational costly square root operation.

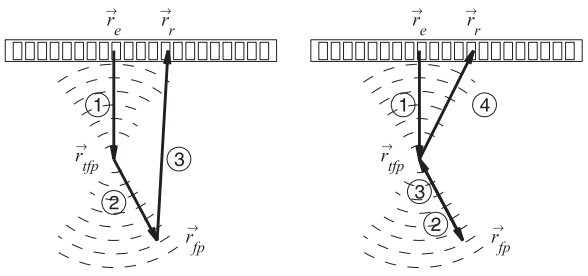

Fig. 2. Wave propagation path (solid line) for calculating the receive focusing time delays for a focused transmission. The center element of the transmitting aperture is perceived as the transmit origin. Dynamic receive focusing (left) and fixed receive focusing (right).

2.2. Two stage sequential beamforming

The objective of the proposed method is to obtain a synthetic transmit focus using data from multiple emissions but without storing the channel data. This is achieved in a two stage process. The 1st stage RF-lines, which are the output from the first beamformer, are obtained with a single focal point in both transmit and receive. This focal point is considered as a VS emitting a spherical wave front spatially confined by the opening angle. Each point in the 1st stage focused image line contains information from the arc of a circle that crosses that point. The arc has center in the focal point and is limited by the opening angle. This is illustrated in Fig. 3. Here it is also possible to see that the highlighted image point at $x = 0$ is represented in a phase-exact manner in multiple 1st stage lines obtained from multiple emissions. This means that the channel delay profile for focusing the highlighted image point using channel data from the first emission is exactly the same as the profile used for creating the highlighted point on the 1st stage line from the first emission. The profiles are the same since the image point is on the arc intersecting the point in the 1st stage line. This is also supported by the illustration in Fig. 2 (right). This characteristic is a consequence of the fixed receive focus and is exploited in the second stage. Here all the representations from different emissions of an image point (in form of samples from different 1st stage lines) are coherently added. A synthetic transmit focus is thus obtained without storing channel data. If the 1st stage is exchanged with a dynamically focused beamformer an image point is no longer exactly presented in any points of any 1st stage lines. The channel delay profile is unique for every point if dynamic focus is applied, which is also illustrated in Fig. 2 (left). Another consequence of having a dynamically focused beamformer in the 1st stage instead of a fixed focus beamformer is a large increase in implementation complexity which is discussed further in Section 2.3.

Each HRI consists of a number of high resolution image lines – the output lines from the 2nd stage beamformer. In this paper, N denotes the number of emissions, which is the same as the number of 1st stage lines and also the number of high resolution lines. The method has in principle no restrictions toward these numbers. Each sample in a high resolution line (HRL) is constructed in the second beamformer by selecting a sample from each of those 1st stage lines, which contain information from the spatial position of the image point and summing a weighted set of these samples.

The number of elements in the transmit sub-aperture, the depth of the focal point and, thus, the $F\#$ determines the opening angle,

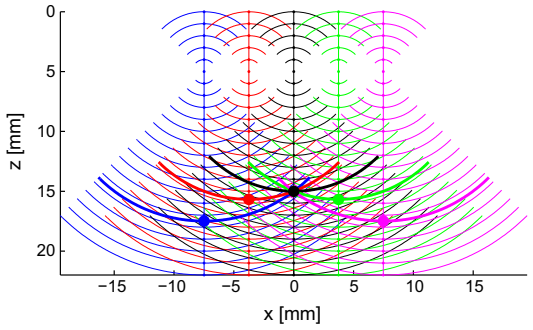

Fig. 3. Example of wave propagation and 1st stage image lines from 5 different emissions. Each point on the image lines contains information from the spatial positions which are indicated by the arc of a circle intersecting the point. A single high resolution image point of the SASB method is obtained by extracting information from all of those 1st stage image lines which contain information about that point.

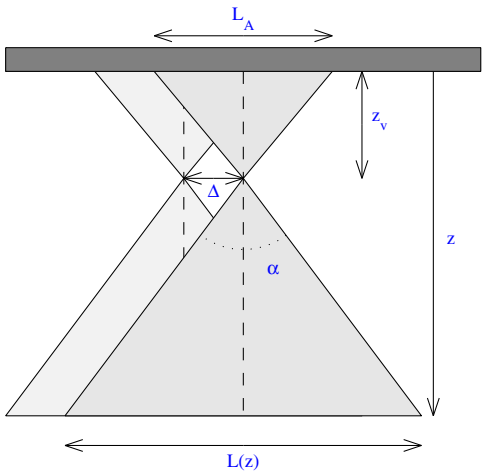

Fig. 4. Geometry model of the emitted wave fields from two consecutive emissions. The lateral width, $L(z)$ of the wave field at a depth, z determines the number of LRL's which can be added in the 2nd stage beamformer for an image point at depth, z.

hence the width of the transmitted wave field and the point spread function (PSF). As a consequence of the spatially limited wave propagation it must be determined for each image point in a HRL which emissions that have a wave field encompassing the image point. These emissions contribute to the HRL, and samples from each of them are selected according to the SAF delays, and added together. By definition a single HRL is composed of the sum of a number of low resolution lines (LRLs). A single LRL is, thus, the contribution from a given emission to a HRL.

The SAF can be formulated as a sum over LRL's. A single sample of the HRL, representing the image point at the location $\vec{r}_{ip}$ with lateral coordinate x and axial coordinate z, can be expressed as

$$h(x,z) = \sum_{k=1}^{K(z)} \mathcal{W}(x_k, z) l_{x_k}(z). \tag{4}$$

$h(x,z)$ is the HRL sample, and $l_{x_k}(z)$ is the LRL sample from the emission with lateral position x_k. The variable $\mathcal{W}$ is an apodization function with $K(z)$ values, which controls the weighting of the contribution from each of the LRL's. It is a function of the axial position of the image point, since the number of contributing emissions, $K(z)$ increases with the distance to the VS. K determines the number of VS's applied for a given HRI point and is a measure of the size of the synthesized aperture. $K(z)$ can be calculated directly from the geometry shown in Fig. 4 as

$$K(z) = \frac{L(z)}{\Delta} = \frac{2(|z - z_v|)\tan(\alpha/2)}{\Delta} \tag{5}$$

showing that K increases linearly with the distance to the virtual source. This facilitates a more range independent lateral resolution compared to DRF since contrary to DRF transmit focusing is also dynamic with the dynamic expansion of the size of the synthezized aperture, K. $L(z)$ is the lateral width of the wave field at a depth, z, and Δ is the distance between the VS's of two consecutive emissions. α is the opening angle of the VS and is the angular span for which the phase of the wave field can be considered constant. The opening angle can be expressed as

$$\alpha = 2\arctan\frac{1}{2F\#}, \tag{6}$$

which is a valid approximation [21]. With L_A denoting the size of the sub-aperture the F-number becomes $F\# = z_v/L_A$. The LRL can be formulated using the RF-line, $s_{x_k}(z')$

$$l_{x_k}(z) = s_{x_k}(z'). \tag{7}$$

z' is the axial position at which to select a sample from the RF-line. z' can be found from the distance function, $z' = d(\vec{r}_{v_{x_k}}, \vec{r}_{ip})/2$ which calculates the transmit-receive round trip travel path for the SAF, and thus the sample index for the RF-line, $s_{x_k}(z')$. The transducer elements are electronically focused at the VS at the position $\vec{r}_{v_{x_k}}$ with a focal distance of z_v from the aperture. The aperture is focused in both transmit and receive and the distance function becomes a sum of transmit and receive travel paths

$$d(\vec{r}_{v_{x_k}}, \vec{r}_{ip}) = 2z_v \pm 2|\vec{r}_{ip} - \vec{r}_{v_{x_k}}| \tag{8}$$

The ± in (8) refer to whether the image point is above or below the VS. A single sample of the HRL can thus be formulated using (4) and (7)

$$h(x,z) = \sum_{k=1}^{K(z)} \mathcal{W}(x_k, r) s_{x_k}(d(\vec{r}_{v_{x_k}}, \vec{r}_{ip})). \tag{9}$$

The formulation of the method in this section assumes an aperture with an infinite number of elements. This becomes apparent when observing (5). At greater depth $K(z)$ will exceed the number of available 1st stage lines, N. At depths beyond the point where $K(z) = N$ the synthesized aperture will no longer increase with depth. The $F\#$ will increase and the lateral resolution will no longer be range independent beyond that depth. Here it is also worth mentioning that as $K(z)$ increases the difference in acquisition time between the 1st stage lines applied increases and motion artifacts might become an issue. The synthesized aperture will also decrease for the HRL's near the edges, compared to the center HRL because of the limited number of 1st stage lines available. The lateral resolution is, thus, laterally dependent. The apodization function $\mathcal{W}$ is also laterally dependent and asymmetric.

The HRI is composed of a sum of LRI's from multiple transmissions as formulated in (9). The formulation assumes that the image object is stationary during all transmission, which is not the case in vivo. Tissue motion and motion artifacts are nevertheless not completely destructive to SA imaging. The susceptibility to motion of SA imaging has been investigated by several authors [22–30], and techniques to address the problems with tissue motion have been demonstrated.

2.3. Implementation

In SAF data from multiple emissions are applied. This could essentially decrease the image frame rate if a full set of emissions is needed to construct and update the HRI. Nikolov and Jensen proposed SA recursive imaging [31] to be able to construct a new frame after each emission. In SASB acquisition of a full set of N emissions is a necessity before the first HRI can be constructed, but by storing the M most recent 1st stage lines a new HRL can be constructed after each emission using the already stored lines and the newly acquired line. This is feasible by having a temporal offset between the reconstructed HRL and the acquired RF-line corresponding to M emissions. For HRI number i HRI_i the HRL's are numbered $J = 1, 2, \ldots N$. The corresponding RF-lines across the aperture are denoted $j = 1, 2, \ldots N$, and for HRI_{i+1} they are denoted $j = N+1, N+2, \ldots 2N$. The HRL J of HRI_k can be constructed while acquiring the RF-line, $j = J + M$. With M being equal to the number of available channels of the 2nd stage beamformer the temporal offset is minimized. Each 1st stage line makes a contribution to several HRL in the 2nd stage beamformer. All of these HRL can in principle be refreshed after each acquisition. This is solely determined by the capability of the 2nd stage beamformer to do parallel beamforming.

A view on implementation of the SASB at a block function level demonstrates a requirement for two beamformers and memory for storage of the 1st stage image lines to feed the 2nd stage beamformer. The 1st stage beamformer is simple since the receive delay-profiles are the same for all image points except for a depth dependent additive constant. It only requires calculation of a single profile or a look up table (LUT) with a single entry. It could easily be analog and thereby save many ADC's. The 2nd stage beamformer has the complexity of a general dynamic receive focusing beamformer. For each depth a separate entry in a LUT for a profile is required or the delay profile must be calculated. Apodization is also a desirable requirement for the 2nd stage beamformer to suppress off-axis energy lobes. Since $K(z)$ increases linearly with depth the apodization is dynamic. The apodization is also a function of the lateral position of the HRL due to the finite aperture and it can profitably be calculated as a parametric function. The desired number of channels of a single-beam beamformer in the 2nd stage equals the number of acquired 1st stage lines to synthesize the full size array. The channel count, C of the 2nd stage beamformer can be reduced though with a factor of M to $C = N/M$ using a M-beam beamformer capable of processing M parallel beams and an additional accumulation buffer for temporary output lines. In this form and in a case of N 1st stage lines (N acquisitions) and N 2nd stage lines the 2nd stage temporary output lines of the beamformer are $L_{out} = \mathrm{mod}([0{:}\,(M-1)]C + n - 1, N) + 1$ using the 1st stage lines for the input of the beamformer $L_{in} = \mathrm{mod}([0{:}\,(C-1)] + n - 1, N) + 1$ for beamforming operation n. After N operations each output line has been generated M times using M different sets of input signals (different virtual sources). By accumulating the M temporary output lines in the buffer the resulting output lines are exactly the same as if a single-beam N-channel beamformer is used.

3. Simulation results

In this section the method is investigated using simulations in Field II [18,19] and SAF is carried out using the Beamformation Toolbox, *BFT2* [20]. Images of point targets using different realizations of SASB are created. The axial and lateral resolution are extracted and compared to conventional B-mode imaging. The simulations are made with a model of a linear array 7 MHz transducer with properties similar to a commercial transducer.

3.1. Setup

The parameters, which are the most decisive for the performance of SASB are the focal depth z_v (the focal depth), and the $F\#$ of the VS. A parameter study is done by varying z_v with values of 5, 10, 15, 20 mm, and the $F\#$ with values in the range 0.5–2.5. The study is done with a default set of transducer parameters and processing parameters shown in Table 1.

In the main parameter study the value of $N_e = 401$ has been set to exclude the effects of a finite aperture to demonstrate the ability of the method to generate a range independent resolution. The number of 1st stage image lines and also 2nd stage image lines is the same as the number of transducer elements.

In this study a single cycle sinusoid is used as excitation and a weighted double cycle sinusoid is used to simulate the transducer impulse response. Another less extensive study is performed with more practical realizable parameters. The number of elements is $N = 191$. A double cycle sinusoid forms the excitation, and the measured impulse response of the applied transducer type is used. The scattering media consists of stationary point targets (PTs) placed in the center of the image in the range from 5 mm to 95 mm with a distance of 10 mm.

Table 1
Default values for the simulation parameter study.

Parameter		Value
Various		
Sampling frequency	f_s	120 MHz
Transducer		
Pitch	Δ	0.208 mm
Center frequency	f_c	7 MHz
Bandwidth, relative	B	0.6
Elevation focus	z_{ele}	25 mm
Number of elements	N	401
Excitation		1 Cycle sinusoid
1st Stage processing		
Focusing		Fixed, (xmt/rcv)
Number of channels, xmt/rcv	N_{1st}	63/63
Transmit sub-aperture		Symmetric only
Transmit apodization	$\mathcal{A}_{xmt}$	Hamming
Focal depth (virtual source)	z_v	5, 10, 15, 20 mm
Receive apodization	$\mathcal{A}_{rcv}$	Hamming
Receive sub-aperture		Same as transmit
Number of image lines	N	401
Distance between lines	Δ	0.208 mm
2nd Stage processing		
Focusing		Synthetic aperture
Number of channels	N_{2nd}	401
SA weighting	$\mathcal{W}$	Hamming
Number of image lines	N	401
Distance between lines	Δ	0.208 mm
Applied 1st stage lines		Symmetric only

3.2. Resolution study

Different realizations of SASB are simulated to evaluate performance and limitations. The position of the VS and the opening angle determines the image area covered by a single emission. If the covered area increases, the number of 1st stage lines, which can be used for the 2nd stage beamforming, also increases, yielding a larger synthesized aperture. This explicitly sets demands on the size of the array and the number of required 2nd stage beamformer channels if a range independent resolution is the objective. The study will show that other complications exist with the combination of a shallow focal depth and a large opening angle.

The log compressed envelope HRI's are shown in this section. The axial and lateral resolution are extracted at the image center for several depths. The resolution is quantified at −6 dB, the Full Width at Half Maximum (FWHM), and at −40 dB. For each PT the

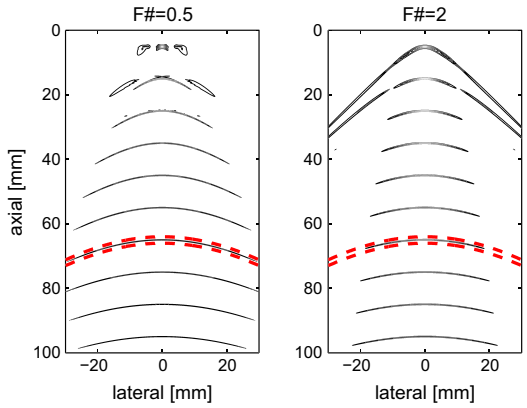

Fig. 5. Contour plots of the envelope of the output from the 1st stage beamformer. $F\# = 0.5$ (left), and $F\# = 2$ (right). The VS is at 5 mm. The curvature of the PSF is determined by the distance between the VS's and the point of the PSF. This is calculated analytically and shown as dotted lines for two points just above and below the PT at $z = 65$ mm.

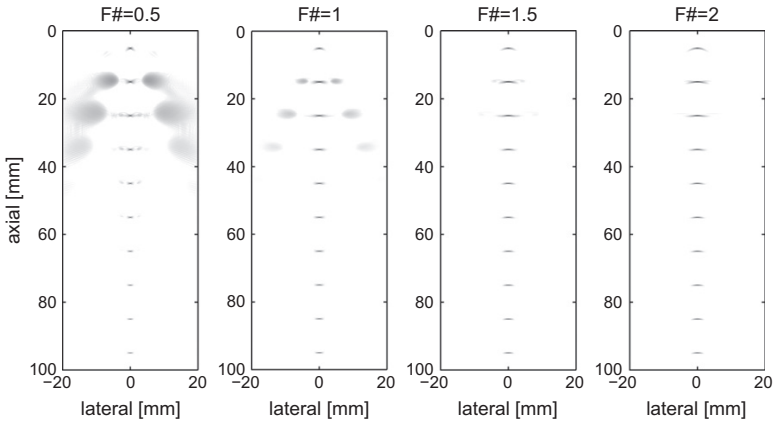

Fig. 6. SASB Images with the VS at 5 mm and with different values of *F#*. Dynamic Range is 60 dB.

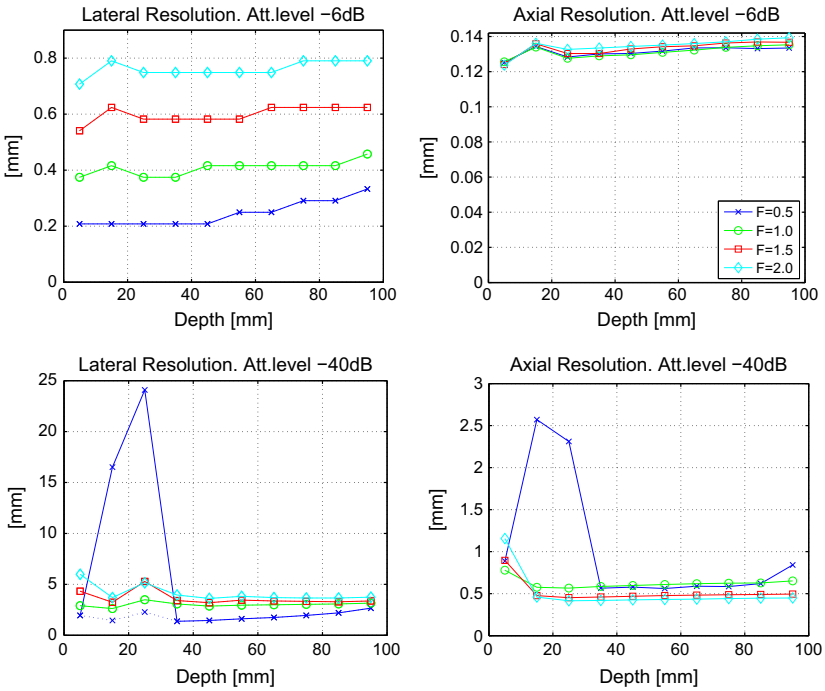

Fig. 7. Resolution as function of depth at −6 dB (top) and −40 dB (bottom). Lateral resolution (left) and axial resolution (right). If the lateral PSF has a distinct main-lobe and side-lobe distribution, the main-lobe resolution is shown as a dotted line. Shown for the four different setups represented in Fig. 6.

resolution is calculated as the width at which the envelope amplitude has decreased to the specified level relative to the maximum level at that given PT. For the lateral resolution the envelope amplitude is taken as the maximum amplitude within a axial range of ±3 mm around the PT. Likewise for the axial resolution the envelope amplitude is taken as the maximum amplitude across the entire lateral range of the image.

A poor lateral resolution is the consequence of having a PSF with a wide main lobe and/or high side-lobe levels. The illustrations of the quantified lateral resolution reflects this by also showing the main-lobe resolution as a dotted line, but only if the lateral PSF has a distinct main-lobe and side-lobe distribution. That is if the lateral PSF drops below the − 40 dB level and rises above this level again at a greater lateral position.

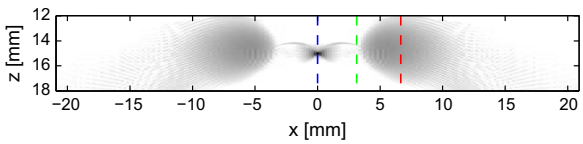

Fig. 8. A zoom in on the HRI shown in Fig. 6 for *F#* = 0.5. Three different HRL's are marked with dotted lines. The LRL's composing these HRL's are shown in Figs. 9–11.

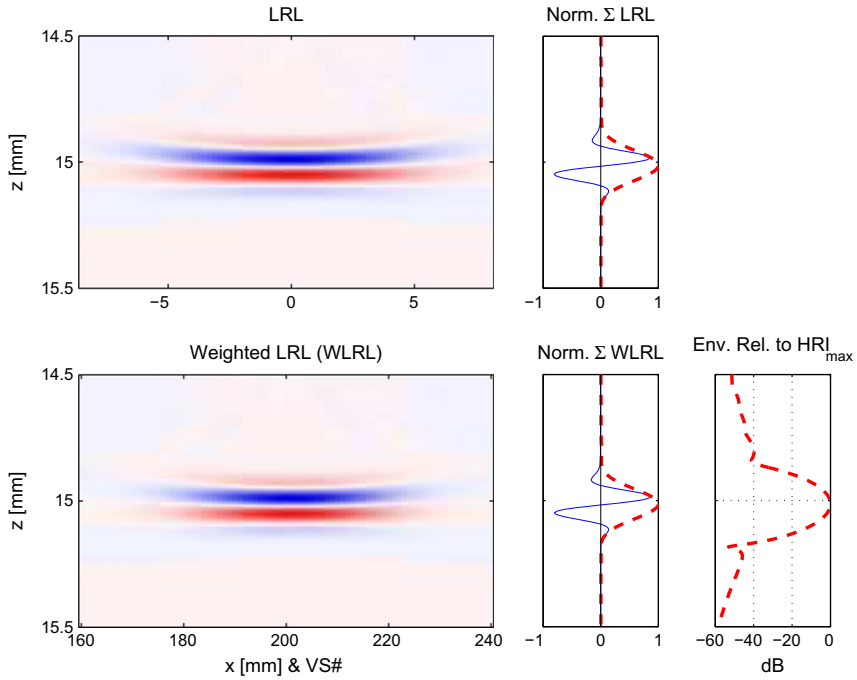

Fig. 9. The LRL's composing the center HRL of the HRI shown in Fig. 8. The LRL's are shown before and after the weighting function. The summation of the LRL's and the corresponding envelope are also shown.

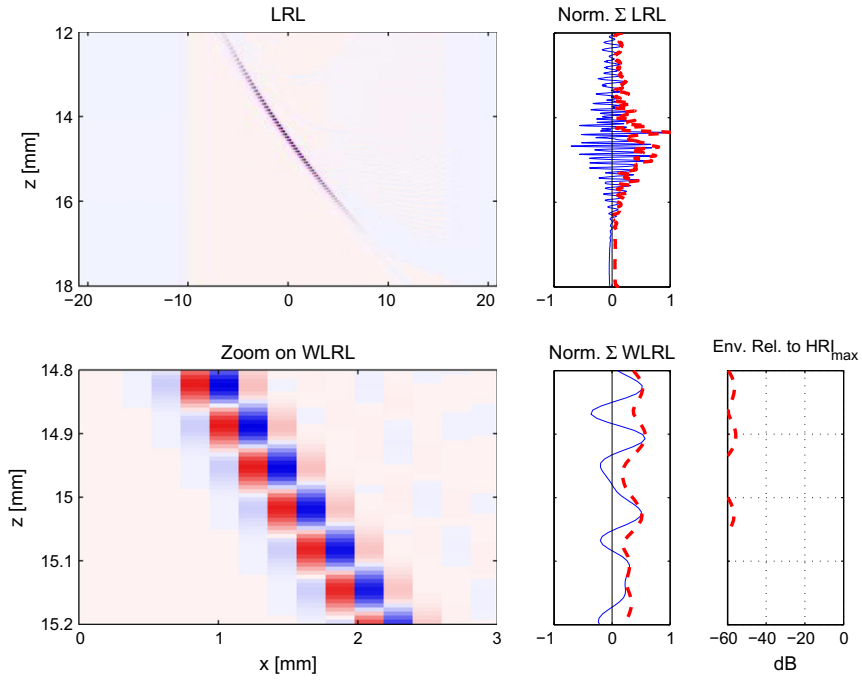

Fig. 10. The LRL's composing the off-center HRL at the lateral position $x = 3.1$ of the HRI shown in Fig. 8. A zoom in on a few of the weighted LRL's is shown to visualize destructive summation of the LRL's.

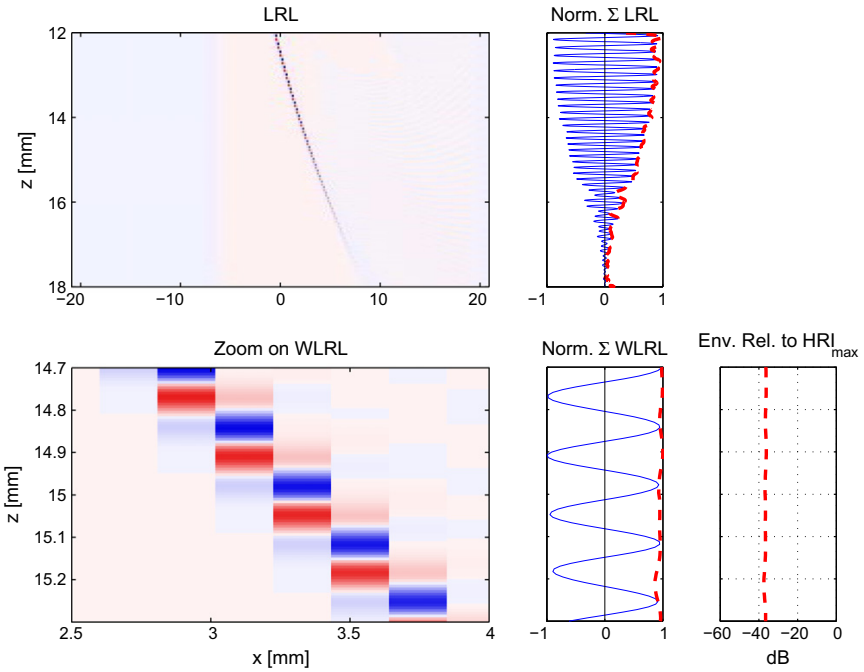

Fig. 11. The LRL's composing the off-center HRL at the lateral position $x = 6.7$ of the HRI shown in Fig. 8. A zoom in on a few of the weighted LRL's is shown to visualize a phase-shift of almost an entire pulse-echo wave length, yielding undesired constructive summation, and an envelope level above −40 dB.

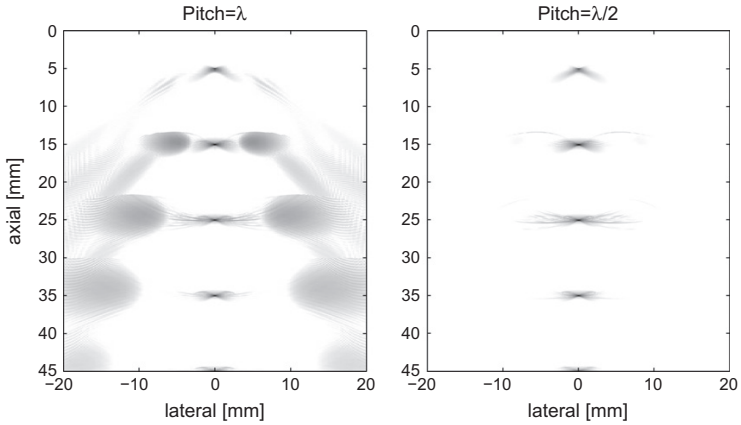

Fig. 12. Two SASB images are constructed using a linear array (left) and a linear phased array (right). Both having 401 elements, a VS at 5 mm, and with $F\# = 0.75$. The linear array is twice the width of the phased array, but the image has been cropped to the same width as the phased array image. Dynamic range is 70 dB.

The PSF at the output of the 1st stage beamformer has a large extent because of the fixed receive focusing. The curvature is determined by the distance between the VS's and the point of the PSF. Consider the point at position $\vec{r}_p = (x, z) = (0, z_p)$. The curvature, $z_c(x)$ is

$$z_c(n) = z_v \pm \sqrt{(z_p - z_v)^2 + (|n|\Delta)^2}. \tag{10}$$

The variable x has been substituted by $n\Delta$, where $-N/2 \leqslant n \leqslant N/2$ is the VS number counting from the VS at $x = 0$. The ± refer to whether the image point is above or below the VS, just as in (3), and (8). The contour plot of the PSF is shown in Fig. 5 with a VS at 5 mm and with $F\# = 0.5$, and $F\# = 2$. The shape of the PSF is the same in both cases, but the width of the PSF differs due to the different opening angles. $z_c(n)$ from (10) has been plotted on top of the contour plot to illustrate the coherence. A PT is placed at $z = 65$ mm and z_c has been plotted for two points at $z_p = 64$ mm and $z_p = 66$ mm, respectively. The curvatures of these plots are similar to the PSF.

The envelope images after 2nd stage processing of these data sets are shown in Fig. 6 with a 60 dB dynamic range. The images are constructed with $N = 401$ which equals an image width of approximately 83 mm, but the displayed images have been cropped to a width of 40 mm. The resolution seems range independent if the dominant side-lobes are discounted. The lateral

resolution decreases as the *F*# increases as expected because of the decrease in the width of the synthesized aperture.

The quantified resolution of the HRI in Fig. 6 is shown in Fig. 7. The resolution is practically constant at −6 dB and −40 dB through range for all values of *F*#, with a few exceptions. The exceptions are for those PT near the VS when *F*# = 0.5. Here the side-lobe level is very dominant. Side-lobes are also noticeable for *F*# = 1 when looking at the HRI in Fig. 6. They are below the −40 dB level though and do not show in Fig. 7.

3.2.1. Investigating grating-lobes

The off-axis energy-lobes in Fig. 6 for *F*# = 0.5 are dominant. Taking a closer look at the phase of those LRL's which are summed in the 2nd stage beamformer can disclose the origin of this artifact. The part of the image containing the PT at 15 mm is shown in Fig. 8. Three different HRL's are investigated. They are marked with dotted lines in Fig. 8. SASB relies on phase coherent addition of the LRL's as expressed in (4). The LRL's composing the center HRL are plotted in Fig. 9. It is apparent that the LRL's are completely phase aligned and add up constructively as expected. The figure shows the LRL's before and after the weighting function. It also shows the HRL, hence the summation of the LRL's and the corresponding envelope. Finally the envelope of the weighted HRL is shown relative to the maximum of the HRI in Fig. 8.

The LRL's composing the HRL at $x = 3.1$ mm are plotted in Fig. 10. The LRL's are shown before the weighting and a zoom in on a few of the LRL's after the weighting function is shown. The phase shift between consecutive LRL's is close to half a pulse-echo wave length and this destructive summation yields an envelope level near −60 dB.

The LRL's composing the HRL at $x = 6.7$ mm are plotted in Fig. 11. The phase shift between consecutive LRL's has increased to almost an entire pulse-echo wave length and the LRL's add up constructively to an envelope level above −40 dB. In this simulated setup the pulse-echo signal consists of only a few periods, hence only a few non-zero contributions are included in the summation of the LRL's. If the pulse-echo signal contains several periods several non-zero LRL's will be present in the sum, yielding an even higher envelope level.

The artifacts shown are grating lobes, since they arise due to lateral spatial under-sampling. Consider having a setup with a phased array transducer with a $\lambda/2$ pitch and, thus, twice the lateral density of VS's. The illustration of LRL's prior to summation equivalent to the one shown in Fig. 11 will contain LRL's with a phase shift between consecutive LRL's of only half a wave length. Every second LRL will be equal to the ones shown in Fig. 11 but every other LRL will have a phase which is in between the two. The result is destructive summation instead of unintentional constructive summation, and the massive grating lobes are avoided. This is exemplified in Fig. 12. Two HRI's are constructed using a linear array with λ-pitch and a linear phased array with $\lambda/2$-pitch respectively. The

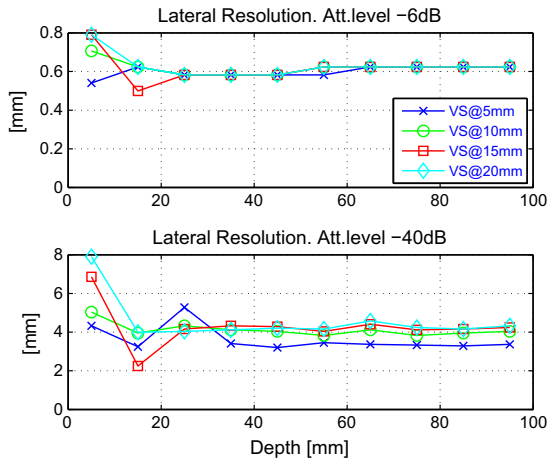

Fig. 14. Lateral resolution with *F*# = 1.5 as a function of depth at −6 dB (top) and −40 dB (bottom).

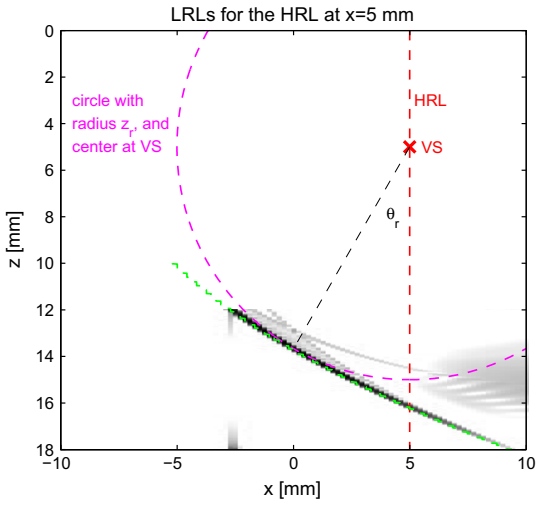

Fig. 13. The log-compressed envelope of the LRL's constituting the HRL at $x_h = 4$ mm is shown in the range 12–18 mm with a dynamic range of 50 dB. The VS is at the depth $z_v = 5$ mm and *F*# = 0.5. A PT is positioned at the point $\vec{r}_p = (x, y) = (0, z_p)$ with depth, $z_p = 15$ mm. The appearance of the LRL's for the off-center HRL can be approximated by a rotation of the LRL's of the center HRL. The center of rotation is the VS of the off-center HRL, and the rotation radius is $z_r = z_p - z_v$. The angle of rotation $\theta_r = \arcsin(x_h/z_r)$ is also indicated.

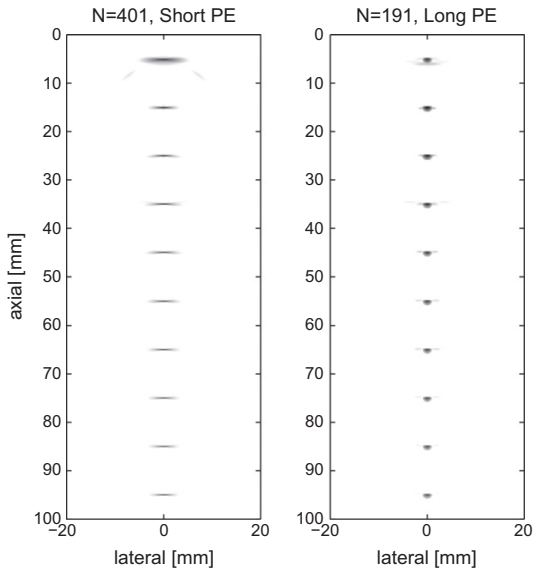

Fig. 15. Envelope images with the VS at 20 mm and with *F*# = 2. Two different simulation models are used. $N = 401$, and a short pulse-echo (PE) response (left). $N = 191$, and a long pulse-echo response (right). The image using $N = 401$ has been cropped to the same width as the image using $N = 191$. Dynamic range is 60 dB.

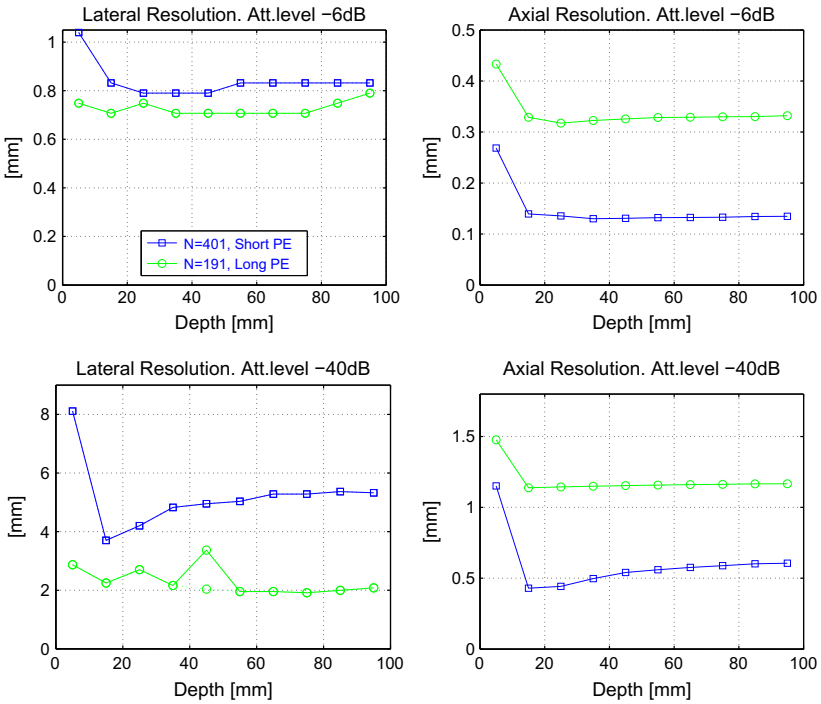

Fig. 16. Resolution as function of depth at −6 dB (top) and −40 dB (bottom). Lateral resolution (left) and axial resolution (right). If the lateral PSF has a distinct main-lobe, and side-lobe distribution, the main-lobe resolution is shown as a dotted line. The resolution is extracted from the HRI's in Fig. 15.

difference between the two images is striking, since the grating lobes are avoided by increasing the lateral spatial sampling in the 1st stage processing.

The VS's can be conceived as elements in a virtual array. In SASB the wave fields from several emissions are sampled by the virtual array and coherently added. For a given frequency grating lobes arise at a combination of a sparse spatial sampling by the virtual array and wave fields with incident angles beyond a certain limit. Both of these parameters can be controlled in SASB to prevent grating lobes. The array spacing and the VS spacing do not have to be the same. With a dense lateral sampling the VS can have $\lambda/2$ spacing even though the array has λ spacing. For a given spacing between the VS's the range of incident angles must be restricted. This is possible by putting a limit to the opening angle of the VS.

The restriction on the opening angle to avoid grating lobes can be demonstrated from an analysis of the LRL's constituting the off-center HRL's. In Fig. 9 the LRL's constituting the center HRL are phase-coherently aligned. They are aligned at the depth, $z_p = 15$ mm, where a PT at $\vec{r}_p = (x, y) = (0, z_p)$ is placed. In Fig. 11 the LRL's constituting an off-center HRL at the lateral position x_h are no longer aligned phase-coherently. As a simple approximation these LRL's can be found by a rotation of the aligned LRL's. The line of phase equality is perpendicular to the line with origin in the VS of the off-center HRL and going to $\vec{r}_p$ and with length $z_r = z_p - z_v$, where z_v is the depth of the VS. The angle of this line is

$$\theta_r = \arcsin\left(\frac{x_h}{z_r}\right). \tag{11}$$

This geometry is illustrated in Fig. 13 superimposed on the log-compressed envelope of a set of LRL's from the HRL at $x_h = 5$ mm. The exact positions of constant phase are also indicated in Fig. 13 as a dashed line. It comes from the intersections of the indices representing the PT and the indices representing a number of FP's all placed in the same off-center HRL.

By applying the approximation about the rotated LRL's it is possible to estimate the phase shift between consecutive LRL's with a simple expression. The axial shift between consecutive LRL's is

$$x = \tan\theta_r \Delta. \tag{12}$$

Substituting θ_r with half the opening angle, $\alpha' = \alpha/2$ the axial shift can be expressed as

$$x = \tan(\alpha')\Delta = \frac{\Delta}{2F\#}. \tag{13}$$

If the spatial shift does not exceed half the wavelength of the pulse-echo signal, $\lambda_{pe} = \lambda/2 = c/f_0/2$ grating lobes are avoided. That is

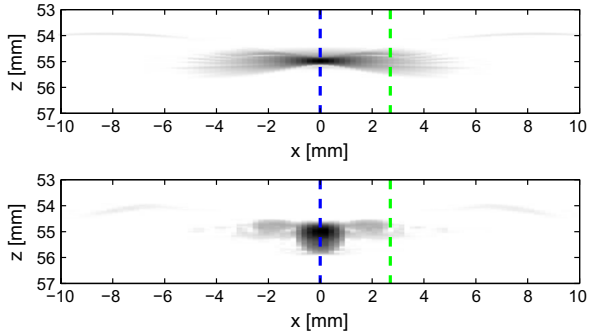

Fig. 17. Envelope images with the VS at 10 mm, and with $F\# = 2$ from Fig. 15. Short PE response (top), and long PE response (bottom). Shown in the range from 53 mm to 57 mm, and superimposed with vertical dashed lines indicating those HRL's for which the LRL's are shown. The LRL's are shown in Figs. 18 and 19.

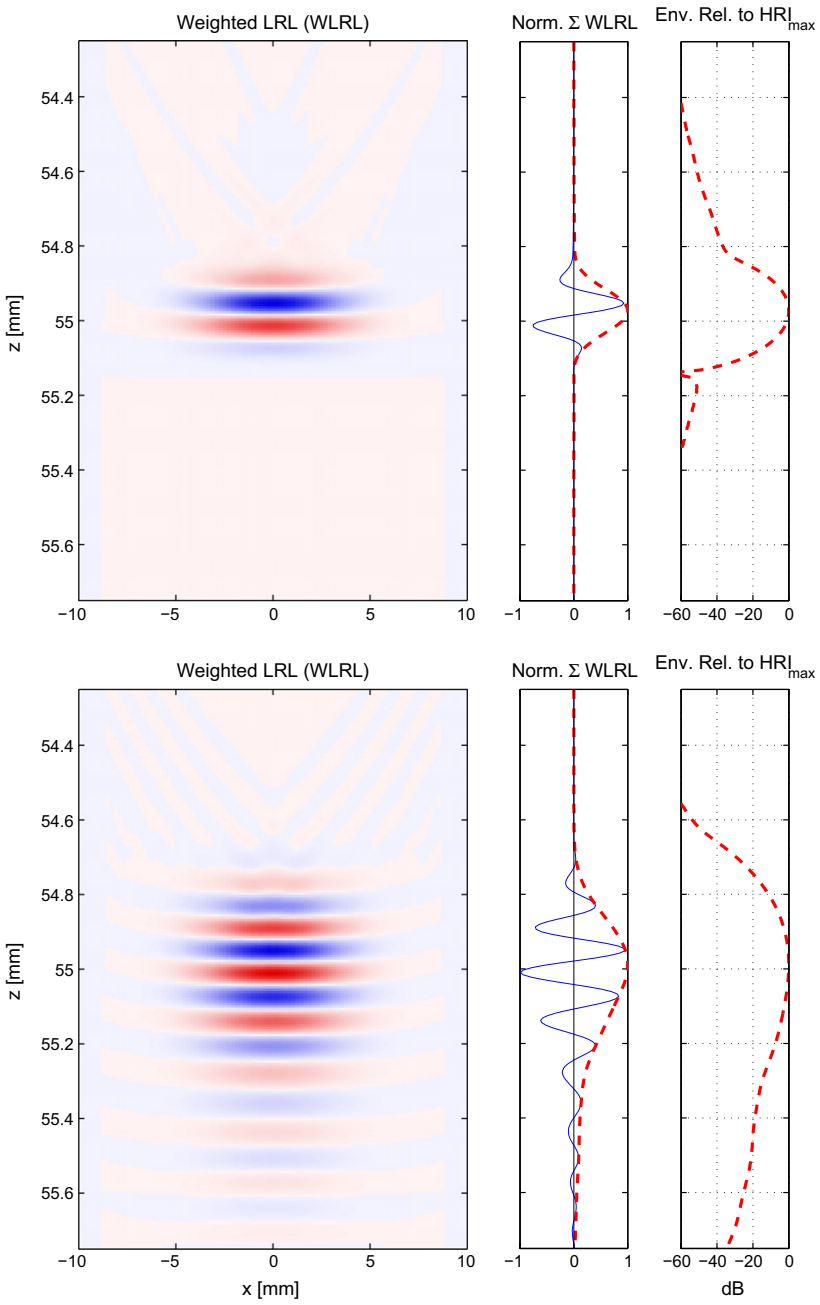

Fig. 18. The LRL's composing the center HRL of the two HRI's shown in Fig. 17. The LRL's are shown after the weighting function. The summation of the LRL's and the corresponding envelope are also shown.

$x < \lambda_{pe}/2$ or $x < \lambda/4$ This condition can be used to put restrictions on the $F\#$ of the VS

$$F\# \geqslant \frac{\Delta}{\lambda/2} \quad \text{for} \quad x \leqslant \lambda/4. \tag{14}$$

The opening angle of the VS limits the range of angles of the wave field. If a transducer with $\Delta = \lambda$ is used in SASB grating lobes are avoided if $F\# \geqslant 2$.

The spatial pulse-echo wavelength is extracted from the center LRL and is $\lambda_{pe} = 0.15$ mm. With $\Delta = 0.208$ mm the VS must be designed with $F\# \geqslant 1.39$ with the restriction of (14). This is also reflected in Fig. 6, where the grating lobes evidently are attenuated for $F\# = 1.5$ and $F\# = 2$ compared to the setup where $F\# = 0.5$, and $F\# = 1$. In Fig. 12 (right) a phased array with pitch $\Delta = 0.104$ is applied, which requires $F\# \geqslant 0.70$. The applied $F\#$ is 0.75 and the grating lobes are avoided. Notice that the requirement for the $F\#$ is not tied to the array spacing but to the spacing of the VS's. The

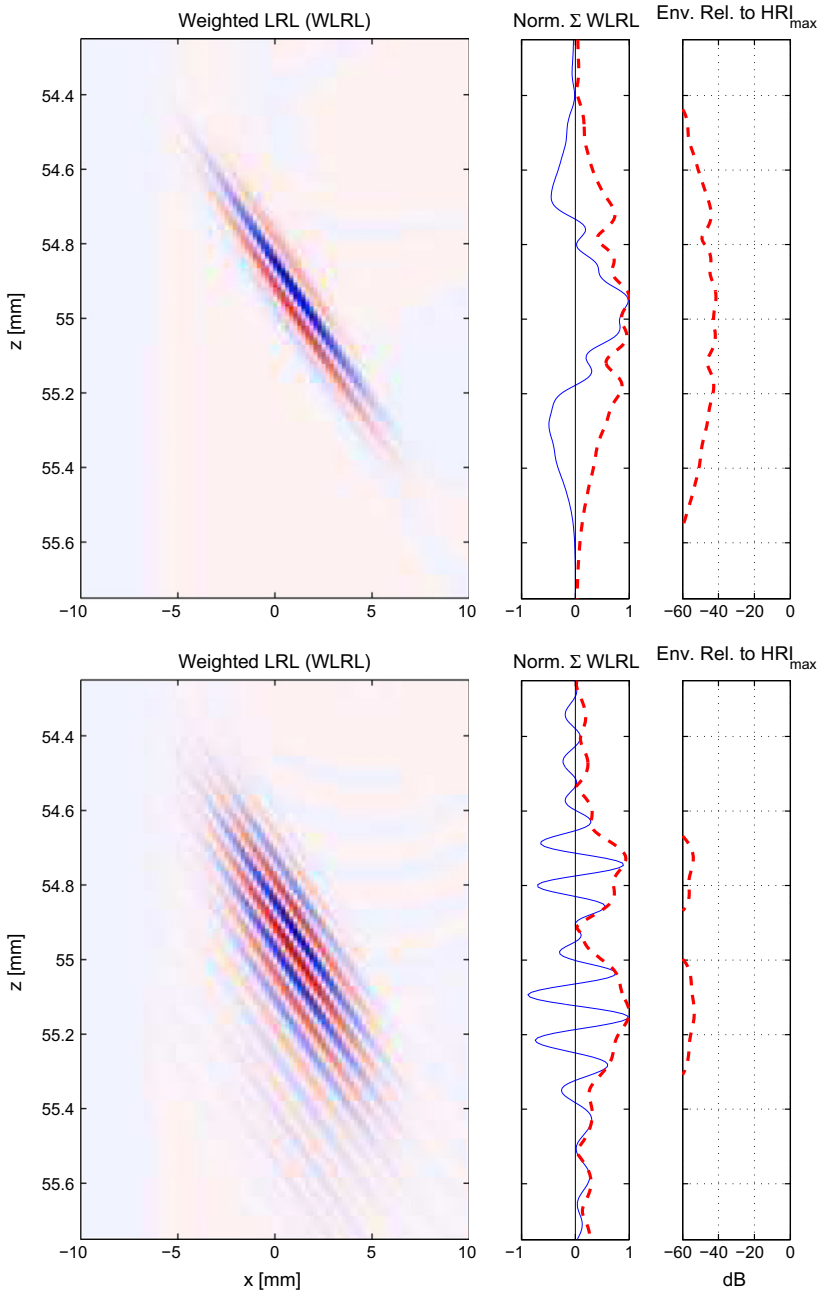

Fig. 19. The LRL's composing the off-center HRL of the two HRI's shown in Fig. 17. The LRL's are shown after the weighting function. The summation of the LRL's and the corresponding envelope are also shown.

setup is thus equivalent to a setup where $\Delta = 0.208$ and the density of the VS's is doubled.

$K(z)$ from (5) determines the number of VS's applied and the size of the synthesized aperture. It is a function of the position of the VS and the opening angle and, thus, the $F\#$. It was shown previously that the grating lobes were appropriately attenuated for the linear array with $F\# = 1.5$ when the VS was at 5 mm. The lateral resolution with $F\# = 1.5$ and different positions of the VS is shown

Table 2
The number of array elements used during transmission as a function of VS position and $F\#$.

VS depth	$F\# = 1.5$	$F\# = 2$
5 mm	17	13
10 mm	33	25
15 mm	49	37
20 mm	65	49

in Fig. 14. The resolution functions are very similar but not the same in the four different setups because of the different number of applied VS's.

3.2.2. Influence of transducer impulse response

The performance results presented in the previous sections were based on a transducer with $N = 401$, a short excitation signal, and a simple impulse response. The performance using a more realistic transducer simulation model is presented in this section and a comparison between the two is made. Envelope images with the VS at 20 mm, $F\# = 2$, and with the two different simulation models are shown in Fig. 15. The new simulation model has $N = 191$. The excitation signal has two periods, and the impulse response is the measured response of a commercial transducer yielding a longer pulse-echo (PE) response. The difference between the two images is significant. The axial resolution has decreased as a consequence of the extended PE response. The lateral resolution has improved in the entire range also beyond depths of 80 mm, where $K(z)$ ceases to increase linearly. The axial and lateral resolution are extracted, and shown in Fig. 16. The improvement in lateral resolution at −40 dB is at least a factor of 2.

To illustrate the cause of the difference in performance, the LRL's composing the HRI's are investigated. The investigation concerns only the range from 53 mm to 57 mm which include a single PT at a depth of 55 mm. The HRI's in this range are shown in Fig. 17, superimposed with vertical dashed lines indicating those HRL's for which the LRL's are shown.

The LRL's for the center HRL are shown in Fig. 18. The LRL's for the off-center HRL are shown in Fig. 19. In these figures the LRL's after LRL-weighting are shown. They also show the summation of the LRL's and the corresponding envelope. Finally the envelope of the weighted HRL is shown relative to the maximum of the HRI's in Fig. 17. The LRL's sum completely constructive for the center HRL in both setups.

For the off-center HRL's the LRL's sum destructively toward zero level. With a short pulse-echo response the off-center HRL is composed of the sum of a only a few positive and negative half-periods. The amplitudes of these half-periods varies with range and lateral position. The amplitude of the HRL, thus, varies with range. The variation over range is considerable due to the sparse number of cycles in the sum.

With a longer pulse-echo response the off-center HRL is composed of the sum of several positive and negative half-periods. The amplitudes of these half-periods decay smoothly over range and lateral position and on average sum destructively to a zero level. The HRL is of oscillating nature with the same center frequency as the pulse-echo response, which is not the case for the setup with the short PE response.

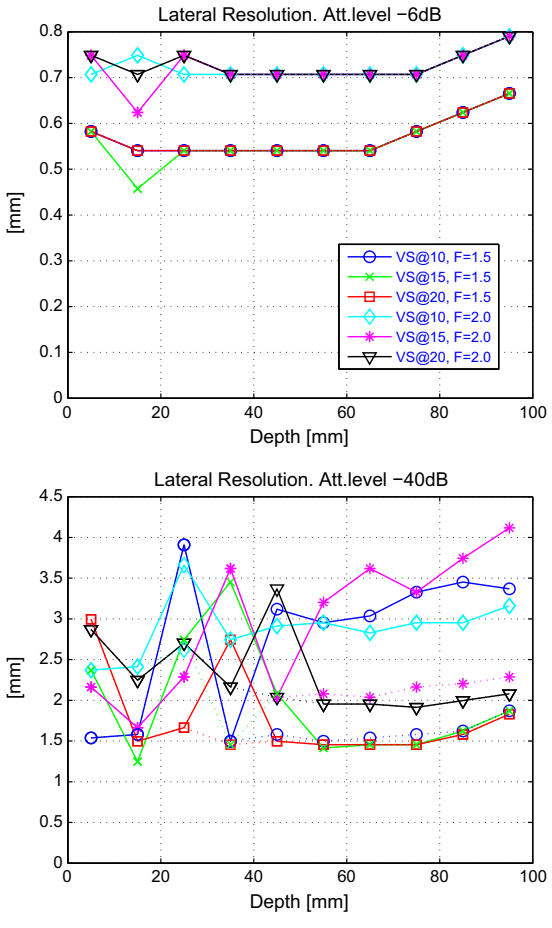

Fig. 20. Lateral resolution of SASB as function of depth at −6 dB (top) and −40 dB (bottom). If the lateral PSF has a distinct main-lobe, and side-lobe distribution, the main-lobe resolution is shown as a dotted line. In all configurations the results are based on the realistic transducer simulation model introduced in Section 3.2.2.

3.2.3. Comparison to dynamic receive focusing

The performance of SASB is among others a function of VS position and $F\#$. These parameters also determine the number of elements used during transmission. This has an influences on the emitted energy and the signal to noise ratio. It was shown in Section 3.2.1 that the grating lobes were appropriately attenuated for $F\# = 1.5$ and $F\# = 2$. The number of elements used as a function of VS position and $F\#$ is shown in Table 2.

The choice of configuration for comparison with DRF is based on the results presented in Fig. 20. Here the lateral resolution for a number of configurations is shown. In all configurations the results are based on the realistic transducer simulation model introduced

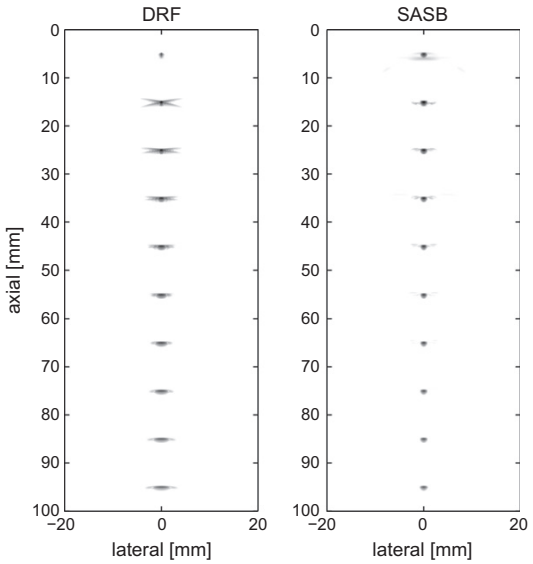

Fig. 21. Envelope images using DRF (left) and SASB (right). For DRF the transmit focal point is at 70 mm. For SASB the VS is at 20 mm and $F\# = 1.5$. Dynamic Range is 60 dB.

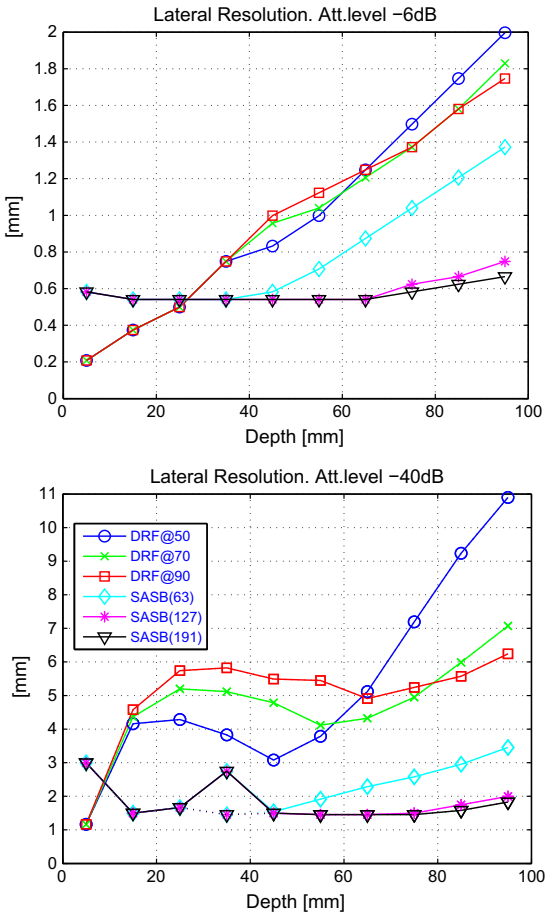

Fig. 22. Lateral resolution of DRF and SASB as function of depth at −6 dB (top) and −40 dB (bottom). If the lateral PSF has a distinct main-lobe, and side-lobe distribution, the main-lobe resolution is shown as a dotted line. In all configurations the results are based on the realistic transducer simulation model introduced in Section 3.2.2. For DRF the transmit focal point is at 50 mm, 70 mm, and 90 mm. For SASB the VS is at 20 mm and $F\#$ = 1.5. SASB results are presented using different number of available 2nd stage beamformer channels. N_{2nd} = 63, N_{2nd} = 127, and N_{2nd} = 191.

in Section 3.2.2. The performance with the VS at 20 mm and $F\#$ = 1.5 is superior to the other configurations in almost the entire range. It is thus a rational choice for a good performance and a comparison with DRF.

Fig. 21 shows images with DRF and SASB side by side, and Fig. 22 shows the quantified lateral resolution for different configurations. The quantified axial resolution does not differ between the different configurations and is not shown. Different positions of the transmit focal point in DRF has been applied for a fair comparison. The VS is at 20 mm and $F\#$ = 1.5 for all cases of SASB. In Fig. 21, and in the previous sections the number of channels in the 2nd stage beamformer is unlimited, so that $N_{2nd} = N$. In Fig. 22 additional SASB results are presented where the number of channels has been limited to N_{2nd} = 127, and N_{2nd} = 63.

There is an substantial improvement in resolution using SASB compared to DRF. It accounts for both the FWHM and the resolution at −40 dB. The improvement in FWHM is at least a factor of 2 and the improvement at −40 dB is at least a factor of 3. The improvement of SASB over DRF is a reality except for a few exceptions. At depths until 20 mm the FWHM is superior with DRF. With SASB the resolution is almost constant throughout the range. For DRF the FWHM increases almost linearly with range and the resolution at −40 dB is fluctuating with range.

By putting restrictions on the number of 2nd stage beamformer channels the system complexity is reduced. It will have a negative consequence on resolution, since the synthesized aperture decreases. When the number of channels is restricted to N_{2nd} = 63, and N_{2nd} = 127 then the depths at which $K(z)$ ceases to increase linearly is at 40 mm and 61 mm respectively. This is also apparent when observing the resolution in Fig. 22 when these restrictions are applied. Both the FWHM and the resolution at −40 dB cease to be constant at these depths. Even when the number of channels is restricted to N_{2nd} = 63 the performance of SASB is superior to DRF.

4. Measurement results

A commercial scanner and a linear array transducer with parameters similar to the ones in Table 1 have been used to acquire data. A tissue phantom with wire targets and 0.5 dB/MHz/cm attenuation is used as imaging object. RF-data using DRF and 1st stage SASB is acquired with a 5 MHz center frequency and stored. 2nd stage SASB processing, envelope detection, and logarithmic compression is done off-line for both DRF and SASB. An envelope image of the acquired 1st stage SASB data is shown in Fig. 23. It resembles the shape of the contours shown in Fig. 5 as expected. Notice the arcs are turned upside down before and after the focal point at 20 mm. A side by side comparison between the DRF image and the SASB image is also shown in Fig. 23. With DRF the transmit focal point is at 65 mm, and with SASB the VS is at 20 mm $F\#$ = 2.

The images based on measured data confirms the results from the simulations. At the center of the image the resolution of SASB is superior to DRF and is practically range independent. A zoom in on the PT at 69 mm for the DRF and SASB images from Fig. 23 is shown in Fig. 24. Here the difference in resolution is prominent. The resolution in the near field is slightly better for DRF as stated in Section 3.2.3 and in Fig. 22.

The speckle pattern is present at a greater range in the SASB image compared to the DRF image indicating greater penetration. At greater depths the emitted wave field in SASB is wide compared to DRF. The intensity is lower and so is the SNR of the 1st stage SASB-data. The SNR increases because of the summation of a number of LRL's. Provided that the image object does not move in between acquisitions and assuming uncorrelated electronic noise at the receivers the potential SNR improvement at the center HRL compared to 1st stage RF-data is $\Delta\, SNR(z) = 10\log_{10}(K(z))$ with a rectangular apodization in the 2nd stage. With an apodization function $\mathcal{W}$ the SNR improvement becomes

$$\Delta SNR(z) = 10\log_{10}\left(\sum_{k=1}^{K(z)} \mathcal{W}(x_k, z)\right). \tag{15}$$

The signal to noise ratio as a function of depth for a set of acquired DRF-data and a set of 1st stage SASB-data has been estimated, and is shown in Fig. 25. For DRF the transmit focus is at 45 mm and for SASB the VS is at 20 mm with $F\#$ = 2. 20 data sets have been acquired for both DRF and SASB using a tissue phantom with an attenuation of 0.5 dB/[MHz cm]. The signal part is estimated by averaging the measured signals. A set of noise signals is estimated by subtracting the estimated signal part from the measured signals. The SNR is

$$SNR(z) = \frac{\mathcal{E}\{Y(z)\}^2}{\mathcal{E}\{[Y(z) - \mathcal{E}\{Y(z)\}]\}^2} \simeq \frac{\left(\frac{1}{M}\sum_{m=1}^{M} y_m(z)\right)^2}{\frac{1}{M}\sum_{m=1}^{M}\left[y_m(z) - \frac{1}{M}\sum_{m=1}^{M} y_m(z)\right]^2}. \tag{16}$$

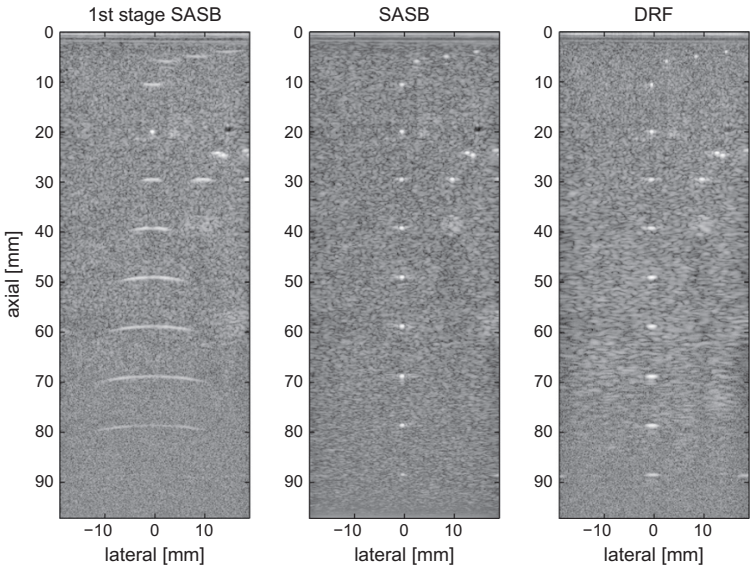

Fig. 23. Envelope images using 1st stage SASB (left), SASB (center), and DRF (right). RF-data is acquired using a commercial scanner, and processing is done off-line. For DRF the transmit focal point is at 65 mm. For SASB the VS is at 20 mm and $F\# = 2$. Dynamic Range is 60 dB.

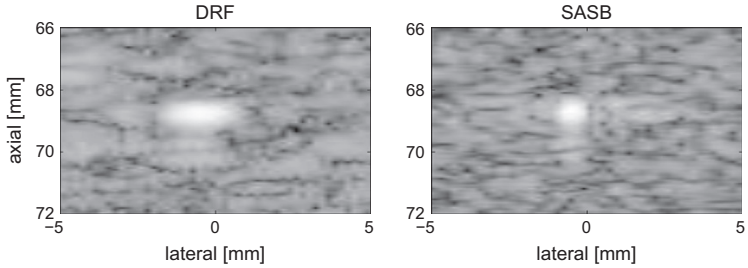

Fig. 24. A zoom in on the DRF and SASB images from Fig. 23.

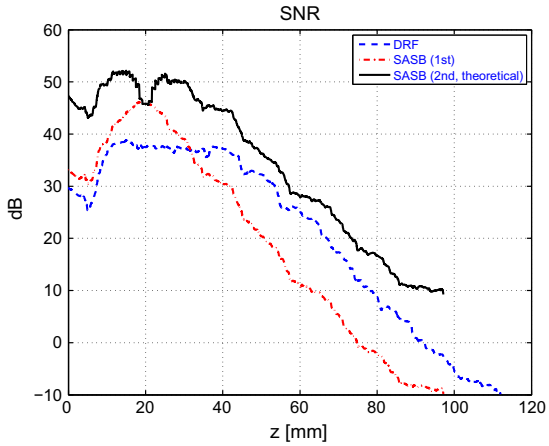

Fig. 25. SNR as a function of depth. Data sets are acquired with a commercial scanner and a tissue phantom for both DRF and 1 stage SASB. The estimated SNR of 2nd stage SASB is also shown.

$\mathcal{E}$ is the expectation operator. $Y(z)$ denotes the M number of measured data sets, and $y_m(z)$ is the m'th data set. The theoretical potential SNR improvement, $\Delta SNR(z)$ from (15) is also shown in Fig. 25 with a Hamming window as SA weighting. For $z = 80$ mm the value of $\Delta\, SNR(z)$ can be calculated using (6) and (5) and is 19 dB. The potential SNR of the SASB is superior to DRF at the entire range and an improvement of 8 dB is realized at a depth of 80 mm.

5. Conclusion

The main motivation for SASB is to apply synthetic aperture techniques with a restricted system complexity. The objective is to improve lateral resolution and obtain a more range independent resolution compared to conventional ultrasound imaging.

The SASB method has been investigated using simulations in Field II and by off-line processing of data acquired with a commercial scanner. The parameters which are the most decisive for the performance are the depth of the VS (the focal depth), and the $F\#$ of the VS. The lateral resolution increases with a decreasing $F\#$, but grating lobes arise at a combination of a sparse spatial sampling by the virtual array and wave fields with incident angles

beyond a certain limit. It is possible to restrict the range of incident angles by putting a limit to the opening angle of the VS. For a transducer with a pitch of $\Delta = \lambda$ grating lobes are avoided if $F\# \geqslant 2$. For a phased array transducer with $\Delta = \lambda/2$ grating lobes are avoided if $F\# \geqslant 1$.

Simulations have been done with two different pulse-echo responses having different bandwidths. The performance difference between the two simulation models is significant. The lateral resolution is significantly better for the simulation model with the longer pulse-echo response and the improvement is at least a factor of 2 at -40 dB.

The performance of SASB with the VS at 20 mm and $F\# = 1.5$ is compared with conventional dynamic receive focusing (DRF). The axial resolution is the same for the two methods. There is an substantial improvement in lateral resolution using SASB compared to DRF. It accounts for both the FWHM and the resolution at -40 dB. The improvement in FWHM is at least a factor of 2 and the improvement at -40 dB is at least a factor of 3. The improvement of SASB over DRF is a reality except for a few exceptions. At depths until 20 mm the FWHM is superior with DRF. With SASB the resolution is almost constant throughout the range. For DRF the FWHM increases almost linearly with range and the resolution at -40 dB is fluctuating with range. By putting restrictions on the number of 2nd stage beamformer channels the system complexity is reduced. It will have a negative consequence on resolution since the synthesized aperture decreases, but even when the number of channels is restricted to $N_{2nd} = 63$ the performance of SASB is still superior to DRF.

SASB has been applied to data acquired with a commercial scanner and a tissue phantom with wire targets. The images confirms the results from the simulations. At the center of the image the resolution of SASB is superior to DRF and is practically range independent. The resolution in the near field is slightly better for DRF. A feasible solution could be to construct the final image by applying DRF above the VS and SASB beyond the VS.

The speckle pattern is present at a greater range in the SASB image compared to the DRF image indicating greater penetration. The signal to noise ratio as a function of depth for a set of acquired DRF-data and a set of 1st stage SASB-data has been estimated. The theoretical potential improvement in SNR of SASB over DRF has been estimated based on the measured SNR data and an assumption of a stationary image object, and a correct phase-alignment in the 2nd stage beamformer. The improvement is attained at the entire range and at a depth of 80 mm the improvement is 8 dB.

References

[1] L.J. Cutrona, W.E. Vivian, E.N. Leith, G.O. Hall, A high resolution radar combat-surveillance system, IRE Trans. Mil. Elect. MIL-5 (1961) 127–131.
[2] C.W. Sherwin, J.P. Ruina, D. Rawcliffe, Some early developments in synthetic aperture radar systems, IRE Trans. Mil. Elect. MIL-6 (1962) 111–115.
[3] J.C. Curlander, R.N. McDonough, Synthetic Aperture Radar: Systems and Signal Processing, John Wiley & Sons Inc., 1991.
[4] M. Karaman, P.C. Li, M. O'Donnell, Synthetic aperture imaging for small scale systems, IEEE Trans. Ultrason. Ferroelec. Freq. Contr. 42 (1995) 429–442.
[5] R.Y. Chiao, L.J. Thomas, S.D. Silverstein, Sparse array imaging with spatially-encoded transmits, in: Proc. IEEE Ultrason. Symp. 1997, pp. 1679–1682.
[6] J.T. Ylitalo, H. Ermert, Ultrasound synthetic aperture imaging: monostatic approach, IEEE Trans. Ultrason. Ferroelec. Freq. Contr. 41 (1994) 333–339.
[7] M.H. Pedersen, K.L. Gammelmark, J.A. Jensen, In-vivo evaluation of convex array synthetic aperture imaging, Ultrasound Med. Biol. 33 (2007) 37–47.
[8] D.K. Peterson, G.S. Kino, Real-time digital image reconstruction: a description of imaging hardware and an analysis of quantization errors, IEEE Trans. Son. Ultrason. 31 (1984) 337–351.
[9] G.R. Lockwood, J.R. Talman, S.S. Brunke, Real-time 3-D ultrasound imaging using sparse synthetic aperture beamforming, IEEE Trans. Ultrason. Ferroelec. Freq. Contr. 45 (1998) 980–988.
[10] C.R. Hazard, G.R. Lockwood, Theoretical assessment of a synthetic aperture beamformer for real-time 3-D imaging, IEEE Trans. Ultrason. Ferroelec. Freq. Contr. 46 (1999) 972–980.
[11] M. O'Donnell, L.J. Thomas, Efficient synthetic aperture imaging from a circular aperture with possible application to catheter-based imaging, IEEE Trans. Ultrason. Ferroelec. Freq. Contr. 39 (1992) 366–380.
[12] C. Passmann, H. Ermert, A 100-MHz ultrasound imaging system for dermatologic and ophthalmologic diagnostics, IEEE Trans. Ultrason. Ferroelec. Freq. Contr. 43 (1996) 545–552.
[13] C.H. Frazier, W.D. O'Brien, Synthetic aperture techniques with a virtual source element, IEEE Trans. Ultrason. Ferroelec. Freq. Contr. 45 (1998) 196–207.
[14] S.I. Nikolov, J.A. Jensen, Virtual ultrasound sources in high-resolution ultrasound imaging, in: Proc. SPIE – Progress in biomedical optics and imaging, vol. 3, 2002, pp. 395–405.
[15] S.I. Nikolov, J.A. Jensen, 3D synthetic aperture imaging using a virtual source element in the elevation plane, in: Proc. IEEE Ultrason. Symp. vol. 2, 2000, pp. 1743–1747.
[16] M.H. Bae, M.K. Jeong, A study of synthetic-aperture imaging with virtual source elements in B-mode ultrasound imaging systems, IEEE Trans. Ultrason. Ferroelec. Freq. Contr. 47 (2000) 1510–1519.
[17] J. Kortbek, J.A. Jensen, K.L. Gammelmark, Synthetic aperture focusing applied to imaging using a rotating single element transducer, in: Proc. IEEE Ultrason. Symp. 2007, pp. 1504–1507.
[18] J.A. Jensen, N.B. Svendsen, Calculation of pressure fields from arbitrarily shaped, apodized, and excited ultrasound transducers, IEEE Trans. Ultrason. Ferroelec. Freq. Contr. 39 (1992) 262–267.
[19] J.A. Jensen, Field: a program for simulating ultrasound systems, Med. Biol. Eng. Comp. 10th Nordic-Baltic Conference on Biomedical Imaging 4(Supplement 1, Part 1) (1996b) 351–353.
[20] J. Kortbek, S.I. Nikolov, J.A. Jensen, Effective and versatile software beamformation toolbox, in: Proc. SPIE – Medical Imaging – Ultrasonic Imaging and Signal Processsing, vol. 651319, 2007, pp. 1–10.
[21] N. Oddershede, J.A. Jensen, Effects influencing focusing in synthetic aperture vector flow imaging, IEEE Trans. Ultrason. Ferroelec. Freq. Contr. 54 (2007) 1811–1825.
[22] L.F. Nock, G.E. Trahey, Synthetic receive aperture imaging with phase correction for motion and for tissue inhomogenities – Part I: basic principles, IEEE Trans. Ultrason. Ferroelec. Freq. Contr. 39 (1992) 489–495.
[23] G.E. Trahey, L.F. Nock, Synthetic receive aperture imaging with phase correction for motion and for tissue inhomogenities – Part II: effects of and correction for motion, IEEE Trans. Ultrason. Ferroelec. Freq. Contr. 39 (1992) 496–501.
[24] H.Ş. Bilge, M. Karaman, M. O'Donnell, Motion estimation using common spatial frequencies in synthetic aperture imaging, in: Proc. IEEE Ultrason. Symp. 1996, pp. 1551–1554.
[25] M. Karaman, H.Ş. Bilge, M. O'Donnell, Adaptive multi-element synthetic aperture imaging with motion and phase aberration correction, IEEE Trans. Ultrason. Ferroelec. Freq. Contr. 42 (1998) 1077–1087.
[26] C.R. Hazard, G.R. Lockwood, Effects of motion artifacts on a synthetic aperture beamformer for real-time 3D ultrasound, in: Proc. IEEE Ultrason. Symp. 1999, pp. 1221–1224.
[27] J.S. Jeong, J.S. Hwang, M.H. Bae, T.K. Song, Effects and limitations of motion compensation in synthetic aperture techniques, in: Proc. IEEE Ultrason. Symp. 2000, pp. 1759 –1762.
[28] S.I. Nikolov, J.A. Jensen, K-space model of motion artifacts in synthetic transmit aperture ultrasound imaging, in: Proc. IEEE Ultrason. Symp. 2003, pp. 1824–1828.
[29] K.L. Gammelmark, J.A. Jensen, Multielement synthetic transmit aperture imaging using temporal encoding, IEEE Trans. Med. Imag. 22 (2003) 552–563.
[30] K.L. Gammelmark, J.A. Jensen, Duplex synthetic aperture imaging with tissue motion compensation, in: Proc. IEEE Ultrason. Symp. 2003, pp. 1569–1573.
[31] S.I. Nikolov, K. Gammelmark, J.A. Jensen, Recursive ultrasound imaging, in: Proc. IEEE Ultrason. Symp. vol. 2, 1999, pp. 1621–1625.

BIBLIOGRAPHY

[1] M. E. Anderson, N. Bottenus, and G. E. Trahey. *A seminar on k-space applied to medical ultrasound*. Dept. of Biomedical Engineering, Duke University, 2015.

[2] J. A. Jensen. Linear description of ultrasound imaging systems, notes for the international summer school on advanced ultrasound imaging. Technical report, Department of Information Technology, DTU, 1999.

[3] J. A. Jensen. *Imaging in medical diagnosis and therapy*, volume 3, chapter Ultrasound Velocity Imaging, pages 65–99. CRC Taylor and Francis Group, 2015. 2015; 3.

[4] J. A. Jensen, S. Nikolov, K. L. Gammelmark, and M. H. Pedersen. Synthetic aperture ultrasound imaging. *Ultrasonics*, 44:e5–e15, 2006.

[5] J. Kortbek, J. A. Jensen, and K. L. Gammelmark. Sequential beamforming for synthetic aperture imaging. *Ultrasonics*, 53(1):1–16, 2013.

[6] J. A. Jensen. A model for the propagation and scattering of ultrasound in tissue. *J. Acoust. Soc. Am.*, 89:182–191, 1991.

[7] J. A. Jensen. A new calculation procedure for spatial impulse responses in ultrasound. *J. Acoust. Soc. Am.*, 105(6):3266–3274, 1999.

[8] J. A. Jensen, D. Gandhi, and W. D. O'Brien. Ultrasound fields in an attenuating medium. In *Proc. IEEE Ultrason. Symp.*, pages 943–946, 1993.

[9] J. A. Jensen. *Estimation of Blood Velocities Using Ultrasound: A Signal Processing Approach*. Cambridge University Press, New York, 1996.

[10] A. D. Pierce. *Acoustics, An Introduction to Physical Principles and Applications*. Acoustical Society of America, New York, 1989.

[11] P. M. Morse and K. U. Ingard. *Theoretical Acoustics*. McGraw-Hill, New York, 1968.

[12] P. R. Stepanishen. Pulsed transmit/receive response of ultrasonic piezoelectric transducers. *J. Acoust. Soc. Am.*, 69:1815–1827, 1981.

[13] L. E. Kinsler, A. R. Frey, A. B. Coppens, and J. V. Sanders. *Fundamentals of Acoustics*. John Wiley & Sons, New York, third edition, 1982.

[14] P. R. Stepanishen. Wide bandwidth near and far field transients from baffled pistons. In *Proc. IEEE Ultrason. Symp.*, pages 113–118, 1977.

[15] L. Raade and B. Westergreen. *β Mathematics handbook*. Charwell-Bratt, Ltd., Kent, England, 1990.

[16] M. R. Spiegel. *Mathematical handbook of formulas and tables*. McGraw-Hill, New York, 1968.

[17] M. Arditi, F. S. Forster, and J. Hunt. Transient fields of concave annular arrays. *Ultrason. Imaging*, 3:37–61, 1981.

[18] A. Penttinen and M. Luukkala. The impulse response and nearfield of a curved ultrasonic radiator. *J. Phys. D: Appl. Phys.*, 9:1547–1557, 1976.

[19] J. C. Lockwood and J. G. Willette. High-speed method for computing the exact solution for the pressure variations in the nearfield of a baffled piston. *J. Acoust. Soc. Am.*, 53:735–741, 1973.

[20] J. L. S. Emeterio and L. G. Ullate. Diffraction impulse response of rectangular transducers. *J. Acoust. Soc. Am.*, 92:651–662, 1992.

[21] J. A. Jensen. Ultrasound fields from triangular apertures. *J. Acoust. Soc. Am.*, 100(4):2049–2056, 1996.

[22] W. H. Press, B. P. Flannery, S. A. Teukolsky, and W. T. Vetterling. *Numerical recepies in C. The art of scientific computing*. Cambridge University Press, Cambridge, 1988.

[23] G. R. Harris. Transient field of a baffled planar piston having an arbitrary vibration amplitude distribution. *J. Acoust. Soc. Am.*, 70:186–204, 1981.

[24] P. R. Stepanishen. Acoustic transients from planar axisymmetric vibrators using the impulse response approach. *J. Acoust. Soc. Am.*, 70:1176–1181, 1981.

[25] J. Naze Tjøtta and S. Tjøtta. Nearfield and farfield of pulsed acoustic radiators. *J. Acoust. Soc. Am.*, 71:824–834, 1982.

[26] J. W. Goodman. *Introduction to Fourier optics*. McGraw Hill Inc., New York, second edition, 1996.

[27] J.C. Gore and S. Leeman. Ultrasonic backscattering from human tissue: A realistic model. *Phys. Med. Biol.*, 22:317–326, 1977.

[28] M. Fatemi and A.C. Kak. Ultrasonic b-scan imaging: Theory of image formation and a technique for restoration. *Ultrason. Imaging*, 2:1–47, 1980.

[29] L.A. Chernov. *Wave propagation in a random medium*. Academic Press, 1960.

[30] S. Leeman, V.C. Roberts, P.E. Chandler, and L.A. Ferrari. Inverse imaging with strong multiple scattering. In *Mathematics and computer science in medical imaging*. Springer-Verlag, 1988.

[31] G. E. Tupholme. Generation of acoustic pulses by baffled plane pistons. *Mathematika*, 16:209–224, 1969.

[32] P. R. Stepanishen. The time-dependent force and radiation impedance on a piston in a rigid infinite planar baffle. *J. Acoust. Soc. Am.*, 49:841–849, 1971.

[33] Philip M. Morse and Herman Feshbach. *Methods of theoretical physics, part I*. McGraw-Hill, New York, 1953.

[34] P. R. Stepanishen. Transient radiation from pistons in an infinite planar baffle. *J. Acoust. Soc. Am.*, 49:1629–1638, 1971.

[35] A. C. Kak and K. A. Dines. Signal processing of broadband pulse ultrasound: measurement of attenuation of soft biological tissues. *IEEE Trans. Biomed. Eng.*, BME-25:321–344, 1978.

[36] K. V. Gurumurthy and R. M. Arthur. A dispersive model for the propagation of ultrasound in soft tissue. *Ultrason. Imaging*, 4:355–377, 1982.

[37] J. A. Jensen and P. Munk. Computer phantoms for simulating ultrasound B-mode and CFM images. In S. Lees and L. A. Ferrari, editors, *Acoustical Imaging*, volume 23, pages 75–80, 1997.

[38] J. A. Jensen. Field: A program for simulating ultrasound systems. *Med. Biol. Eng. Comp.*, 10th Nordic-Baltic Conference on Biomedical Imaging, Vol. 4, Supplement 1, Part 1:351–353, 1996.

[39] R. F. Wagner, S. W. Smith, J. M. Sandrick, and H. Lopez. Statistics of speckle in ultrasound B-scans. *IEEE Trans. Son. Ultrason.*, 30:156–163, 1983.

[40] D. H. Evans, W. N. McDicken, R. Skidmore, and J. P. Woodcock. *Doppler Ultrasound, Physics, Instrumentation, and Clinical Applications*. John Wiley & Sons, New York, 1989.

[41] D. H. Evans and W. N. McDicken. *Doppler Ultrasound, Physics, Instrumentation, and Signal Processing*. John Wiley & Sons, New York, 2000.

[42] T. L. Szabo. *Diagnostic ultrasound imaging inside out*. Elsevier, 2004.

[43] R. S. C. Cobbold. *Foundations of Biomedical Ultrasound*. Oxford University Press, 2006.

[44] W. W. Nichols and M. F. O'Rourke. *McDonald's Blood Flow in Arteries, Theoretical, Experimental and Clinical Principles*. Lea & Febiger, Philadelphia, 1990.

[45] C. G. Caro, T. J. Pedley, R. C. Schroter, and W. A. Seed. *Cardiovascular Physiology*, volume 1 of *MTP international review of science Physiology. Series 1*, chapter Mechanics of the circulation, pages 15–48. Medical and Technical Publishers, London: Butterworth; Baltimore: University Park Press, 1974.

[46] D. W. Holdsworth, C. J. D. Norley, R. Fraynek, D. A. Steinman, and B. K. Rutt. Characterization of common carotid artery blood-flow waveforms in normal human subjects. *Physiol. Meas.*, 20:219–240, 1999.

[47] E. L. Carstensen, K. Li, and H. P. Schwan. Determination of the acoustic properties of blood and its components. *J. Acoust. Soc. Am.*, 25:286–289, 1953.

[48] F. Dunn, P. D. Edmonds, and W. J. Fry. Absorption and dispersion of ultrasound in biological media. In *Biological Engineering*. McGraw-Hill, New York, 1969.

[49] R. J. Ulrick. A sound velocity method for determining the compressibility of finely divided substances. *J. Applied Phys.*, 18:983–987, 1947.

[50] W. R. Platt. *Color Atlas and Textbook of Hematology*. J. B. Lippincott, Toronto, 1969.

[51] L. Y. L. Mo and R. S. C. Cobbold. Theoretical models of ultrasonic scattering in blood. In *Ultrasonic Scattering in Biological Tissues*. CRC Press, Boca Raton, Fla., 1993.

[52] G. S. Kino. *Acoustic Waves, Devices, Imaging, & Analog Signal Processing*. Prentice-Hall, Englewood Cliffs, N.J., 1987.

[53] O. Bonnefous and P. Pesqué. Time domain formulation of pulse-Doppler ultrasound and blood velocity estimation by cross correlation. *Ultrason. Imaging*, 8:73–85, 1986.

[54] O. Bonnefous, P. Pesqué, and X. Bernard. A new velocity estimator for color flow mapping. In *Proc. IEEE Ultrason. Symp.*, pages 855–860, 1986.

[55] J. A. Jensen and N. B. Svendsen. Calculation of pressure fields from arbitrarily shaped, apodized, and excited ultrasound transducers. *IEEE Trans. Ultrason., Ferroelec., Freq. Contr.*, 39:262–267, 1992.

[56] J. R. Womersley. Oscillatory motion of a viscous liquid in a thin-walled elastic tube. I: The linear approximation for long waves. *Phil. Mag.*, 46:199–221, 1955.

[57] D. H. Evans. Some aspects of the relationship between instantaneous volumetric blood flow and continuous wave Doppler ultrasound recordings III. *Ultrasound Med. Biol.*, 8:617–623, 1982.

[58] A. Swillens, L. Løvstakken, J. Kips, H. Torp, and P. Segers. Ultrasound simulation of complex flow velocity fields based on computational fluid dynamics. *IEEE Trans. Ultrason., Ferroelec., Freq. Contr.*, 56(3):546–556, 2009.

[59] A. V. Oppenheim and R. W. Schafer. *Discrete-Time Signal Processing*. Prentice-Hall, Englewood Cliffs, N.J., third edition edition, 2010.

[60] D. W. Baker. Pulsed ultrasonic Doppler blood-flow sensing. *IEEE Trans. Son. Ultrason.*, SU-17:170–185, 1970.

[61] C. Kasai, K. Namekawa, A. Koyano, and R. Omoto. Real-Time Two-Dimensional Blood Flow Imaging using an Autocorrelation Technique. *IEEE Trans. Son. Ultrason.*, 32:458–463, 1985.

[62] T. Loupas, J. T. Powers, and R. W. Gill. An axial velocity estimator for ultrasound blood flow imaging, based on a full evaluation of the Doppler equation by means of a two-dimensional autocorrelation approach. *IEEE Trans. Ultrason., Ferroelec., Freq. Contr.*, 42:672–688, 1995.

[63] J. A. Jensen. Stationary echo canceling in velocity estimation by time-domain cross-correlation. *IEEE Trans. Med. Imag.*, 12:471–477, 1993.

[64] S. Bjærum, H. Torp, and K. Kristoffersen. Clutter filter design for ultrasound colour flow imaging. *IEEE Trans. Ultrason., Ferroelec., Freq. Contr.*, 49:204–209, 2002.

[65] A. C. H. Yu and L. Løvstakken. Eigen-based clutter filter design for ultrasound color flow imaging: a review. *IEEE Trans. Ultrason., Ferroelec., Freq. Contr.*, 57(5):1096–1111, 2010.

[66] S. G. Foster. *A pulsed ultrasonic flowmeter employing time domain methods*. PhD thesis, Dept. Elec. Eng., University of Illinois, Urbana, Ill., 1985.

[67] J. A. Jensen. Artifacts in velocity estimation using ultrasound and cross-correlation. *Med. Biol. Eng. Comp.*, 32/4 suppl.:s165–s170, 1994.

[68] B. Dunmire, K. W. Beach, K-H Labs., M. Plett, and D. E. Strandness. Cross-beam vector Doppler ultrasound for angle independent velocity measurements. *Ultrasound Med. Biol.*, 26:1213–1235, 2000.

[69] P. Tortoli, G. Bambi, and S. Ricci. Accurate Doppler angle estimation for vector flow measurements. *IEEE Trans. Ultrason., Ferroelec., Freq. Contr.*, 53(8):1425–1431, Aug. 2006.

[70] M. D. Fox. Multiple crossed-beam ultrasound Doppler velocimetry. *IEEE Trans. Son. Ultrason.*, SU-25:281–286, 1978.

[71] V. L. Newhouse, D. Censor, T. Vontz, J. A. Cisneros, and B. B. Goldberg. Ultrasound Doppler probing of flows transverse with respect to beam axis. *IEEE Trans. Biomed. Eng.*, BME-34:779–788, 1987.

[72] G. E. Trahey, J. W. Allison, and O. T. von Ramm. Angle independent ultrasonic detection of blood flow. *IEEE Trans. Biomed. Eng.*, BME-34:965–967, 1987.

[73] J. A. Jensen and P. Munk. A new method for estimation of velocity vectors. *IEEE Trans. Ultrason., Ferroelec., Freq. Contr.*, 45:837–851, 1998.

[74] J. A. Jensen. A new estimator for vector velocity estimation. *IEEE Trans. Ultrason., Ferroelec., Freq. Contr.*, 48(4):886–894, 2001.

[75] M. E. Anderson. Multi-dimensional velocity estimation with ultrasound using spatial quadrature. *IEEE Trans. Ultrason., Ferroelec., Freq. Contr.*, 45:852–861, 1998.

[76] R. Bracewell. *The Fourier transform and its applications*. McGraw-Hill, New York, 3rd edition, 1999.

[77] J. A. Jensen. Optimization of transverse oscillating fields for vector velocity estimation with convex arrays. In *Proc. IEEE Ultrason. Symp.*, pages 1753–1756, July 2013.

[78] J. Udesen, M. B. Nielsen, K. R. Nielsen, and J. A. Jensen. Examples of in-vivo blood vector velocity estimation. *Ultrasound Med. Biol.*, 33:541–548, 2007.

[79] M. J. Pihl, M. B. Stuart, B. G. Tomov, M. F. Rasmussen, and J. A. Jensen. A transverse oscillation approach for estimation of three-dimensional velocity vectors. Part II: Experimental validation. *IEEE Trans. Ultrason., Ferroelec., Freq. Contr.*, 51(10):1608–1618, 2014.

[80] J. A. Jensen, H. Holten-Lund, R. T. Nilsson, M. Hansen, U. D. Larsen, R. P. Domsten, B. G. Tomov, M. B. Stuart, S. I. Nikolov, M. J. Pihl, Y. Du, J. H. Rasmussen, and M. F. Rasmussen. SARUS: A synthetic aperture real-time ultrasound system. *IEEE Trans. Ultrason., Ferroelec., Freq. Contr.*, 60(9):1838–1852, 2013.

[81] M. J. Pihl, M. B. Stuart, B. G. Tomov, J. M. Hansen, M. F. Rasmussen, and J. A. Jensen. Preliminary examples of 3D vector flow imaging. In *Proc. SPIE Med. Imag.*, volume 8675, pages 86750H–1–86750H–12, 2013.

[82] M. J. Pihl and J. A. Jensen. A transverse oscillation approach for estimation of three-dimensional velocity vectors. Part I: Concept and simulation study. *IEEE Trans. Ultrason., Ferroelec., Freq. Contr.*, 61:1599–1607, 2014.

[83] J. T. Ylitalo and H. Ermert. Ultrasound synthetic aperture imaging: Monostatic approach. *IEEE Trans. Ultrason., Ferroelec., Freq. Contr.*, 41:333–339, 1994.

[84] M. O'Donnell and L. J. Thomas. Efficient synthetic aperture imaging from a circular aperture with possible application to catheter-based imaging. *IEEE Trans. Ultrason., Ferroelec., Freq. Contr.*, 39:366–380, 1992.

[85] M. Karaman, P. C. Li, and M. O'Donnell. Synthetic aperture imaging for small scale systems. *IEEE Trans. Ultrason., Ferroelec., Freq. Contr.*, 42:429–442, 1995.

[86] M. Karaman and M. O'Donnell. Subaperture processing for ultrasonic imaging. *IEEE Trans. Ultrason., Ferroelec., Freq. Contr.*, 45:126–135, 1998.

[87] G. R. Lockwood and F.S. Foster. Design of sparse array imaging systems. In *Proc. IEEE Ultrason. Symp.*, pages 1237–1243, 1995.

[88] G. R. Lockwood, J. R. Talman, and S. S. Brunke. Real-time 3-D ultrasound imaging using sparse synthetic aperture beamforming. *IEEE Trans. Ultrason., Ferroelec., Freq. Contr.*, 45:980–988, 1998.

[89] S. I. Nikolov, K. Gammelmark, and J. A. Jensen. Recursive ultrasound imaging. In *Proc. IEEE Ultrason. Symp.*, volume 2, pages 1621–1625, 1999.

[90] M. Tanter, J. Bercoff, L. Sandrin, and M. Fink. Ultrafast compound imaging for 2-D motion vector estimation: application to transient elastography. *IEEE Trans. Ultrason., Ferroelec., Freq. Contr.*, 49:1363–1374, 2002.

[91] J. Udesen, F. Gran, K. L. Hansen, J. A. Jensen, C. Thomsen, and M. B. Nielsen. High frame-rate blood vector velocity imaging using plane waves: Simulations and preliminary experiments. *IEEE Trans. Ultrason., Ferroelec., Freq. Contr.*, 55(8):1729–1743, 2008.

[92] J. Udesen, F. Gran, and J. A. Jensen. Fast Color Flow Mode Imaging Using Plane Wave Excitation and Temporal Encoding. In *Proc. SPIE - Progress in biomedical optics and imaging*, volume 5750, pages 427–436, Feb. 2005.

[93] S. I. Nikolov and J. A. Jensen. In-vivo Synthetic Aperture Flow Imaging in Medical Ultrasound. *IEEE Trans. Ultrason., Ferroelec., Freq. Contr.*, 50(7):848–856, 2003.

[94] K. L. Gammelmark and J. A. Jensen. Multielement synthetic transmit aperture imaging using temporal encoding. *IEEE Trans. Med. Imag.*, 22(4):552–563, 2003.

[95] M. H. Pedersen, K. L. Gammelmark, and J. A. Jensen. In-vivo evaluation of convex array synthetic aperture imaging. *Ultrasound Med. Biol.*, 33:37–47, 2007.

[96] J. A. Jensen and S. I. Nikolov. Directional synthetic aperture flow imaging. *IEEE Trans. Ultrason., Ferroelec., Freq. Contr.*, 51:1107–1118, 2004.

[97] O. Bonnefous. Measurement of the complete (3D) velocity vector of blood flows. In *Proc. IEEE Ultrason. Symp.*, pages 795–799, 1988.

[98] J. A. Jensen and N. Oddershede. Estimation of velocity vectors in synthetic aperture ultrasound imaging. *IEEE Trans. Ultrason., Ferroelec., Freq. Contr.*, 25:1637–1644, 2006.

[99] R. Y. Chiao, L. Y. Mo, A. L. Hall, S. C. Miller, and K. E. Thomenius. B-mode blod flow (B-flow) imaging. In *Proc. IEEE Ultrason. Symp.*, pages 1677–1680, 2000.

[100] J. A. Jensen. Method for in-vivo synthetic aperture B-flow imaging. In *Proc. SPIE - Progress in biomedical optics and imaging*, volume 5373, pages 44–51, 2004.

[101] E. Mace, G. Montaldo, B. Osmanski, I. Cohen, M. Fink, and M. Tanter. Functional ultrasound imaging of the brain: theory and basic principles. *IEEE Trans. Ultrason., Ferroelec., Freq. Contr.*, 60(3):492–506, 2013.

[102] J. Bercoff, G. Montaldo, T. Loupas, D. Savery, F. Meziere, M. Fink, and M. Tanter. Ultrafast compound Doppler imaging: Providing full blood flow characterization. *IEEE Trans. Ultrason., Ferroelec., Freq. Contr.*, 58(1):134–147, January 2011.

[103] B-F. Osmanski, M. Pernot, G. Montaldo, A. Bel, E. Messas, and M. Tanter. Ultrafast Doppler imaging of blood flow dynamics in the myocardium. *IEEE Trans. Med. Imag.*, 31(8):1661–1668, 2012.

[104] K. L. Hansen, J. Udesen, F. Gran, J. A. Jensen, and M. B. Nielsen. In-vivo examples of complex flow patterns with a fast vector velocity method. *Ultraschall in Med.*, 30:471–476, 2009.

[105] E. Mace, G. Montaldo, I. Cohen, M. Baulac, M. Fink, and M. Tanter. Functional ultrasound imaging of the brain. *Nature methods*, 8(8):662–664, 2011.

[106] E. Konofagou and J. Ophir. A new elastographic method for estimation and imaging of lateral displacements, lateral strains, corrected axial strains and poisson's ratios in tissues. *Ultrasound Med. Biol.*, 24(8):1183–1199, 1998.

[107] K. Nightingale, M. S. Soo, R. Nightingale, and G. Trahey. Acoustic radiation force impulse imaging: In-vivo demonstration of clinical feasibility. *Ultrasound Med. Biol.*, 28:227–235, 2002.

[108] K. R. Nightingale, M. L. Palmeri, R. W. Nightingale, and G. E. Trahey. On the feasibility of remote palpation using acoustic radiation force. *J. Acoust. Soc. Am.*, 110(1):625–634, 2001.

[109] W. N. McDicken, G. R. D. Sutherland, C. M. Moran, and L. N. Gordon. Color Doppler velocity imaging of the myocardium. *Ultrasound Med. Biol.*, 18(6-7):651–654, 1992.

[110] K. L. Hansen, J. Udesen, C. Thomsen, J. A. Jensen, and M. B. Nielsen. In vivo validation of a blood vector velocity estimator with MR angiography. *IEEE Trans. Ultrason., Ferroelec., Freq. Contr.*, 56(1):91–100, 2009.

[111] M. M. Pedersen, M. J. Pihl, J. M. Hansen, P. M. Hansen, P. Haugaard, M. B. Nielsen, and J. A. Jensen. Secondary arterial blood flow patterns visualised with vector flow ultrasound. In *Proc. IEEE Ultrason. Symp.*, pages 1242–1245, 2011.

[112] J. B. Olesen, M. S. Traberg, M. J. Pihl, and J. A. Jensen. Non-invasive measurement of pressure gradients using ultrasound. In *Proc. SPIE Med. Imag.*, pages 1–7, mar 2013. 86750G.